SYNTHESIS AND CHARACTERIZATION OF FUNCTIONALIZED [4Fe-4S] CUBANE CLUSTERS AND LINKAGE TO METALLOPORPHRYRINS AS CATALYTIC SITES

by

Deidra L. Gerlach

A dissertation submitted in partial fulfillment
of the requirements for the degree of
Doctor of Philosophy
(Chemistry)
in the University of Michigan
2013

Doctoral Committee:

Associate Professor Nicloai Lehnert, Chair
Professor Paul F. Hollenberg
Assistant Professor Mi Hee Lim
Assistant Professor Nataniel Szymczak

DEDICATION

This thesis is dedicated to my beautiful nieces Jasmine, Lindsay, and Jada who are already growing into smart and capable young women.

ACKNOWLEDGEMENTS

First and foremost I must acknowledge my advisors Nicolai and Dimitri for the guidance through graduate school and opportunity to explore two challenging areas of synthetic bio-inorganic chemistry. Thank you Nicolai for your patience, your sharing of knowledge, the international travel, and the great beer and burgers at your BBQs!

Of course, the completion of my degree would not be capable without my committee members and replacement committee members: Paul Hollenberg, Mi Hee Lim, Vincent Pecoraro, and Nataniel Szymczak. The incredible staff, and the ever helpful instrument technicians of the chemistry department (especially, Jeff Kampf for his remarkable patience with disordered iron-sulfur structures and the structures found in Ch 3 and 4) have all be so helpful. Also, Chris Ziegler and James Engle at Akron University were outstandingly helpful to collect x-ray diffraction data and solve the structure of the complexes presented in Ch 2. I am grateful of the funding I received from the Rackham Merit Fellowship and the Chemistry Department which allowed me to stay out of the classroom for several semesters.

I will forever cherish the camaraderie and friendships built with fellow graduate students and particularly fellow lab mates. The everyday discussions and tips and even the sharing of complaints and frustrations bound us as family. In particular, I whole-heartedly thank Shawn Eady for saving my sanity and for all the laughs.

Although my parents, brothers, extended family, and friends may not have understood the tasks and expectations of a PhD student in chemistry or ever made it to the end of the introduction of my thesis project, they have always cheered me on and given me confidence. Thank you Mom, for showing me how to be a strong woman with a voice. Thank you Dad, for giving me the belief that I can be whatever I want to be, and do whatever I want to do.

Lastly, thank you Rick, my love, for putting up with me through every milestone, for being my shoulder to cry on, for being my cleaning staff, for always having dinner and a lunch prepared, for helping care for our dogs Paco and Erma, and for giving me unconditional love.

TABLE OF CONTENTS

LIST OF TABLES

LIST OF FIGURES

LIST OF ABBREVIATIONS

aNIR	assimilatory nitrite reductase
APS	adenosine 5’-phosphosulfate
aSIR	assimilatory sulfite reductase
ATP	adenosine 5’-triphosphate
CODH	carbon monoxide dehydrogenase
CYP	cytochrome P450
CV	cyclic voltammetry
1,2-dce	1,2-dichloroethane
DI	deionized
DMAPP	dimethylallyl diphosphate
DMF	dimethylformamide
dNIR	dissimilatory nitrite reductase
dSIR	dissimilatory sulfite reductase
EPR	electron paramagnetic resonance
FAD	flavin adenine dinucleotide
Fc/Fc^{+}	ferrocene/ferrocenium
FMN	flavin mononucleotide
IPP	isopentenyl diphosphate
IspG	HMBPP synthase
IspH	HMBPP reductase
HiPIP	high potential iron protein
HMBPP	(E)-4-hydroxy-3-methyl-but-2-enyl diphosphate
HRP	horseradish peroxidase
LCT	liquid chromatography time-of-flight
MeCN	acetonitrile

$MeNO_2$	nitromethane
MI	1-methylimidazole
MOF	metal organic framework
NADPH	nicotinamide adenine dinucleotide phosphate
NHE	normal hydrogen electrode
NIR	nitrite reductase
NMR	nuclear magnetic resonance
NO	nitric oxide
PAPS	3'-phosphoadenosine-5-phosphosulfate
py	pyridine
RB	round bottom
SAM	S-adenosylmethionine
SIR	sulfite reductase
SMePy	*para*-pyridylmethylthiolate
SPy	*para*-pyridylthiolate
THF	tetrahydrofuran
TLC	thin layer chromatography
T*o*-F_2PP	*meso*-tetra(*ortho*-difluorophenyl)porphyrin
T*per*-F_5PP	*meso*-tetra(penta-fluorophenyl)porphyrin
TPP	*meso*-tetraphenylporphyrin
$TriSH_3$	1,3,5-triethyl-2,4,6-tris(3-sulfanylindolyl[1]methyl)benzene

Abstract

Iron-sulfur clusters and hemes are found throughout biological systems in a variety of unique and important enzymatic systems. Only one type of enzyme contains both a heme and an iron-sulfur cluster at the active site of the enzyme, sulfite and nitrite reductase (SIR/NIR). The assimilatory variety of these enzymes is capable of both sulfite and nitrite reduction to produce sulfide and ammonia, respectively. As these enzymes function at ambient temperature and pressure and perform a six-electron reduction without substrate dissociation, they provide an attractive blueprint for biologically inspired multi-electron catalysts. The enzyme active site contains a [4Fe-4S] cluster which supplies electrons to a catalytic heme center through an axially coordinated sulfide bridge.

The goal of this research is to synthesize complexes biologically inspired by SIR/NIR for the purpose of reductive catalysis. The three key structural features for the first generation complex design include (i) a metalloporphyrin, for use as a catalytic site, (ii) a [4Fe-4S] cluster, for use as an electron reservoir, and (iii) a bridging ligand or atom to link the catalytic and electron storage components. Two designs were formulated using different forms of connectivity for the bridging component: a) axial coordination of an iron-sulfur cluster via a bridging ligand to a heme complex, and b) covalent ligation of the iron-sulfur cluster directly to the functionalized porphyrin ligand.

The axially bound model developed here was optimized to accomplish the optimal binding of the heme and [4Fe-4S] cluster by modification of the electron density of the heme iron by the addition of electron withdrawing groups to the porphyrin, and by evaluation of different types of organic bridges to connect these components. The

covalently bound model utilizes a singly functionalized porphyrin ligand intended for direct binding to an iron-sulfur cluster for electron transfer from the cluster to the heme iron via the porphyrin ligand. The covalent bound model is likely the more viable route for further progress. In the process of synthesizing and testing different types of functionalized [4Fe-4S] clusters, an interesting, sulfide-bridged cluster was discovered. The properties of the sulfide-bridged double cubane cluster with pyridylthiolate ligands were then investigated.

CHAPTER 1

Introduction

1.1 Biological Sulfur and the Biogeochemical Sulfur Cycle

The biogeochemical sulfur cycle is an important process in the oxidative balance of all biogeochemical cycles on Earth. Natural ebbs toward the fully oxidized sulfur (sulfate) and fully reduced sulfur (sulfide) can be found throughout the atmosphere, hydrosphere, biosphere and lithosphere (Figure 1.1). Sulfur has an equally important role in agriculture, industry, metallurgy, and the chemical processes essential to all living things.

It is important to understand the purely inorganic cycling of sulfur through the lithosphere, hydrosphere and atmosphere since it is within these domains that the biosphere, in which humans fit, is physically and chemically located. Sulfur is the 16th most abundant element in the Earth's crust but the 4th most abundant in sea water.[1] The purely inorganic part of the sulfur cycle is a relatively simple cycle on its own where the majority of the sulfur found in the lithosphere and hydrosphere exists in the fully oxidized state of sulfate or as metal sulfide minerals. The dynamic regions of the biogeochemical cycle are the atmosphere and biosphere. The major contributors to the sulfur content in the atmosphere are volcanic action emitting H_2S and SO_2, bacterial ponds emitting similar gasses and small organic thiols and disulfides, and human produced sulfur pollutants from the burning of fossil fuels.[2]

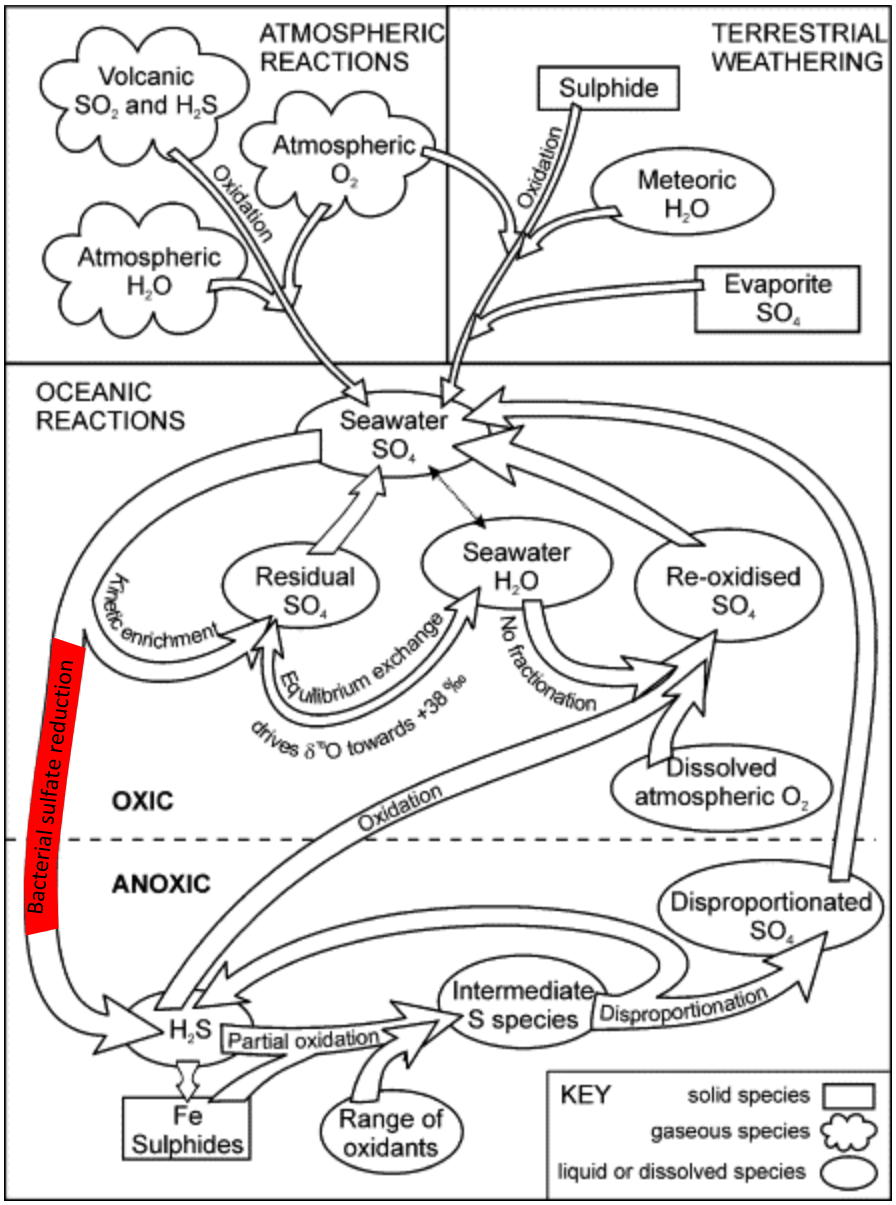

Figure 1.1. Biogeochemical sulfur cyle.[3]

Although the abundance of sulfur is rather low in the dynamic portions of the earth system, living organisms have been utilizing sulfur since bacteria first evolved to use photosynthesis by metabolizing H_2S gas three billion years ago.[1] Some organisms specialize in reducing sulfur compounds to sulfide, while others oxidize sulfur compounds to sulfate.[4] Animals are unable to synthesize cysteine and rely on bacteria

and plants primarily as their source.[5] Understanding the mechanism by which cysteine is synthesized is important to humanity since human life is dependent on other organisms for this vital biological molecule. Nature has evolved the machinery to catalyze the activation and reduction of sulfate to sulfide by means of a series of four enzymes, plus an enzyme for the assimilation of sulfide for the synthesis of cysteine (Figure 1.2).

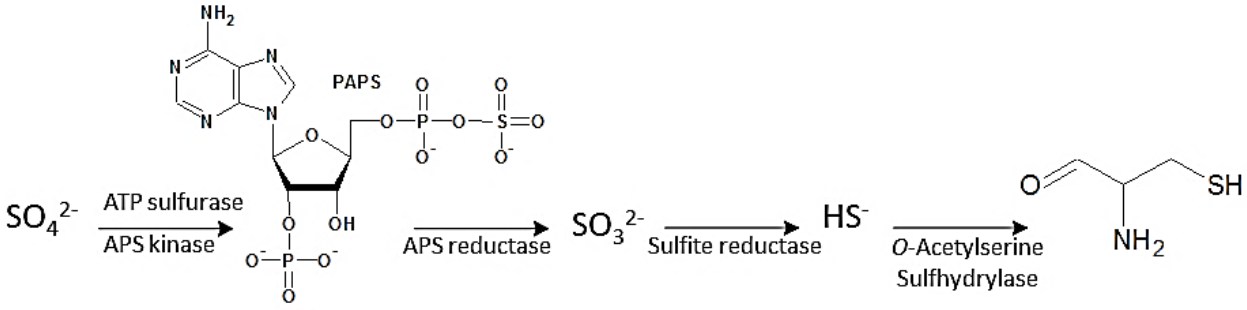

Figure 1.2. Overall enzymatic cascade for the reduction of sulfate to sulfide and production of cysteine.

ATP sulfurylase and APS kinase is the leading enzyme pair that prepares sulfate for reduction by first reacting it with ATP to produces adenosine 5'-phosphosulfate (APS) and 3'-phosphoadenosine-5-phosphosulfate (PAPS), respectively. These two enzymes are found paired in animals or as two separate enzymes in plants, fungi, and bacteria.[6] ATP sulfurylase produces APS from a sulfate ion and one ATP molecule and PAPS requires a second ATP to further phosphorylate APS. Both enzymes employ a binding pocket intelligently defined by H-bonds to selectively orient the correct substrates to utilize the high energy bond of ATP to catalyze the reactions.[6] The second enzyme in the series, APS reductase, performs the first reduction of the sulfate group to sulfite. Both assimilatory and dissimilatory APS reductases perform the same reduction for different purposes and by very different mechanisms.[7] Neither variety of the enzyme is found in animals. Assimilatory APS reductase performs a two electron reduction by

binding the sulfate end of PAPS to a unique iron-center of an iron-sulfur cubane cluster [4Fe-4S] and subsequent reduction by a thioredoxin reductase cofactor through the formation of a disulfide.[5b] Alternatively, dissimilatory APS reductase employs a binding pocket utilizing H-bonding so that the sulfate group of APS is positioned adjacent to a flavin that reduces the sulfate by two electrons and releases sulfite.[8] The primary role of the assimilatory enzyme is to produce sulfite as needed for biosynthesis; whereas the dissimilatory enzyme uses the reduction of sulfate as the end electron acceptor in anaerobic respiration of bacteria.[7] The last enzyme in the process of reducing sulfite to sulfide is assimilatory sulfite reductase (aSIR) in which six electrons pass through the [4Fe-4S] cluster of the active site to the siroheme catalytic site to reduce sulfite to sulfide.[9] The production of cysteine is completed by the enzyme *o*-acetylserine sulfhydrylase by reacting a Schiff base with the sulfide without assistance from metal coordination.[5c]

The power horse in this series of enzymes for the reduction of sulfate to biocompatible sulfide is SIR. The oxidation state of the sulfur changes from +4 to -2 as six electrons consecutively pass to the substrate without releasing intermediates. The assimilatory enzyme is necessary to produce sulfide; whereas, the corresponding dissimilatory SIR (dSIR) does not necessarily complete all six one- electron reductions to yield sulfide. SIR has a very unusual active site that consists of a catalytic heme derivative, a siroheme, linked to a [4Fe-4S] ferredoxin cluster. The major goal of this thesis is to build a functional analog of SIRs. In order to better understand the structures and roles of iron-sulfur clusters, a detailed introduction into this subject is provided in the following.

1.2 Biological Iron

Iron is the fourth most abundant element in the Earth's crust (6.3%) preceded by oxygen (47%), silicon (26%), and aluminum (8.1%) and followed by calcium (5.0%), magnesium (2.9%), sodium (2.3%), and potassium (1.5%).[10] Thus, unsurprisingly, iron is the most abundant transition metal found in living organisms. In addition to its ubiquity, iron has a multitude of accessible oxidation states ranging from -2 to +6. The standard reduction potential of Fe^{3+} to Fe^{2+} is +0.77 V. Both the ferrous and ferric oxidation states can exist in high-spin or low-spin states depending on the ligand field. Iron coordinates well with a wide variety of biological ligands including standard amino acids such as cysteinate, histidine, aspartate etc., and also chelates well with inorganic ligands such as water, oxygen, nitric oxide, carbon monoxide, sulfide, and cyanide. The versatility of binding and electronic states of iron results in highly tunable reduction potentials making iron an excellent biological metal for electron transfer and catalysis. Thus, iron is utilized by biological systems for various vital processes predominantly including redox activity.

Iron is exploited in the prosthetic groups of proteins for the transfer of electrons and small molecules, small molecule binding as sensors, to catalyze oxygenations, hydrolysis, general biosynthesis (especially hormones), oxidative and reductive processes, and utilized for structural support, etc.[11] Accordingly, all of these proteins are supported and maintained by a well-developed system for transporting, storing, and, in the case of most single cell organisms, harvesting of iron ions.[12] Ferritin, transferrin and siderophores are the most commonly known proteins and biomolecules in the category of iron storage, transport, and acquisition. Regardless of the diversity and similarities of iron

proteins in function, location, and organisms originating from, iron proteins can be categorized into three major (and somewhat vague) classes: iron-sulfur proteins, heme-proteins and non-heme proteins, each ranging in complexity. Typical heme-proteins utilize a variant of iron protoporphyrin IX. Some of the most commonly known proteins which feature a heme prosthetic group that is vital for their function are hemoglobin, myoglobin, catalase, horseradish peroxidase (HRP), cytochrome P450's (CYP), and the numerous varieties of cytochrome c electron transfer proteins.[13]

Non-heme iron proteins contain a diverse collection of prosthetic groups including mono-nuclear iron centers, bi-nuclear diiron oxo-complexes, and bi-nuclear Fe/Mn oxo complexes. Finally, the active sites of iron-sulfur proteins include bi-, tri- and tetra-nuclear iron-sulfur clusters, Fe/Ni-sulfur complexes, and polynuclear Fe(/Mo)-sulfur complexes.[11] Iron-sulfur clusters are commonly ligated directly to proteins via cysteine, histidine, or aspartate side chains with bridging sulfides connecting the iron centers. The category of iron-sulfur clusters in itself is quite diverse and of major interest to this thesis work.

1.3 Typical Iron-Sulfur Clusters Used for Electron Transfer

Included in the class of iron-sulfur proteins is the single iron center in rubredoxin, [Fe(S-Cys)$_4$], an iron tetrahedrally bound to four cysteinates (Figure 1.3). Note that the tetrahedral iron of rubredoxin bound by four sulfur atoms is in essence the building block of the larger iron-sulfur clusters. The iron of rubredoxin cycles between the ferrous and ferric oxidation states in one-electron transport processes. In addition to the single iron center in rubredoxin, iron-sulfur clusters are widely utilized in electron transport chains leading to the catalytic sites of enzymes. The iron-sulfur cluster dimers, [2Fe-2S], and

cubanes, [4Fe-4S], are ferredoxins which serve as one electron reductions or oxidations. In the [2Fe-2S] and [4Fe-4S] ferredoxins inorganic sulfide is used to bridge between the iron centers. Ligation is completed by addition of cysteinate ligands, and thus these sites are better labeled as $[Fe_2S_2(S\text{-}Cys)_4]$ and $[Fe_4S_4(S\text{-}Cys)_4]$, respectively (Figure 1.3). Lastly, in the iron-sulfur cluster family there is a tri-nuclear cuboidal cluster with a [3Fe-4S] core which is much less common in biological systems. The core structure is analogous to the tetra-nuclear cubane cluster, deficient of one iron center and a coordinated cysteinate, thus the chemical formula for this prosthetic group is $[Fe_3S_4((S\text{-}Cys)_3]$ (Figure 1.3).

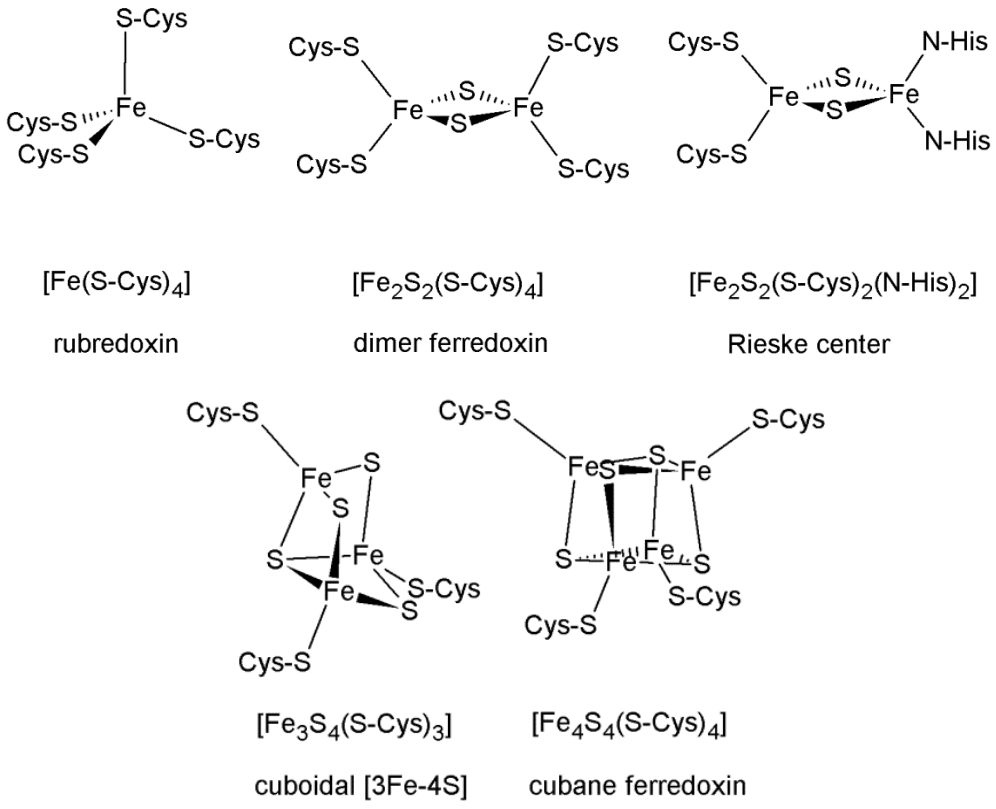

Figure 1.3. Protein active site structures of typical iron-sulfur clusters.

The individual iron centers in the iron-sulfur clusters are essentially tetrahedrally coordinated by a combination of sulfide and cysteinate ligands. Characteristic Fe-S bond lengths of 2.2 to 2.4 Å are observed for the internal iron-sulfide and external iron-thiolate bonds (Figure 1.4). The external Fe-S(Cys) bonds are often longer than the internal Fe-sulfide bonds by as much as a tenth of an Ångstrom.[14] These longer bond lengths may aid in the ligand exchange that occurs within some ferredoxins with a flexible loop in which a conformational change will follow the ligand exchange typically triggered by reduction of the cluster.[15] It should also be noted that for the cubane ferredoxins multiple average internal Fe-S bond lengths exist where the average length of eight of the bonds is 2.294 Å, oriented on opposite faces, and the four Fe-S bonds that connect these faces have an average length of 2.256 Å.[14, 16] The cubane ferredoxin can thus be viewed as two dimeric ferredoxins stacked on top of each other with alternating Fe and S corners.

The internal S-Fe-S bond angles of the iron centers in the ferredoxins are on average in the range of 102 to 106° and therefore labeled as distorted tetrahedral. The Fe-S-Fe bond angles are more acute on average in the range of 73 to 77° so that the sulfurs protrude out of the perfect cubane while the irons are compressed inwards.[16] The bond angles and bond lengths of the cubane ferredoxin core [4Fe-4S] match well with the trimeric [3Fe-4S] core.[14] The lability of an iron center in the cubane ferredoxin is observed in the enzyme aconitase in which the catalytic activity depends on the occupancy of the labile iron center.[17] The labile nature of exogenous ligands and even iron centers would suggest that the iron-sulfur clusters are highly fragile cofactors. Yet, the ferredoxin cofactors are quite robust *in vivo* being stable in water and in the presence of most organic and biological ligands. Instability of iron-sulfur clusters arises in the

presence of oxidants and strong acids which lead to oxidative decomposition, or in the presence of high concentrations of cupric ions which are more aggressive thiophiles.

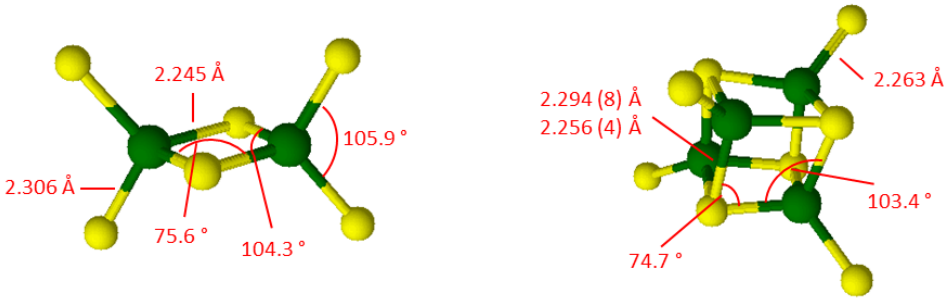

Figure 1.4. Scheme of the dimeric and tetrameric ferredoxins with average bond lengths and bond angles included.

The versatility of use and ability to tune the reduction potentials of the ferredoxins are instrumental to the biological function of these electron transfer centers. The single iron center rubredoxins have a typical redox potential range of 0 to -100 mV vs NHE for the Fe^{3+}/Fe^{2+} couple. The [2Fe-2S] ferredoxins typically operate in the range of -150 to -450 mV and cycle between the $[Fe_2S_2]^{2+}/[Fe_2S_2]^{+}$ oxidation states.[13] Here, the oxidized cluster entails two high-spin ferric iron centers that undergo a one electron reduction to the reduced cluster formally with one high-spin ferric and one high-spin ferrous iron center, although because the two metal centers are electronically coupled it is best to describe the reduced state as having two $Fe^{2.5+}$ centers. An excellent example of the tuning of the reduction potential of iron-sulfur clusters is the comparison of the [2Fe-2S] ferredoxin to the Rieske center, which differs from the [2Fe-2S] ferredoxin in that the Rieske center has two cysteinates ligated to one of the irons and two histidines bound to the other iron center (instead of all cysteinate ligands) (see Figure 1.3). The reduction potentials in which the Rieske centers operate are significantly more positive (in the range of -100 to +400 mV) for the $[Fe_2S_2]^{2+}/[Fe_2S_2]^{+}$ couple.[13]

The cuboidal iron-sulfur cluster is capable of operation in both the high and low potential ranges as observed for the [2Fe-2S] dimers. This again is an elegant example for the ability of the biological environment to modify and fine-tune redox potentials of iron-sulfur clusters. Most cuboidal ferredoxins transfer electrons in the range of -300 to -700 mV for the $[Fe_4S_4]^{2+}/[Fe_4S_4]^{1+}$ couple. However, adjustments in the protein environment allowing different degrees of solvation stabilizes the cluster in the higher oxidation state allowing for operation at more positive potentials of +100 to +400 mV by using the $[Fe_4S_4]^{3+}/[Fe_4S_4]^{2+}$ couple.[13, 18] These cubanes are usually referred to as a high potential iron proteins (HiPIPs).

The resting state of the cuboidal ferredoxins is the $[Fe_4S_4]^{2+}$ state; where two high-spin ferric and two high-spin ferrous irons coexist for an overall formal $Fe^{2.5+}$ oxidation state. Each tetrahedral iron center of the [4Fe-4S] clusters is high-spin due to each of the three S^{2-} core sulfide ligands and the exogenous thiolate ligand being weak field ligands. Since the cubane can be viewed as two stacked dimeric ferredoxins, the electronic coupling can also be explained with the following model. Each dimer face has high-spin, ferromagnetically coupled ferric and ferrous iron centers for a total spin of $S={}^{9}/_{2}$. The two faces are anti-ferromagnetically coupled for a total spin of S=0. Thus, these systems are spectroscopically "challenged" due to the complexity of this spin coupling scheme and the diamagnetic ground state (Figure 1.5). When reduced to the $[Fe_4S_4]^{1+}$ state, one ferric and three ferrous iron centers are coupled. When oxidized to the $[Fe_4S_4]^{3+}$ state, three ferric and one ferrous iron centers are coupled. In each case the total spin becomes S=½. Enzymes with an electron transfer chain of iron-sulfur clusters to a redox active catalytic site are often difficult to probe spectroscopically due to added

signals from the many ferrodoxins. Therefore, the domains containing just the electron transfer chains of ferredoxins are often cleaved from the protein before further study.

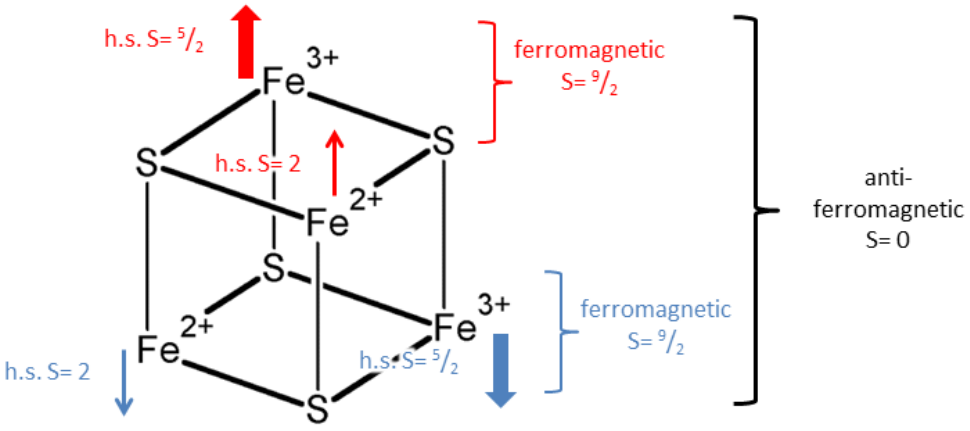

Figure 1.5. Spin coupling diagram for the resting state of the $[Fe_4S_4]^{2+}$ cluster core.

1.4 Unique Iron-Sulfur Cluster Structures and Biological Reactivity

Being an early developed prosthetic group dating back to an era before an oxygen atmosphere developed, sulfur was the abundant electron source in anaerobic respiration. Hence, through evolution nature has found other functions for iron-sulfur clusters in addition to electron transfer. Iron-sulfur clusters are also involved in redox regulation of gene transcription, non-redox active catalysis at a particular iron-center, and radical stabilization.[15, 19] For example, the WhiB-like family of proteins utilizes an iron-sulfur cubane cluster in a low molecular weight protein for small molecule sensing, such as O_2 or NO. By exogenous ligand replacement of the ferredoxin, the cluster can become fully ligated by NO.[20] A myriad of radical propagated reactions occur in living organisms that require the radical S-adenosylmethionine (SAM), as in the synthesis of biotin, but the extreme reactivity of free radicals in biological systems cannot go unregulated. One way

to stabilize SAM radicals is by binding to an open coordination site of a site-differentiated cubane ferredoxin.[21]

Another example in the recent literature are the iron-sulfur cubane clusters involved in the IspH and IspG enzymes, which are part of the isoprenoid synthesis pathway in harmful pathogens. At a unique iron center of the cubane with a labile ligand coordinated, binding of the alkene substrate initiates two one-electron reduction and protonation steps to reduce a terminal C-OH to a C-H bond (Figure 1.6).[22] These enzymes have been of recent interest as the targets of an inhibitory drug since these enzymes for the production of isoprenoids are only found in organisms that are harmful to humans.

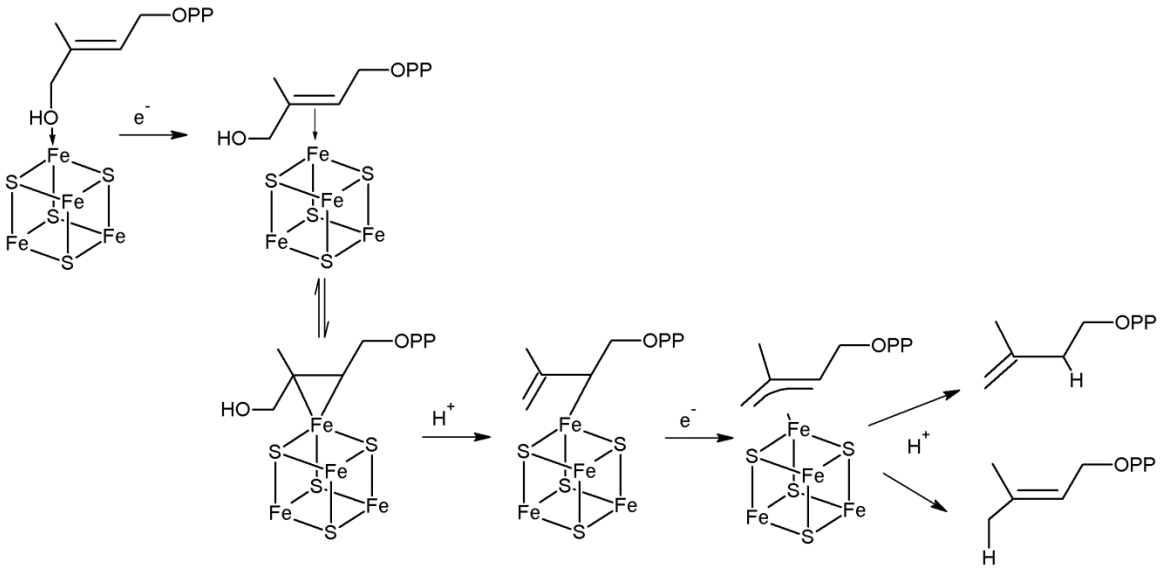

Figure 1.6. Schematic mechanism for the conversion of HMBPP to DMAPP and IPP by IspH at the [4Fe-4S] catalytic site.

In addition to the role of site-differentiated cubane ferredoxins for radical stabilization and for providing a binding site for the coordination of substrates which are then modified at a different position in the molecule, further specialized and structurally

more complex iron-sulfur clusters have also evolved for very unique chemistry in biology. Both the P-cluster and the FeMo-cofactor of nitrogenases are metal centers built from iron-sulfur clusters. Another structurally unique motif is the Fe/Ni-sulfide prosthetic group of carbon monoxide dehydrogenase (CODH) (Figure 1.7).

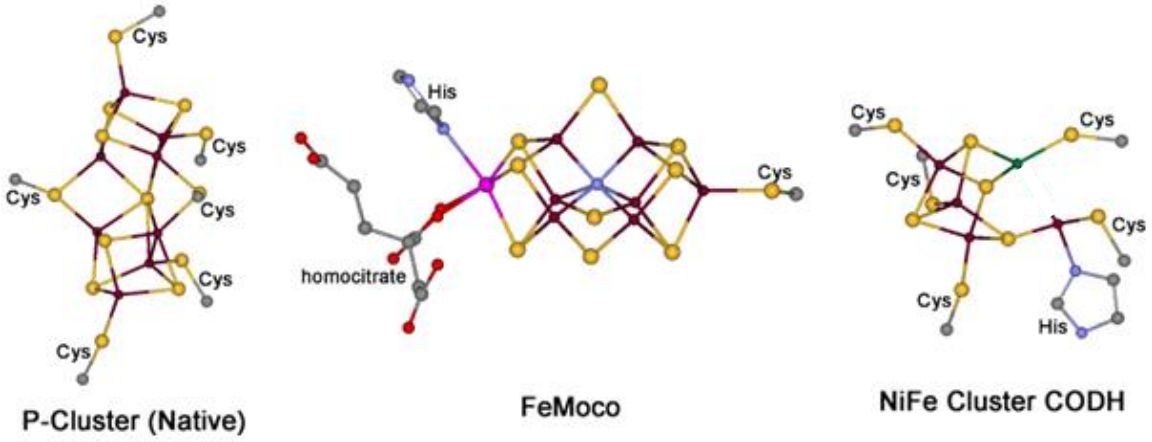

Figure 1.7. Structures of the P-cluster (left) and FeMoco (center, central blue atom now identified as carbide) of nitrogenase and NiFe cluster of CODH (right).

Nitrogenases, found only in bacteria, perform an important role in the global nitrogen cycle by catalytically reducing atmospheric dinitrogen to the biocompatible form of nitrogen, ammonia, through an ATP driven process.[23] The molybdenum enzyme is the most commonly found nitrogenase in bacteria, whereas the vanadium and iron-only nitrogenases are less common and are usually only utilized under unusual conditions such as lower temperature or when molybdenum starved.[24] Each nitrogenase contains the active site cofactor (FeMoco, FeVco, or FeFeco), a P-cluster for electron transfer, and a binding site for the reduced Fe protein with two bound ATP.[24] As of yet only the structure of the FeMoco has been determined crystallographically (Figure 1.3), but based on spectroscopic data and the similarity in sequence, the FeVco active site cluster is

usually thought to be similar to the FeMoco structure, where Mo is then replaced by V.[25] Recently, the mystery central atom of nitrogenase has been confirmed as carbide.[26] Overall, the cofactor has the structure of two iron-sulfur cubanes that share a "sulfur" corner which is actually the carbide. Additionally, the source of the carbide central atom has been shown to originate from the methyl group on SAM.[26c] Three bridging sulfides ring the juncture. Similarly, the P-cluster that functions in electron transfer to the cofactor also has a structure consisting of two iron-sulfur cubanes which share a sulfur corner with two bridging sulfides (Figure 1.7).

In the reduction of N_2 by nitrogenase, H^+ is concomitantly reduced to H_2. Additional substrates Mo-nitrogenase is capable of reducing are other small unsaturated molecules, such as acetylene, ethylene, and propylene, and the enzyme is inhibited by CO, CN^- and H_2. V-nitrogenase shows similar behavior with one significant discrepancy: instead of being inhibited by CO, the H_2 production is seen to decrease in the presence of CO, indicating that the reduction of H^+ is being diverted and that CO is reduced. Product analysis shows a mixture of light hydrocarbons, in particular ethylene, ethane, propylene and propane by forming new C-C bonds.[27]

The active site of CODH, the C cluster, contains a tri-nuclear cuboidal iron-sulfur cluster [3Fe-4S] in which the vacant iron site is inhabited by a nickel atom. The detached iron that would make up the fourth cuboidal iron position remains adjacent to the cubane cluster. CODHs typically operate in the oxidative direction, oxidizing CO to CO_2 at the Ni center, and the resulting electrons are passed through an iron-sulfur electron transfer chain to a ferredoxin carrier.[28] In some variants of this enzyme its catalytic activity is connected to acetyl Coenzyme A synthase, which utilizes the CO produced in the

reductive pathway of CODH where (CO_2 is reduced to CO) for the biosynthesis of an acetyl group, which is then attached to Coenzyme A (Figure 1.7).

1.5 Electron Transfer Ferredoxins Covalently Linked to an Enzyme Active Site

Although ferredoxins are typically utilized in biological systems in electron transfer chains, it is rare to find a true ferredoxin of the [4Fe-4S] variety in the active site of an enzyme covalently linked to a catalytic site.[13] Only three classes of such metalloproteins are known: iron-iron hydrogenase, acetyl CoA synthase, and assimilatory and dissimilatory sulfite/nitrite reductases (Figure 1.8). In these cases, the ferredoxin is covalently bound to the catalytic site via a cysteine thiolate or a sulfide bridge for the purpose of fast electron transfer to the catalytic metal, which is responsible for substrate binding and reduction. Each of these three metalloproteins has a very specialized role in nature and all of them are part of anaerobic processes.

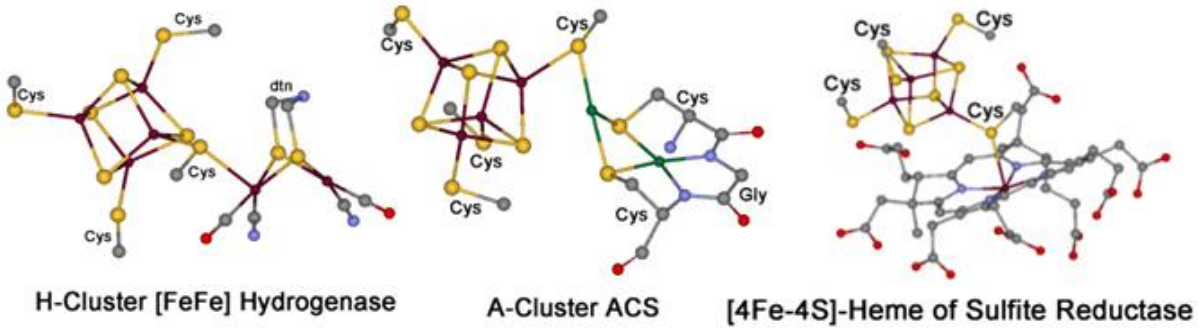

Figure 1.8. Structures of enzyme prosthetic groups featuring a [4Fe-4S] cluster directly linked to the catalytic site: the H-cluster (left), the A-cluster (center), and the active site of SIR (right).

The iron-iron hydrogenase catalyses the reversible reduction of protons to hydrogen at a sulfide bridged diiron cluster known as the H cluster.[14] One molecule of

the *D. desulfuricans* FeFe hydrogenase under optimum conditions produces 9000 molecules of hydrogen in one second at 30 ˚C.[29] The H-cluster has a modified [2Fe-2S] unit in which the bridging sulfides are thiolates with a unique three atom chain for proton shuttling. The remaining coordination sites are occupied by CN^- and CO molecules (Figure 1.8). One iron center is bound through the sulfur of cysteinate to the adjacent [4Fe-4S] cluster. The distal iron center coordinates a water molecule that is labile upon reduction to the Fe(I)-Fe(I) catalytically active oxidation state thus providing an open site for protonation and hydride formation as the first step of the mechanism of the enzyme.

Acetyl CoA synthase catalyzes the synthesis of acetyl coenzyme A by first generating an acetyl group, from the reduction of CO and the transfer of a methyl group, at the cysteinate bridged Ni(Cu)-Ni cluster, the A-cluster.[28a] Somewhat similar to the C cluster of CODH, the [4Fe-4S] cluster is bound through a Ni or Cu center to a square planar Ni center where all of the catalytic activity occurs (Figure 1.8). Unlike the C cluster of CODH, the iron-sulfur cluster is a cubane for optimum electron transfer.

Assimilatory sulfite and nitrite reductase hemoproteins (aSIR/aNIR) catalyze the reduction of sulfite and nitrite to sulfide and ammonia, respectively, at a siroheme active site which is linked by a sulfide or cysteine to a [4Fe-4S] cluster (Figure 1.8).[4d] Although heme and iron sulfur clusters are widely spread throughout metalloproteins as electron transfer and catalytic sites, SIR and NIR are unique in that they are the only known metalloenzymes that incorporate a bridged heme-ferrodoxin center in the active site (see the following section).

1.6 Assimilatory Sulfite and Nitrite Reductases

Both assimilatory sulfite and nitrite reductases (aSIR/aNIR) have the same active site with highly conserved amino acids. Overall, the active sites of these enzymes are essentially identical with the most significant differences being in the protein secondary structure and substrate channels. Due to their closely related active sites, sulfite is reduced by aNIR and nitrite is reduced by a SIR, but not at the full catalytic rate for the natural substrate.[30]

The reduction power of aSIR and aNIR is what makes these heme proteins so interesting, as they can reduce substrate by an unprecedented six electrons before releasing the final product.[9] Note that the closely related dissimilatory sulfite and nitrite reductases catalyze the reduction of sulfite and nitrite in two-electron steps for the purpose of detoxification. The amino acids that define the distal pocket of the siroheme where substrate binds are significantly different between the assimilatory and dissimilatory enzymes.[31]

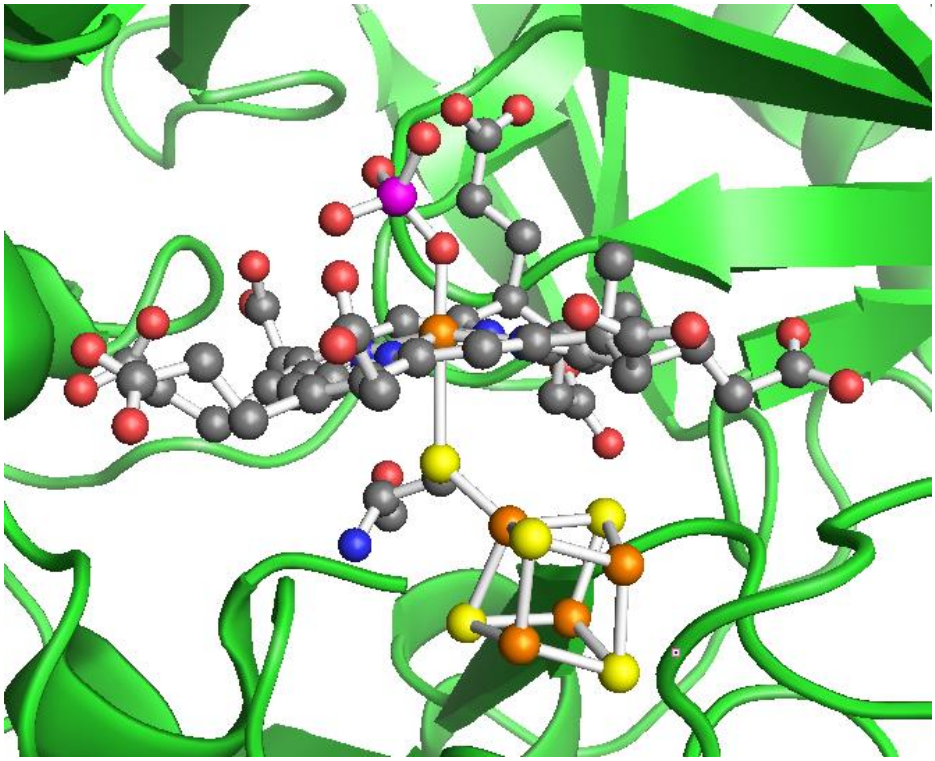

Figure 1.9. Pymol structure of the resting state of the active site of aSIR from *E coli* with phosphate bound at the heme.

The [4Fe-4S] cluster in aSIR/aNIR is of typical structure and function, but the heme is not common for enzymes. The key features of the siroheme are the partial reduction of the porphyrin core and the abundance of carboxylic acid groups at the periphery of the macrocycle. These acid groups serve two purposes, structural stabilization and proton supply to the active site. H-bonding to the surrounding protein locks the heme in place which stabilizes the sulfide/thiolate link to the [4Fe-4S] cluster and protects the sulfide bridge from protonation. Figure 1.9 shows the resting state of aSIR with phosphate bound to the heme.

The reduction potentials of the siroheme and the iron sulfur cluster found in aSIR of *E. coli* are -340 mV and -405 mV, respectively.[4d] Depending on the organism, the

initial electron donor could be a NADPH or photosystem I, in plants, via a FAD-FMN or [2Fe-2S] ferredoxin domain.[32]

It can be inferred that the reduction of substrate occurs generally in two electron increments to release a water molecule (for every two electrons transferred), as proposed for the dissimilatory variety.[31] Most recent research has emphasized the importance of the protein residues in the substrate binding pocket of the active site of aSIR and provides strong evidence for a "push-pull" mechanism where the proton and electron transfer to substrate is linked.[33] Figures 1.10 and 1.11 highlight the significance in the amino acids in the distal pocket of aSIR vs. dSIR, respectively, for the reactivity of the enzyme.[31, 33] The resting state of the active site comprises a high-spin ferric iron in the siroheme and the $[Fe_4S_4]^{2+}$ ferrodoxin. Activation of the catalytic site occurs with the first electron transfer to the siroheme iron, via the electron transfer chain, forming the ferrous iron which releases phosphate from the binding site. Substrate reduction occurs by binding at the distal side of the siroheme in the catalytically active ferrous state, and protons are supplied with the aid of the carboxylic groups of the siroheme and ordered waters in the active site pocket.[33-34] The siroheme iron and ferredoxin exchange between the Fe^{2+}/Fe^{3+} and $[Fe_4S_4]^{2+}/[Fe_4S_4]^{1+}$ oxidation states, respectively, as substrate reduction occurs. Although the exact sequence of electron transfer between the [4Fe 4S] cluster and the siroheme of the active site is not known, it has been shown that both the cluster and the heme are reduced by one electron each in the catalytically active state of the enzyme.[35]

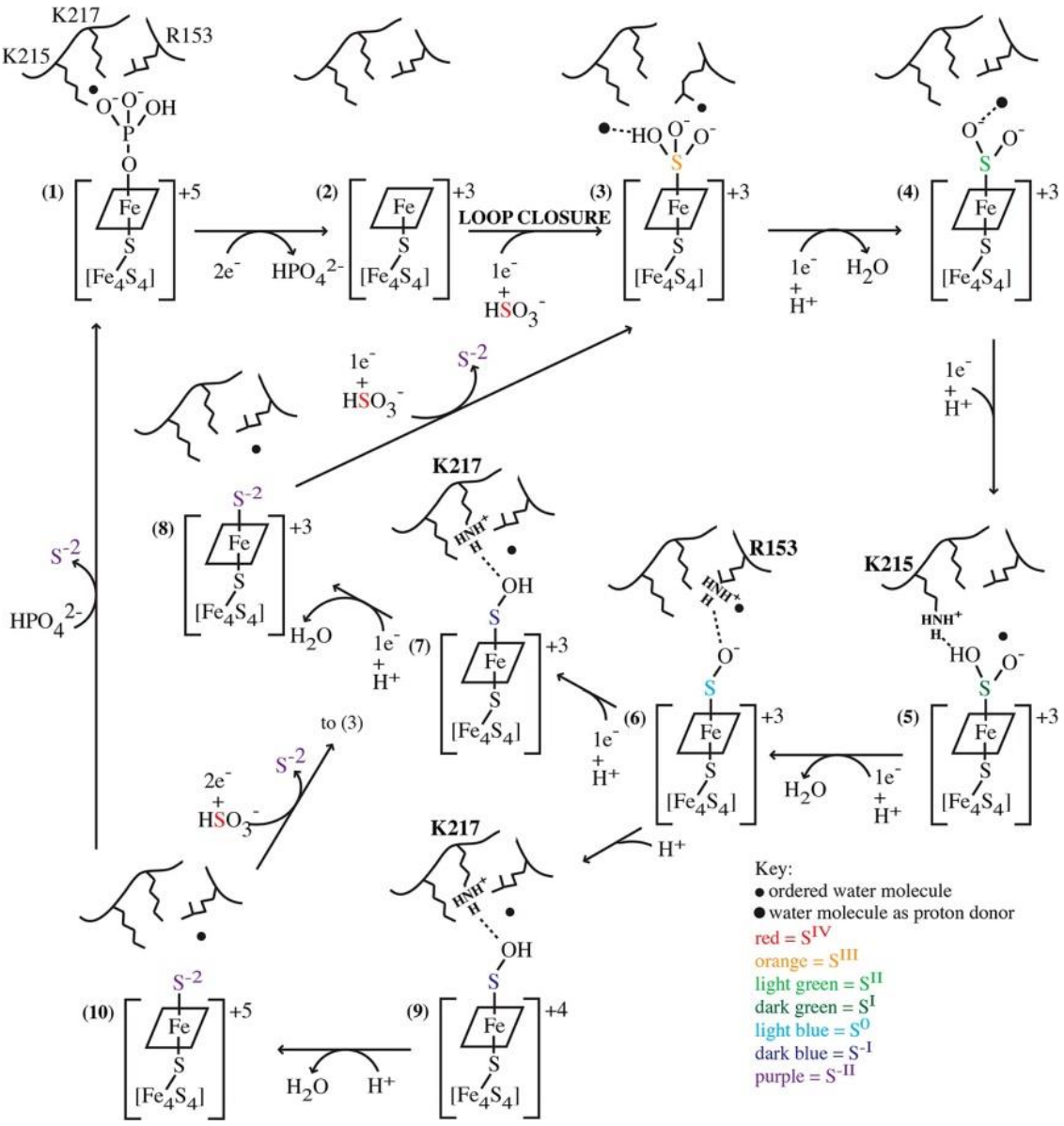

Figure 1.10. Mechanistic scheme for aSIR as proposed by Smith et al.[33]

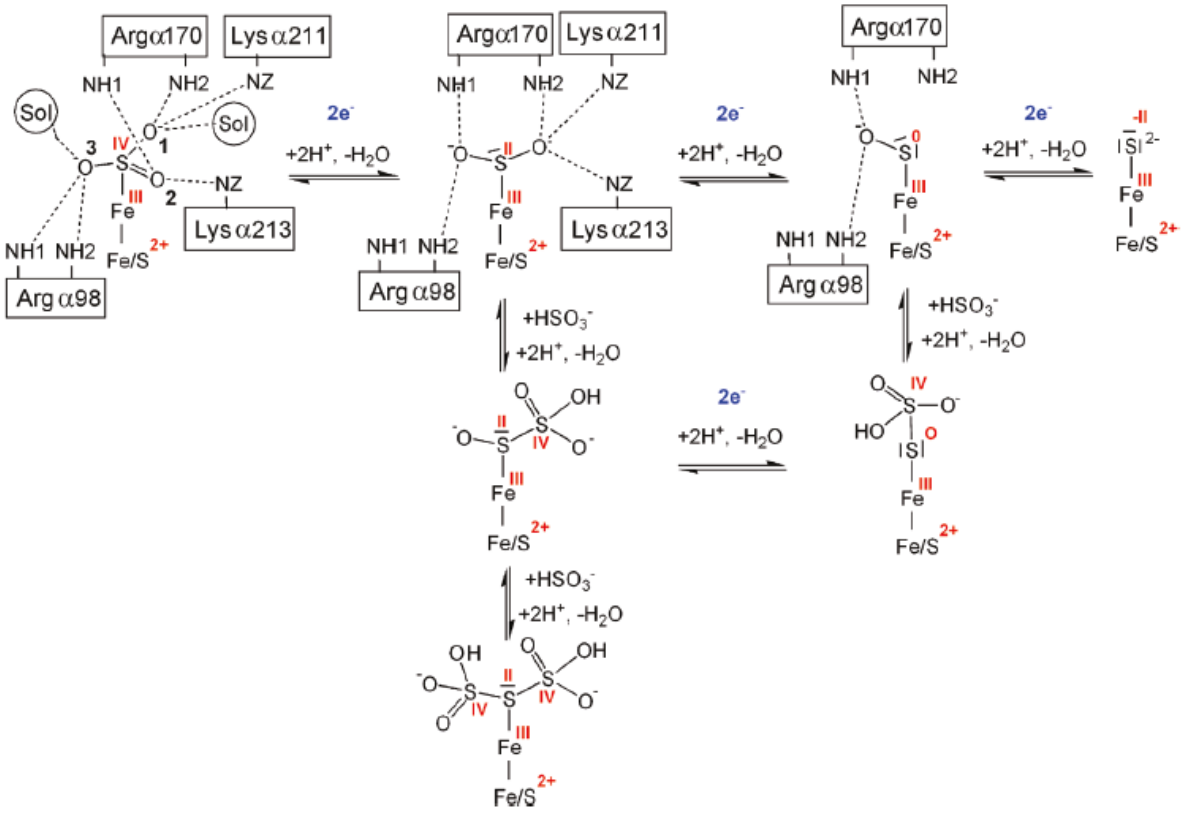

Figure 1.11. Mechanistic scheme for dSIR as proposed by Parey et al.[31]

1.7 Scope of the Thesis

In chapter 2, the synthesis and characterization of unique metal complexes, which are biologically *inspired* by aSIR, are discussed as potential catalytic arrays. The design of these metal complexes is based on the components of the active site of aSIR for the goal of building a robust, single molecule complex capable of catalysing multi-electron reductions of substrates. The simple design requirements include a [4Fe-4S] cluster bridged to a heme via axial ligation. Proof that the desired complex design is obtained in solution with further structural understanding of the complex is achieved via absorption spectroscopy and electrochemistry demonstrating binding of zinc porphyrins axially by a

small organic ligand that bridges to a site-differentiated iron-sulfur cubane cluster. These results are compared to previously published catalyst designs.

In chapter 3, the synthesis and characterization of an alternative biologically inspired catalyst array are presented. The axially bound SIR catalyst design discussed in chapter 2 is modified to covalently link the heme and the iron-sulfur cubane cluster. This is achieved by utilizing tetraphenylporphyrin with a coordinating functional group at the periphery for covalent ligation to a site-differentiated iron-sulfur cubane cluster. Spectroscopic evidence is presented indicating that the moieties are bound, and the properties of the resulting macromolecule are investigated. Together chapters, 2 and 3 present unique designs for biologically inspired catalysts that entail a potential catalytic site and an electron reservoir such as found in the enzyme SIR.

In chapter 4, the synthesis and characterization of unique iron-sulfur cubane clusters tetra-ligated by functionalized ligands are presented. Emphasized are the crystal structures of 4-pyridinethiolate ligated single clusters and a single sulfide bridged double iron-sulfur cubane cluster. Comparisons to previously published iron-sulfur cluster structures and reduction potentials are made. The differences and trends of the physical and spectroscopic properties of the thiolate bound iron-sulfur clusters allow for a better understanding of the ability to tune the reduction potentials of the clusters and give insight into potential further reactivity of clusters with functionalized ligands for synthesis of larger arrays and polymeric solids known metal-organic frameworks (MOFs) using the functionalized clusters as linking ligands.

1.8 References

[1] W. L. Chameides, E. M. Perdue, *Biogeochemical Cycles*, Oxford University Press, New York, New York, **1997**.

[2] R. W. Howarth, J. W. B. Stewart, M. V. Ivanov, *Sulfur Cycling on the Continents*, John Wiley & Sons, Chichester, England, **1992**.

[3] S. H. Bottrell, R. J. Newton, *Earth-Science Rev.* **2006**, *75*, 59-83.

[4] a) P. R. Holmes, T. A. Fowler, F. K. Crundwell, *Journal of The Electrochemical Society* **1999**, 2906-2912; b) C. Dahl, C. G. Friedrich, *Microbial Sulfur Metabolism*, Springer, Berlin, Germany, **2008**; c) S. Bose, M. F. G. Hochella Jr., Y.A., D. W. Kennedy, D. E. McCready, A. S. Madden, B. H. Lower, *Geochimica et Cosmochimica Acta* **2009**, *73*, 962-976; d) M. E. Stroupe, E. D. Getzoff, in *Handb. Metalloproteins* (Eds.: A. Messerschmidt, R. Huber, T. Poulos, K. Wieghardt), John Wiley & Sons, Ltd., Chichester, **2001**, pp. 471-485.

[5] a) D. J. Lalor, T. Schnyder, V. Saridakis, D. E. Pilloff, A. Dong, H. Tang, T. S. Leyh, E. F. Pai, *Protein Engineering* **2003**, *16*, 1071-1079; b) J. Chartron, K. S. Carroll, C. Shiau, H. Gao, J. A. Leary, C. R. Bertozzi, C. D. Stout, *Journal of Molecular Biology* **2006**, *364*, 152-169; c) R. Schnell, W. Oehlmann, M. S. Singh, G., *J. Biol. Chem.* **2007**, *282*, 23473-23481.

[6] S. Harjes, P. Bayer, A. J. Scheidig, *J. Mol. Biol.* **205**, *347*, 623-635.

[7] H. D. Peck Jr., *J. Bacteriol.* **1961**, *82*, 933-939.

[8] A. Schiffer, G. Fritz, P. M. H. Kroneck, U. Ermler, *Biochemistry* **2006**, *45*, 2960-2967.

[9] B. R. Crane, L. M. Siegel, E. D. Getzoff, *Science* **1995**, *270*, 59.

[10] W. F. McDonough, S. Sun, *Chem. Geol.* **1995**, *120*, 223-253.

[11] P. A. Frey, G. H. Reed, *ACS Chem. Biol.* **2012**, *7*.

[12] E. C. Theil, D. J. Goss, *Chem. Rev.* **2009**, *109*, 4568-4579.

[13] R. Holm, P. Kennepohl, E. I. Solomon, *Chem. Rev.* **1996**, *96*, 2239-2314.

[14] P. V. Rao, R. H. Holm, *Chem. Rev.* **2004**, *104*, 527-559.

[15] H. Beinert, R. H. Holm, E. Münck, *Science* **1997**, *277*, 653659.

[16] E. D. Duée, E. Fanchon, J. Vicat, L. C. Sieker, J. Meyer, J. M. Moulis, *J. Mol. Biol.* **1994**, *243*, 683-695.

[17] J. J. G. Moura, I. Moura, T. A. Kent, J. D. Lipscomb, B. H. Huynh, J. LeGall, A. V. Xavier, E. Münck, *J. Biol. Chem.* **1982**, *257*, 6259-6267.

[18] A. Dey, F. E. Jenney Jr., M. W. W. Adams, E. Babini, Y. Takahashi, K. Fukuyama, K. O. Hodgson, B. Hedman, E. I. Solomon, *Science* **2007**, *318*, 1464-1468.

[19] P. L. Roach, *Curr. Opin. Chem. Biol.* **2011**, *15*, 267-275.

[20] a) J. C. Crack, J. Green, M. I. Hutchings, A. J. Thomson, N. E. LeBrun, *Antioxidants & Redox Signaling* **2012**, *17*, 1215; b) J. C. Crack, L. J. Smith, M. R. Stapleton, J. Peck, N. J. Watmough, M. J. Buttner, R. S. Buxton, J. Green, V. S. Oganesyan, A. J. Thomson, N. E. LeBrun, *J. Am. Chem. Soc.* **2012**, *133*, 1112.

[21] a) J. Cheek, J. B. Broderick, *J. Biol. Inorg. Chem* **2001**, *6*, 209-226; b) P. A. Frey, S. J. Booker, *Adv. Protein Chem.* **2001**, *58*, 1-45.

[22] K. Wang, W. Wang, J. No, Y. Zhang, Y. Zhang, E. Oldfield, *J. Am. Chem. Soc.* **2010**, *132*, 6719-6727.

[23] B. K. Burgess, D. J. Lowe, *Chem. Rev.* **1996**, *96*, 2983-3011.

[24] R. R. Eady, *Chem. Rev.* **1996**, *96*, 3013-3030.

[25] R. R. Eady, *Coord. Chem. Rev.* **2003**, *237*, 23-30.

[26] a) K. M. Lancaster, M. Roemelt, P. Ettenhuber, Y. Hu, M. W. Ribbe, F. Neese, U. Bergmann, S. DeBeer, *Science* **2011**, *334*, 974-977; b) T. Spatzal, M. Aksoyoglu, L. Zhang, S. L. A. Andrade, E. Schleicher, S. Weber, D. C. Rees, O. Einsle, *Science* **2011**, *334*, 940; c) J. A. Wiig, Y. Hu, C. C. Lee, M. W. Ribbe, *Science* **2012**, *337*, 1672-1675.

[27] a) C. C. Lee, Y. Hu, M. W. Ribbe, *Science* **2010**, *329*, 642; b) C. C. Lee, Y. Hu, M. W. Ribbe, *Angew. Chem.* **2011**, *123*, 5659-5661.

[28] a) V. Svetlitchnyi, H. Dobbek, W. Meyer-Klaucke, B. T. Thomas Meins, P. Römer, R. Huber, O. Meyer, *Proc. Natl. Acad. Sci. U. S. A.* **2004**, *101*, 446-451; b) H. Dobbek, V. Svetlitchnyi, L. Gremer, R. Huber, O. Meyer, *Science* **2001**, *293*, 1281-1285; c) S. W. Ragsdale, *J. Inorg. Biochem.* **2007**, *101*, 1657-1666.

[29] R. Cammack, *Nature* **1999**, *397*, 214-215.

[30] B. R. Crane, E. D. Getzoff, *Curr. Opin. Struct. Biol.* **1996**, *6*, 744.

[31] K. Parey, E. Warkentin, P. M. H. Kroneck, U. Ermler, *Biochemistry* **2010**, *49*, 8912-8921.

[32] M. Nakayama, T. Akashi, T. Hase, *J. Inorg. Biochem.* **2000**, *82*, 27-32.

[33] K. W. Smith, M. E. Stroupe, *Biochemistry* **2012**, *51*, 9857-9868.

[34] L. J. Young, L. M. Siegel, *Biochemistry* **1988**, *27*, 4991-4999.

[35] P. A. Janick, L. M. Siegel, *Biochemistry* **1982**, *21*, 3538-3547.

CHAPTER 2

Assimilatory Sulfite Reductase Inspired Complexes for Catalysis

Axially Bound Model

(**Deidra L. Gerlach**, Dimitri Coucouvanis, Nicolai Lehnert, "Connecting [4Fe-4S] Clusters and Hemes: Towards Modelling the Active Site of Sulfite Reductase" *European Journal of Inorganic Chemistry* **2013**, 3883-3890.)

2.1 Introduction

In a predominantly oxidative world, reductive biological processes by default are intriguing and offer inspiration for synthetic catalyst designs being either biomimetic or biologically inspired by enzymatic systems. Biomimetic catalysts of an enzyme active site are typically the aim of model complex studies for the purpose of characterizing and understanding electronic states of intermediates and reactivity to elucidate the mechanism of the target enzyme. Alternatively, a biologically inspired complex utilizes the known structural properties, electronic state, and activity of an enzyme active site to design a catalyst that shows similar activity for applications in synthetic chemistry. Enzymes make for excellent role models for synthetic catalysts due to the refined properties of their active sites that lead to catalytic turnover of incredible rates at room temperature, ambient pressure, and mild redox potentials.

The enzyme aSIR reduces sulfite by six electrons without releasing any intermediates while undergoing significant structural changes, shuttling six electrons essentially seamlessly to the substrate at rates upwards of thousands of electrons per

second per heme catalytic site.[1] As discussed in Chapter 1, SIR and NIR have a unique active site in which a siroheme is axially bound by a sulfide or thiolate (depending on the organism) that bridges to a [4Fe-4S] cluster. The siroheme itself in the active site is unique and a prosthetic group that is not commonly utilized in enzymes. The siroheme cofactor has been shown to be an ancestor to the more common heme b, found in the cytochrome P450 family, and is also an early intermediate in the synthesis of hemes.[2] The partially reduced siroheme, which has an isobacteriochlorin core, is less susceptible to reductive stress which was found in the environment of the world before aerobic respiration developed. This contrasts with the heme of cytochromes, which have a porphyrin core (Figure 2.1).[3] The reductive power of siroheme itself has been reported; where, in the presence of reductant, sulfite was reduced producing two, four, and six electron reduced sulfur species, at low turnover rates than aSIR achieves.[4] The ability of siroheme to reduce sulfite is magnified by having a direct link to the [4Fe-4S] cluster in the active site that is in direct connection to the electron transport chain of the enzyme.[1] Thus, the link of the catalytic site of the siroheme to the [4Fe-4S] cluster is a vital feature for fast turnover of aSIR for the efficient "push" of electrons to the substrate.

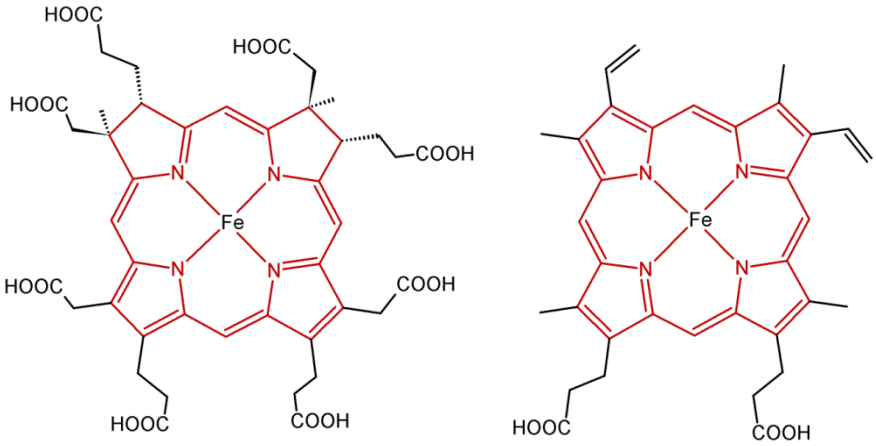

Figure 2.1. Schematic structures of the siroheme with an iron isobacteriochlorin core (left) and the iron protoporphyrin IX with an iron porphyrin core (right).

Aside from the key components of the active site, the siroheme, the sulfide/thiolate link, and the [4Fe-4S] cluster (Figure 2.2), it is important to note other key features of the active site and substrate binding pocket at the distal side of the siroheme. The [4Fe-4S] cluster is secured to the protein backbone by ligation to three cysteinate amino acid side chains and protected from protons. The sulfide linking atom is nestled between the two metal moieties and protected by the folded protein and the siroheme. In organisms where the linking sulfur is a cysteinate group, the cysteine is an amino acid side chain of the protein providing another anchor to the backbone.

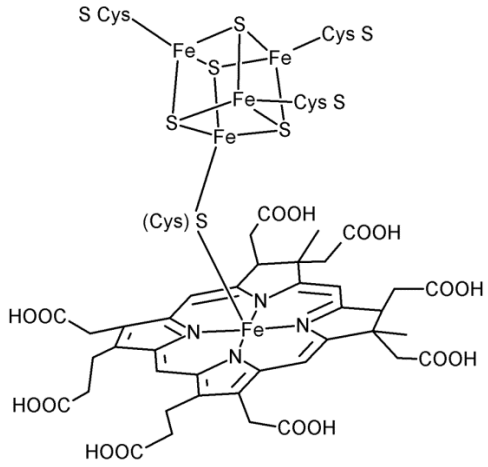

Figure 2.2. Schematic view of the active site of SIR.

The siroheme is not covalently linked to the protein through the isobacteriochlorin ring. The abundance of periphery carboxylic groups on the siroheme aids in immobilizing the catalytic site within the protein and physically orienting the heme with respect to the [4Fe-4S] cluster to provide stability for the single sulfur atom bridge. In addition, these carboxylic acid groups assist in proton delivery to the catalytic site via strong hydrogen bonding to organized water molecules in the active site. Lastly, the substrate binding pocket at the distal side of the heme is vital for determining the degree of reduction of the

substrate by the SIRs. Specific lysine and arginine side chains orient the substrate via hydrogen bonding to the oxygen atoms of the substrate as well as provide for protons as the substrate is reduced, the oxygen atoms are protonated, and water molecules are released.[5] These positively charged electrophilic amino acid residues also aid to lower the reduction potential of the bound substrate by withdrawing electron density. Thus, to summarize the reactivity at the active site of SIR, the catalytic site of the heme bound to the [4Fe-4S] cluster is essential for smooth electron transfer during reduction of substrate while the protein side chains and peripheral carboxylic acid groups of the siroheme are essential for proton transfer and substrate stabilization for all six electrons to transfer.[6]

The unique structure of the active site and reductive capabilities of aSIR are rightfully intriguing for the synthetic bioinorganic chemist for catalytic complex designs. In previous model studies by Holm and coworkers, the assembly of a biomimetic model complex for SIR consisting of a ferric octaethylporphryin (OEP) bridged by sulfide to the LS_3 site-differentiated [4Fe-4S] cubane cluster was reported (Figure 2.3, left). Formation of the bridged unit in solution was demonstrated via spin delocalization to the heme and the LS_3 ligand as determined by ^{1}H-NMR spectroscopy and by Mössbauer spectroscopy.[7] This model complex could not be isolated, but could be doubly reduced in solution in two one-electron steps. No further comments on stability or potential substrate reduction were made in the original report. Unlike the enzyme, the model complex does not have a support structure for stabilizing the sulfide link between the [4Fe-4S] cluster and the heme. This link is susceptible to dissociation in polar solvents and in the presence of protons which, on the other hand, are necessary to emulate the reactivity of SIR/NIR.[8] Holm and coworkers furthered their complex design by utilizing

a more biomimetic iron isobacteriochlorin for the catalytic site which showed similar results as the previous model complex using iron OEP.[9]

Due to the limitations in stability of a sulfide bridge between the catalytic and electron reservoir moieties in the original SIR models, we have chosen a different approach to incorporate the chemical functions of the active site by utilizing a more robust (and less biomimetic) bridge than a single sulfide anion.

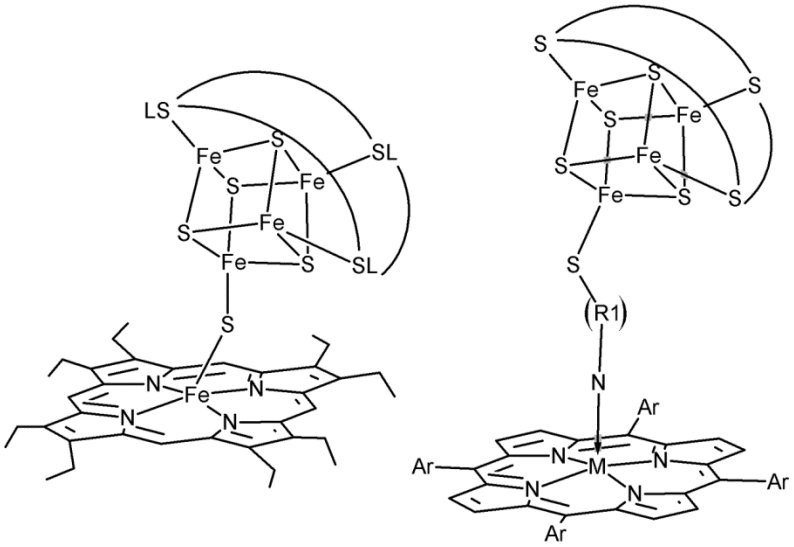

Figure 2.3. The biomimetic model complex by Holm and coworkers (left); biologically-inspired complex design applied here (right).

Our new biologically-*inspired* SIR/NIR model complex design is comprised of a metalloporphyrin bridged by a small organic ligand to a site-differentiated [4Fe-4S] cubane cluster, which is ligated by an encapsulating ligand (Figure 2.3, right). The small bridging ligand is designed to preferentially bind to the [4Fe-4S] cluster via a thiolate and to the axial coordination site of the metalloporphyrin via a pyridine or imidazole group. The bridging ligands employed here are *para*-thiopyridine and 1-ethylthioimidazole. First, we synthesized site-differentiated [4Fe-4S] clusters with these bridging ligands. Titration data monitored by UV-vis absorption spectroscopy and cyclic voltammetry

(CV) are then presented that clearly show the assembly of the full catalytic unit in solution. We further tested and identified the most appropriate heme and the best organic bridge for generating the most robust linkage between the catalytic and electron reservoir components of our model complex.

2.2 Methods and Experimental Procedures

General Procedures. All cluster and ferrous heme synthetises were performed under a nitrogen atmosphere in a glove box or by utilizing common Schlenk line techniques. ^{1}H- and ^{19}F-NMR spectra were acquired on a Varian MR400 400 MHz spectrometer and referenced to solvent. Mid-IR spectra were collected on a Perkin Elmer Spectrum BX FT-IR spectrometer and Far-IR data were obtained on a Nicolet 740 FT-IR spectrometer in KBr pellets. Mass spectrometric data were collected on a Micromass LCT Time-of Flight mass spectrometer. Elemental analyses were performed by Atlantic Mircolab, Inc., Norcross, GA. Electronic spectra were measured on a Varian CARY 1E UV-Visible spectrometer. Cyclic voltammetry experiments were conducted in a 0.1 M solution of Bu_4NPF_6 in acetonitrile (MeCN) or 1,2-dichloroethane (1,2-dce) with a glassy carbon working electrode, a Pt counter electrode and a Ag/AgCl reference electrode on a EG&G Princeton Potentiostat/Galvanostat model 263A. The redox potentials are calibrated to Fc/Fc^{+} and reported vs. NHE. Electron paramagnetic resonance (EPR) spectra were collected on a Bruker X-Band EMX electron spin resonance spectrometer equipped with a Varian liquid nitrogen cryostat (at approximately 80 K). EPR spectra were collected on frozen solutions using 20 mW microwave power and 100 kHz field modulation with the amplitude set to 1 G.

Materials. All solvents were purified by distillation and degassed. All reagents were used as purchased and degassed under vacuum as needed, including pyridine (py) and 1-methylimidazole (MI). Compounds $TriSH_3$[10], 1-$ImCH_2CH_2SH$[11], [Zn(TPP)][12], [Zn(T*o*-F_2PP)][13], [Zn(T*per*-F_5PP)][14], [Fe(T*o*-F_2PP)][15], and $(Bu_4N)_2[Fe_4S_4(SEt)_4]$[16] were prepared according to published procedures.

Synthesis of $(Bu_4N)_2[Fe_4S_4(TriS)(SEt)]$.[10b] $(Bu_4N)_2[Fe_4S_4(SEt)_4]$ (0.87 g, 0.88 mmol) was dissolved in 50 mL of MeCN and stirred in a glove box. A solution of $TriSH_3$ (0.57 g, 0.88 mmol) in 5 mL THF was prepared separately. Upon addition of the $TriSH_3$ solution to the stirring cubane solution, the color changed from brown-black to purple-black. The reaction flask was sealed, evacuated, and stirred for 4 hours under static vacuum. The dark purple solution was filtered with vacuum suction and a dynamic vacuum was applied to the filtrate for a minute. The filtrate was taken to dryness and the resulting black residue was dissolved in THF, filtered, and washed with THF until the filtrate ran clear. The THF filtrate was taken to dryness and the black-purple residue was covered with Et_2O. The resulting purple-black solid was collected by suction filtration, washed with 5-10 mL of Et_2O, and dried under vacuum to yield 0.78 g of product (63% yield). ^{1}H-NMR (400 MHz, CD_3CN, rt, ppm): δ 13.08 (broad s, S*CH*$_2$CH$_3$, 2 H), 7.84 (broad d, indolyl H, 3 H), 7.72 (d, indolyl H, 3 H), 7.31 (t, indolyl H, 3 H), 6.96 (broad t, indolyl H, 3 H), 6.50 (s, N*CH*$_2$, 6 H), 3.06 (broad m, Bu_4N^+, 16 H), 2.43-2.09 (broad m, SCH_2CH_3 and Bz CH_2CH_3 9 H), 1.62 (broad m, Bu_4N^+, 16 H), 1.36 (broad m, Bu_4N^+, 16 H), 1.19 (broad m, Bz CH_2CH_3, 9H), and 0.97 (broad m, Bu_4N^+, 24 H). FT-IR (KBr, cm^{-1}): 2958 (s), 2870 (s), 1608 (m), 1456 (s), 1379 (m), 1333 (m), 1294 (m), 1206 (m), 1151 (m), 1065 (m), 1010 (m), 880 (m), 739 (s), 645 (w), 426 (w), 344 (w).

Synthesis of $(Bu_4N)_2[Fe_4S_4(TriS)(SPy)]$. $(Bu_4N)_2[Fe_4S_4(TriS)(SEt)]$ (0.5g, 0.325 mmol) was dissolved in 20 mL of MeCN and a solution of *p*-thiopyridine (0.040 g, 0.325mmol) in 5 mL MeCN was added while stirring in a glove box. The reaction vessel was sealed and a vacuum was applied. The reaction was allowed to stir for 3 hours under static vacuum. The reaction mixture was filtered, and the filtrate was layered with 100 mL of Et_2O. The black precipitate was collected by vacuum filtration, washed with ether, and dried under vacuum to yield 0.30 g of a black solid product (58% yield). ^{1}H-NMR (400 MHz, CD_3CN, rt, ppm): δ TriS: 7.88 (broad s), 7.73 (d), 7.31 (t), 6.98 (s), 6.59 (s), 2.42 (broad s), 1.36 (s); δ SPy: 8.83 (s), 6.1 (very broad); δ Bu_4N^+: 3.07, 1.93, 1.36, 0.96 (see Figure 2.6). FT-IR (KBr, cm^{-1}): 2957 (s), 2869 (s), 1588 (m), 1567 (m), 1456 (s), 1378 (m), 1333 (m), 1293 (m), 1211 (m), 1150 (m), 1102 (m), 1061 (m), 1010 (m), 880 (m), 805 (m), 738 (s), 704 (m), 645 (w), 497 (w), 424 (w), 349 (w) (see Figure 2.8). UV-vis (1,2-dce, λ nm): 243 (sh), 283 (sh), 329 (sh), 522 (ε 6160 $M^{-1}cm^{-1}$) (see Figure 2.10). CV (MeCN, 0.01 M): -746 mV $[Fe4S4]^{2+/1+}$. LCT-MS (ESI+): *m/z* 242 $(Bu_4N)^+$; (ESI-) *m/z* 1346.1 $(Bu_4N)[Fe_4S_4(TriS)(SPy)]^-$, 1103.8 $[Fe_4S_4(TriS)(SPy)]^-$, 993.7 $[Fe_4S_4(TriS)]^-$.

Synthesis of $(Bu_4N)_2[Fe_4S_4(TriS)(SEtIm)]$. $(Bu_4N)_2[Fe_4S_4(TriS)(SEt)]$ (1.00 g, 0.65 mmol) was dissolved in 70 mL of MeCN and a solution of 1-thioethylimidazole (0.132 g, 0.71 mmol) in 5 mL MeCN was added while stirring in a glove box. The reaction vessel was sealed and a vacuum was applied. The reaction was allowed to stir for 4 hours under static vacuum. The reaction mixture was filtered and the resulting solid was washed until the filtrate ran clear (<10 mL MeCN). The filtrate was layered with 250 mL of Et_2O. The black precipitate was collected by vacuum filtration, washed with ether, and dried under vacuum to yield 0.70 g of a black solid product (67% yield). ^{1}H-NMR

(400 MHz, CD_3CN, rt, ppm): δ TriS: 7.83 (broad s), 7.72 (d), 7.30 (t), 6.95 (broad s), 6.52 (s), 2.41 (broad s), 1.18 (s); δ SEtIm: 11.92 (broad s), 7.55 (s), 7.13 (s), 6.90 (s), 4.38 (broad s); δ Bu_4N^+: 3.03, 1.58, 1.33, 0.94 (see Figure 2.7). FT-IR (KBr, cm^{-1}): 2957(s), 2929(s) 2869 (s), 1607 (w), 1454 (s), 1379 (m), 1339 (m), 1293 (m), 1209 (m), 1152 (m), 1106 (w), 1070 (w), 1009 (w), 881 (w), 738 (s), 653 (w), 528 (w), 426 (w), 339 (w) (see Figure 2.9). UV-vis (1,2-dce, λ nm): 333 (sh), 505 (ε 7587 $M^{-1}cm^{-1}$) (see Figure 2.10). CV (MeCN, 0.01 M) -843 mV $[Fe_4S_4]^{2+/1+}$ and -1563 mV $[Fe_4S_4]^{1+/0}$; (1,2-dce, 0.005 M): -435 mV $[Fe_4S_4]^{2+/1+}$. LCT-MS (ESI+): *m/z* 242.1 $(Bu_4N)^+$; (ESI-) *m/z* 1363.1 $(Bu_4N)[Fe_4S_4(TriS)(SEtIm)]^-$, 993.7 $[Fe_4S_4(TriS)]^-$, 560.4 $[Fe_4S_4(TriS)(SEtIm)]^{2-}$. Anal. Calcd. for $C_{76}H_{115}N_7S_8Fe_4$: C, 56.81%; H, 7.21%; N, 6.10%; S, 15.97%. Found: C, 57.34%; H, 7.14%; N, 5.93%; S, 15.28%.

UV-vis Binding Constant Titrations. Stock solutions of the metalloporphyrins, 1-methylimidazole (MI), and pyridine (py) were prepared utilizing an analytical scale for solids and a micro-syringe for liquids to load the reagents into volumetric flasks to afford stock solutions in the range of 1.00 mM to 15.0 mM in degassed 1,2-dce. A gas-tight quartz cuvette with a septa cap was filled with 3.00 mL of 1,2-dce dispensed via a burette. Based on the extinction coefficient of the Q band of the metalloporphyrin, the concentration of the stock solution was chosen accordingly to maintain the total absorption less than 1 for the titration reaction. An adequate amount of metalloporphyrin was added via micro-syringe for a resulting concentration of 15 – 50 μM. To this solution an aliquot of base was added via micro-syringe; the solution was shaken, and the absorption spectrum was taken. These steps were repeated until the change in absorption of the Q band was negligible. For titrations where the base is a functionalized cubane

cluster, analogous blank titrations were performed where 3.00 mL of 1,2-dce and the corresponding volume of pure solvent, equal to the volume of metalloporphyrin solution, were titrated with an identical volume of cubane solution for background subtraction. The concentrations of the metalloporphyrin and base used for each titration are summarized in Table 2.1.

Table 2.1. Titration conditions for determination of binding constants.

Zinc porphyrin, Stock concentration	Cuvette volume, [Zn(P)] volume	Base, Stock concentration	Volume addition, Molar equivalent
[Zn(TPP)]			
4.91 mM	3 mL, 10 μL	pyridine, 12.4 mM	10 μL, 2.5 equiv.
4.91 mM	3 mL, 10 μL	1-methylimidizole, 12.5 mM	2 μL, 0.51 equiv.
4.91 mM	3 mL, 10 μL	$(Bu_4N)_2[Fe_4S_4(TriS)(SEtIm)]$, 7.55 μL	3 μL, 0.46 equiv.
[Zn(T*o*-F_2PP)]			
4.90 mM	3 mL, 30 μL	pyridine, 12.4 mM	3 μL, 0.25 equiv.
4.90 mM	3 mL, 30 μL	1-methylimidizole, 12.5 mM	1 μL, 0.085 equiv.
4.96 mM	3 mL, 30 μL	$(Bu_4N)_2[Fe_4S_4(TriS)(SPy)]$, 7.51 mM	5 μL, 0.25 equiv.
4.90 mM	3 mL, 30 μL	$(Bu_4N)_2[Fe_4S_4(TriS)(SEtIm)]$, 7.55 mM	3 μL, 0.15 equiv.
[Zn(T*per*-F_5PP)]			
4.82 mM	3 mL, 30 μL	pyridine, 12.4 mM	2 μL, 0.17 equiv.
4.82 mM	3 mL, 30 μL	1-methylimidizole, 12.5 mM	1 μL, 0.086 equiv.
4.86 mM	3 mL, 30 μL	$(Bu_4N)_2[Fe_4S_4(TriS)(SPy)]$, 7.37 mM	5 μL, 0.25 equiv.
4.82 mM	3 mL, 30 μL	$(Bu_4N)_2[Fe_4S_4(TriS)(SEtIm)]$, 7.55 mM	3 μL, 0.16 equiv.

Cyclovoltammetric Titrations. Stock solutions of 14.9 mM [Zn(T*o*-F_2PP)] and 25.0 mM $(Bu_4N)_2[Fe_4S_4(TriS)(SEtIm)]$ were prepared in a solution of 0.1 M Bu_4NF_6 in 1,2-dce. Five solutions were prepared in volumetric flasks with increasing amounts of [Zn(T*o*-F_2PP)] by first adding 1 mL of the cubane stock solution and 0.33 mL, 0.66 mL, 1 mL, 1.33 mL, or 1.66 mL of [Zn(T*o*-F_2PP)]. These solutions were then diluted to 5 mL total volume for a final concentration of 5.0 mM for the cubane and 1.0, 2.0, 3.0, 3.9, and

4.9 mM for [Zn(T*o*-F_2PP)]. The Fc/Fc^+ couple was measured before and after each reaction mixture for external reference; potentials are reported vs. NHE.

Structure Determination. (C. Ziegler and J. Engle at the University of Akron)

General Procedure: The data were collected on an APEX2 CCD diffractometer with Mo source Kα radiation (λ = 0.71073) and the frames were integrated with the Bruker SAINT software package using a narrow-frame algorithm. Absorption corrections were carried out using the multi-scan method SADABS program and the structure was solved and refined using the Bruker SHELXTL Software Package until the final anisotropic full-matrix, least-squares refinement of F^2 converged. The PLATON program was used to squeeze out several disordered molecules.

$(Bu_4N)_2[Fe_4S_4Cl_4]$ experimental: A black rod crystal, approximate dimensions 0.06 mm x 0.16 mm x 0.33 mm, was coated in paratone oil, mounted on a pin and placed on a goniometer head under a stream of nitrogen cooled to 100 K. The X-ray intensity data were measured. The total exposure time was 7.00 hours. The integration of the data using a monoclinic unit cell yielded a total of 20405 reflections to a maximum θ angle of 25.11° (0.84 Å resolution), of which 4379 were independent (average redundancy 4.660, completeness = 99.6%, R_{int} = 4.60%, R_σ = 3.67%) and 3501 (79.95%) were greater than 2σ(F2). The final cell constants of a = 11.4449(7) Å, b = 11.6827(7) Å, c = 18.6182(10) Å, β = 98.505(3)°, volume = 2462.0(2) $Å^3$, are based upon the refinement of the XYZ-centroids of 5392 reflections above 20 σ(I) with 4.424° < 2θ < 49.28°. The ratio of minimum to maximum apparent transmission was 0.876. The calculated minimum and maximum transmission coefficients (based on crystal size) are 0.6311 and 0.9103.

The structure was solved and refined using the space group P2/n, with Z = 2 for the formula unit, $C_{16}H_{36}Cl_4Fe_4NS_4$. The final anisotropic full-matrix least-squares refinement on F^2 with 186 variables converged at R1 = 5.81%, for the observed data and wR2 = 20.43% for all data. The goodness-of-fit was 1.025. The largest peak in the final difference electron density synthesis was 1.278 $e^-/Å^3$ and the largest hole was -0.639 $e^-/Å^3$ with an RMS deviation of 0.168 $e^-/Å^3$. On the basis of the final model, the calculated density was 0.993 g/cm^3 and F(000), 750 e^-.

The PLATON program was used to squeeze out one of the two counter-ions of tetrabutylammonium per asymmetric unit. The number of electrons removed per unit cell was 537, or approximately 268.5 per asymmetric unit.

$[(Fe(To\text{-}F_2PP))_2O] \bullet (Bu_4N)_2[Fe_2S_2Cl_4] \bullet 2(1,2\text{-dce})$ experimental: A red plate crystal, approximate dimensions 0.11 mm x 0.14 mm x 0.40 mm, was coated in paratone oil, mounted on a pin and placed on a goniometer head under a stream of nitrogen cooled to 100 K. The X-ray intensity data were measured. The total exposure time was 43.26 hours. The integration of the data using an orthorhombic unit cell yielded a total of 48976 reflections to a maximum θ angle of 64.76° (0.85 Å resolution), of which 16526 were independent (average redundancy 2.964, completeness = 94.5%, R_{int} = 7.12%, R_σ = 10.86%) and 9856 (59.64%) were greater than $2\sigma(F^2)$. The final cell constants of a = 33.9255(16) Å, b = 23.1335(9) Å, c = 17.1901(7) Å, volume = 13491.1(10) $Å^3$, are based upon the refinement of the XYZ-centroids of 223 reflections above 20 σ(I) with 10.65° < 2θ < 66.04°. The ratio of minimum to maximum apparent transmission was 0.657. The calculated minimum and maximum transmission coefficients (based on crystal size) are 0.2290 and 0.6008.

The structure was solved and refined using the space group Pna2(1), with Z = 4 for the formula unit, $C_{88}H_{44}Cl_4F_{16}Fe_4N_8OS_6$. The final anisotropic full-matrix least-squares refinement on F^2 with 1006 variables converged at R1 = 9.23%, for the observed data and wR2 =15.94% for all data. The goodness-of-fit was 1.760. The largest peak in the final difference electron density synthesis was 1.005 $e^-/Å^3$ and the largest hole was -0.659 $e^-/Å^3$ with an RMS deviation of 0.097 $e^-/Å^3$. On the basis of the final model, the calculated density was 1.013 g/cm3 and F(000), 4120 e^-.

The PLATON program was used to squeeze out several disordered molecules. Two counter-ions of tetrabutylammonium and approximately one dichloroethane solvate per asymmetric unit were removed via the squeeze function. The number of electrons removed per unit cell was 2286, or approximately 571.5 per asymmetric unit.

2.3 Synthesis and Characterization of Site-Differentiated [4Fe-4S] Clusters.

[4Fe-4S] Cluster Synthesis. Iron-sulfur cubane clusters are easily prepared in a one pot, self-assembly reaction under anaerobic conditions.[16] Halides, thiolates, and strong σ-donors such as imines and phosphines are the preferred ligands of iron-sulfur clusters. Since each [4Fe-4S] cluster typically ligates an anionic ligand at each iron corner of the cubane, a large encapsulating ligand was first applied to the tetra-ethylthiolate cluster in order to leave only one corner of the cluster exposed, and in this way, to allow for only one heme to bind to each cubane. The $TriSH_3$ ligand was first designed by Pohl and coworkers and chosen here for the functionality and ease of synthesis as compared to the encapsulating LS_3 ligand developed Holm and coworkers (Figure 2.4).[10a]

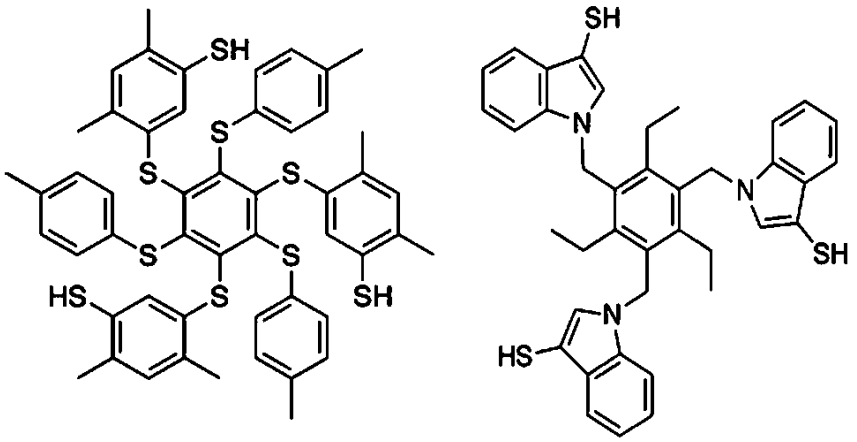

Figure 2.4. Encapsulating ligands designed by Holm and coworkers, LS_3, (left) and Pohl and coworkers, $Tri(SH)_3$ (right).

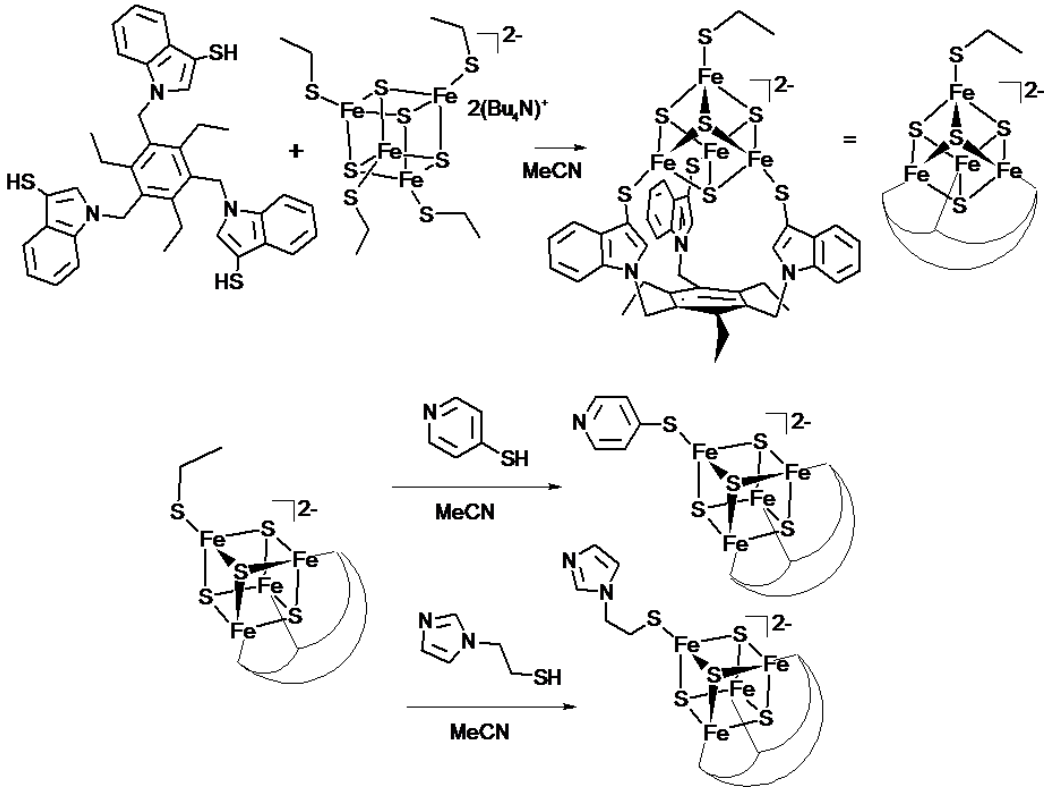

Figure 2.5. Synthetic scheme for the site-differentiated [4Fe-4S] cubane clusters with bound pyridine and imidazole linkers.

Ligand exchange of the $[Fe_4S_4(SEt)_4]^{2-}$ cluster is initiated by protonation of ethylthiolate by the incoming thiol and driven by evaporating the volatile ethanethiol in the evacuated reaction flask. The resulting site-differentiated cubane cluster has one remaining ethylthiolate ligand, which is subsequently replaced by the bridging ligand. This synthetic route is presented in Figure 2.5. The bridging ligand is designed to have an anionic thiolate for preferential binding to the [4Fe-4S] cluster and a neutral pyridine or imidazole for binding to the axial position of the metalloporphyrin. A neutral N-donor ligand is preferred for binding to the heme to minimize the propensity of ligand dissociation when the metal goes through oxidation state changes: the iron center of the ultimately desired iron porphyrin is expected to cycle through the ferric and ferrous oxidation state during substrate binding and reduction, and hence, a neutral N-donor ligand is advantageous for maintaining the structural connection to the [4Fe-4S] cluster.

Characterization by ^{1}H-NMR Spectroscopy. The ^{1}H-NMR spectra of the [4Fe-4S] cubane clusters are broad with significant paramagnetic shifts observed for the protons closest to the irons. Identifying the peaks for the new bridging ligands in $(Bu_4N)_2[Fe_4S_4(TriS)(SPy)]$ and $(Bu_4N)_2[Fe_4S_4(TriS)(SEtIm)]$ is difficult due to the significant broadening of these peaks. Fortunately, the -SEt ligand of the precursor site-differentiated cluster has a characteristic signal for the CH_2 group of the ethyl substituent at 13.08 ppm that disappears when the ethylthiolate ligand is protonated and removed. In the spectrum of $(Bu_4N)_2[Fe_4S_4(TriS)(SPy)]$ broad signals are observed for the ligand -SPy at 8.83 and 6.10 ppm (see Figure 2.6) for the two types of aromatic protons. In the spectrum of $(Bu_4N)_2[Fe_4S_4(TriS)(SEtIm)]$ broad signals for -SEtIm at 7.55, 7.13, and 6.90 (see Figure 2.7) are observed for the imidazole protons. The signal for the CH_2

protons closest to the imidazole ring is shifted down field from typical aliphatic proton signals to 4.38 ppm. Most characteristic, the CH_2 protons closest to the sulfur which ligates to the [4Fe-4S] cluster are shifted downfield to 11.92 ppm, similar to the signal observed for the -SEt ligand for $(Bu_4N)_2[Fe_4S_4(TriS)(SEt)]$ as described above. These peak shifts are reproduced over several syntheses and are real.

Noted in each spectrum are the signals assigned to the TriS ligand and those of the Bu_4N^+ counter ion. The broadening of the signals for the cluster ligands is much more pronounced compared to the counter ion signals. As a result, integration of the signals is not representative of the ratio of protons in the respective molecules due to the signal broadening.

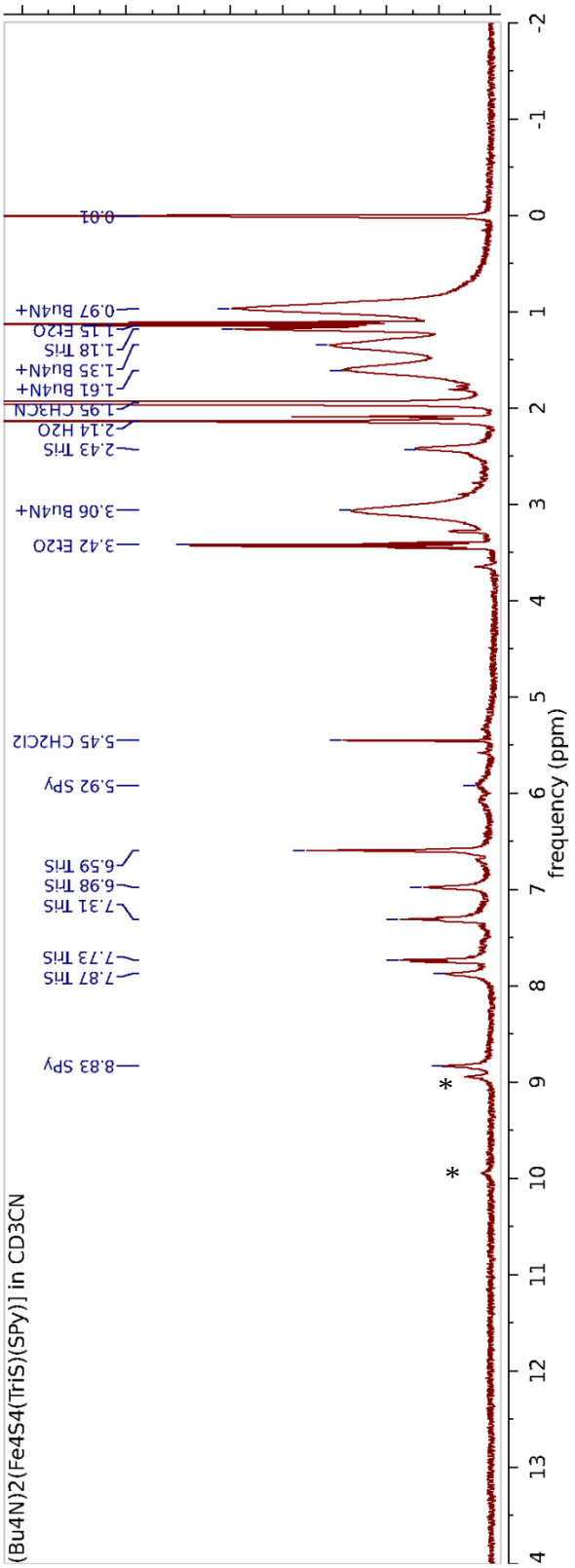

Figure 2.6. ^{1}H-NMR spectrum of $(Bu_4N)_2[Fe_4S_4(TriS)(SPy)]$. (impurities labeled by *)

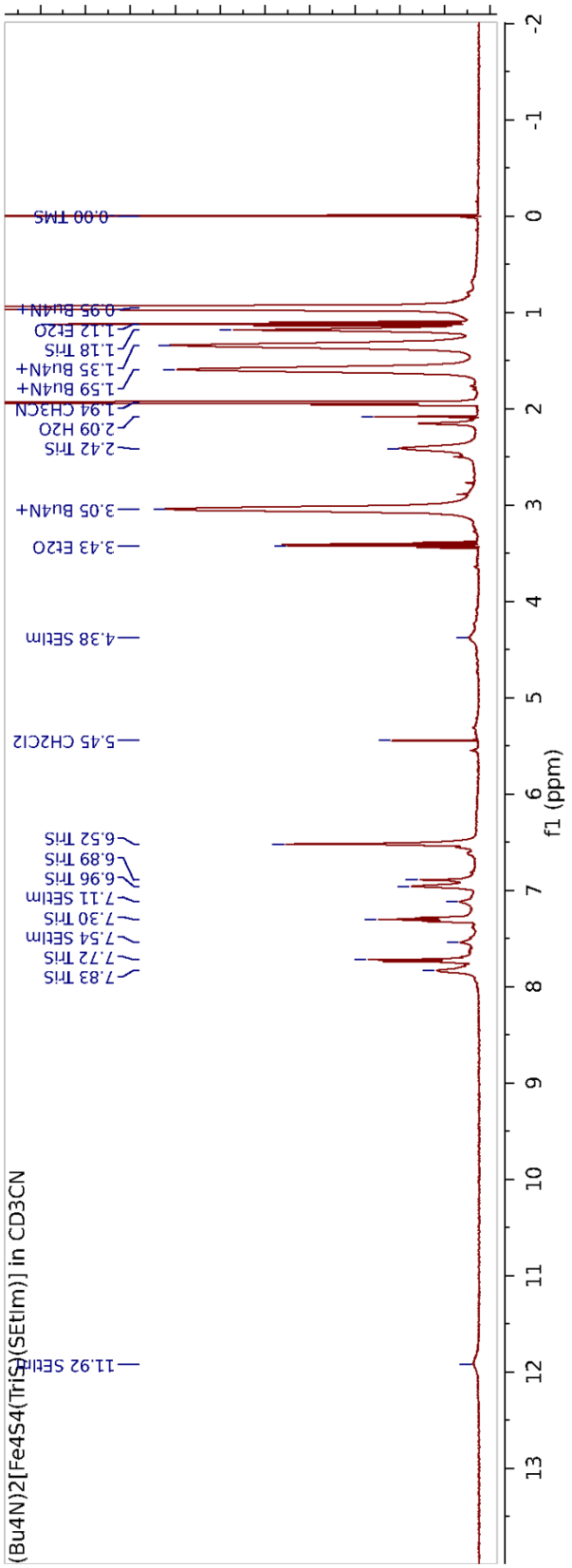

Figure 2.7. ^{1}H-NMR spectrum of $(Bu_4N)_2[Fe_4S_4(TriS)(SEtIm)]$.

Characterization by FT-IR Spectroscopy. A broad band is observed in the far-IR spectrum for each [4Fe-4S] cluster that is attributable to Fe–S vibrations, and this feature shifts with the substitution of the unique thiolate ligand. The precursor cluster $(Bu_4N)_2[Fe_4S_4(TriS)(SEt)]$ shows this vibration at 344 cm^{-1}, which shifts to 349 cm^{-1} for the -SPy ligand (Figure 2.8) and to 339 cm^{-1} for the less rigid -SEtIm ligand (Figure 2.9).

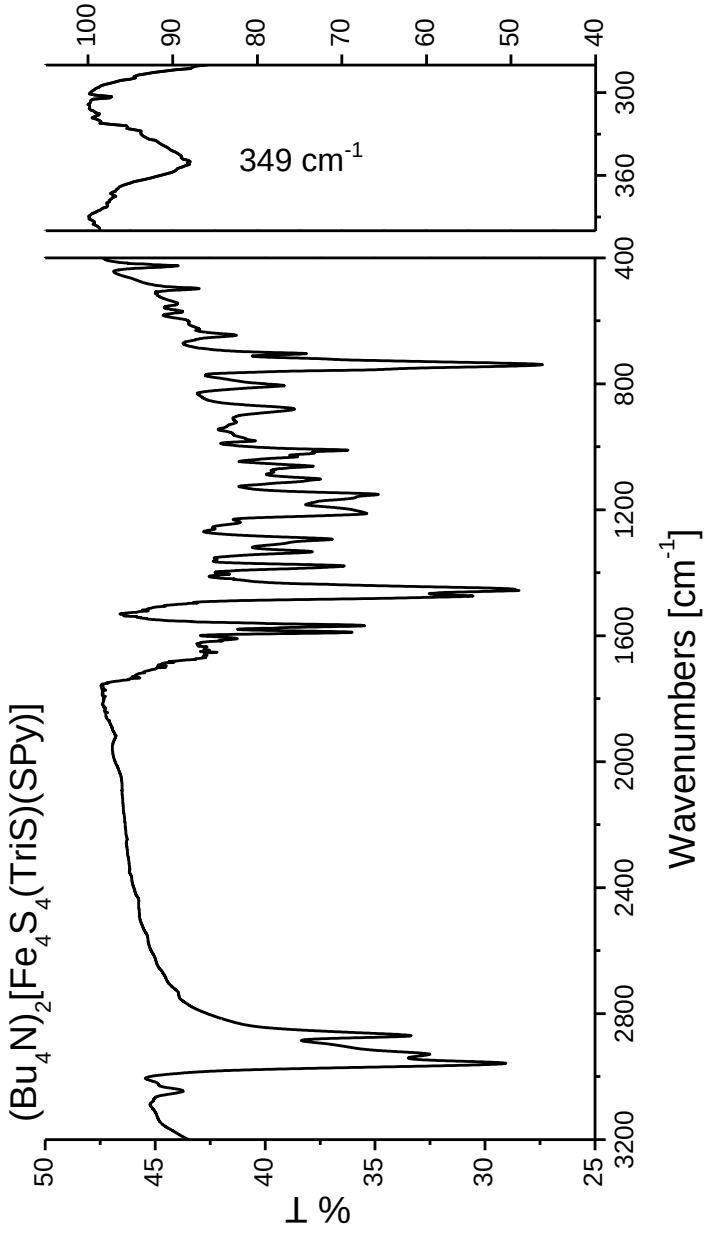

Figure 2.8. Mid- (left) and Far-IR (right) spectra of $(Bu_4N)_2[Fe_4S_4(TriS)(SPy)]$.

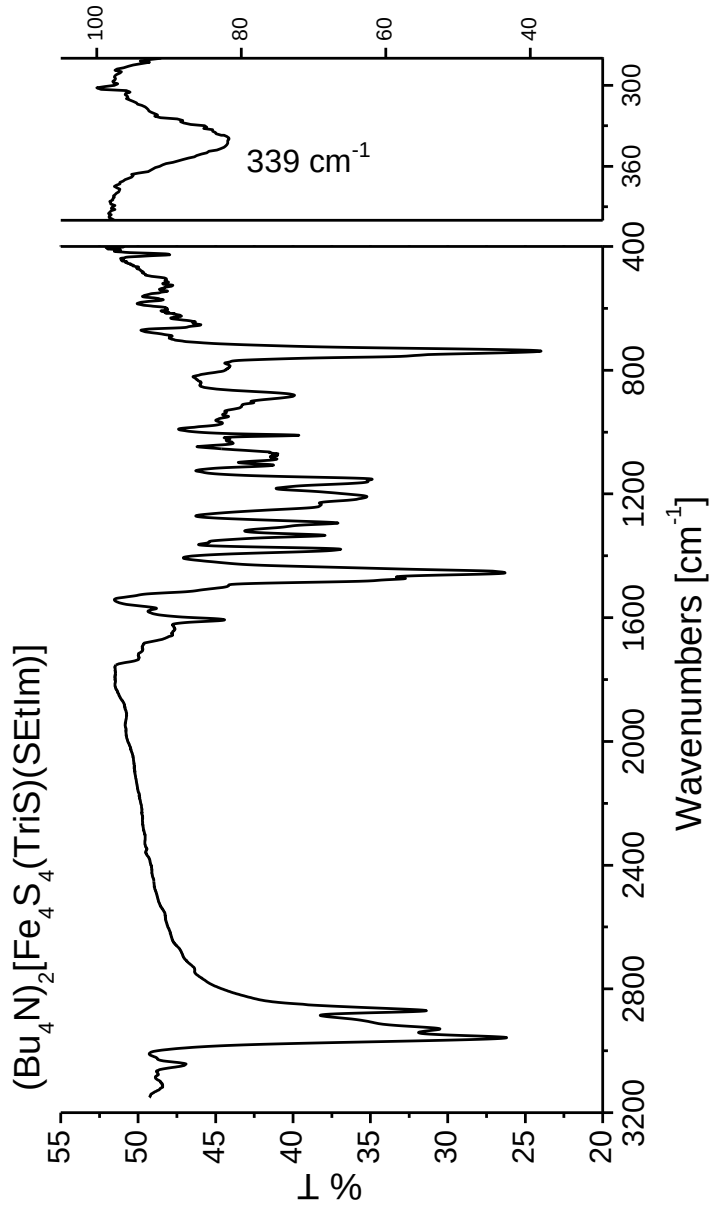

Figure 2.9. Mid- (left) and Far-IR (right) spectra of $(Bu_4N)_2[Fe_4S_4(TriS)(SEtIm)]$.

Characterization by UV/Vis Spectroscopy, LCT-MS and Elemental Analysis. The presence of the specified bi-functional thiolate ligands in these new clusters was further supported by the observation of the mass of the parent ions for these complexes in the LCT-MS data, and the elemental composition was verified by elemental analysis (see the Experimental section of this chapter).

The absorption spectra were collected for both new clusters and compared to the precursor cluster $(Bu_4N)_2[Fe_4S_4(TriS)(SEt)]$ (Figure 2.10). Although [4Fe-4S] cluster solutions are strongly colored, often opaque black, outside of the UV region, only very broad absorption signals for d-d transitions are observed.

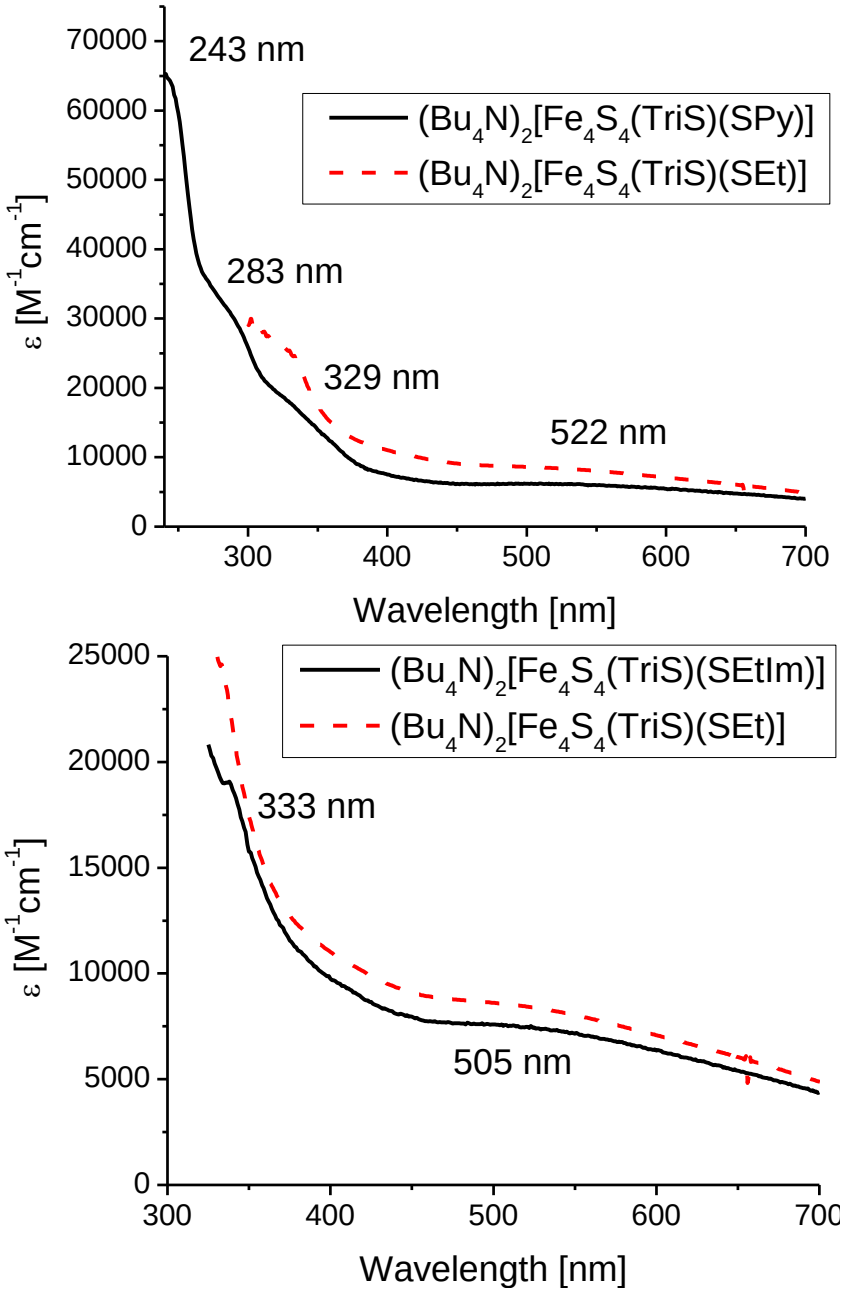

Figure 2.10. UV-Vis absorption spectra of $(Bu_4N)_2[Fe_4S_4(TriS)(SPy)]$ (top, black solid line) and $(Bu_4N)_2[Fe_4S_4(TriS)(SEtIm)]$ (bottom, black solid line) at room temperature in 1,2-dce.

Reduction Potentials Determined by CV. The new, site-differentiated $[Fe_4S_4]^{2+}$ clusters exhibit a shift of the first reduction potential to yield the corresponding $[Fe_4S_4]^{+}$ species to more positive values: the precursor cluster $(Bu_4N)_2[Fe_4S_4(TriS)(SEt)]$[10b] and the phenylthiolate cluster $(Ph_4P)_2[Fe_4S_4(TriS)(SPh)]$ [10a] are reduced at -1026 mV and at -894 mV (vs. NHE, in CH_2Cl_2), respectively. With the substitution of the pyridylthiolate and imidasolylthiolate ligands the reduction is observed more positive at -746 and -843 mV, respectively, as shown in Figures 2.11 and 2.12 and Table 2.2. This trend is due to the reduced electron density of these less electron-rich ligands as evident by the Hammett values for the substituents -Et, -Ph, and -Py (σ_p values -0.15, -0.01 and 0.44, respectively).[17] Since the Hammett value σ_p is proportional to the equilibrium constant for the acid dissociation of benzoic acid, the parameter is a meter for the electron donicity or withdrawing of the substituent. The observed trend in redox potentials follows the trend in Hammett parameters: the more positive the Hammett value of an electron withdrawing group results in a more positive reduction potential as reported previously by Holm et al. in the study of the reduction potential of [4Fe-4S] with a series of arylthiolato ligands.[18] In the series of complexes presented here, $(Bu_4N)_2[Fe_4S_4(TriS)(SPy)]$ with the most positive Hammett value has the most positive reduction potential whereas $(Bu_4N)_2[Fe_4S_4(TriS)(SEt)]$ with the most negative Hammett value has the most negative potential.

Note that the Fe^{III}/Fe^{II} reduction potential for iron porphyrins is observed in the range of -200 to -300 mV. These potentials are suitable for an electron transfer path from the iron-sulfur cluster, which is to act as the electron reservoir, to the heme that will bind

substrate for reduction. The generation of such a catalytic array, consisting of a heme with a linked [4Fe-4S] cluster, is the ultimate goal of this research.

Table 2.2. $E_{½}$ reduction potentials of relevant iron-sulfur clusters vs NHE [mV].

FeS single clusters	$[Fe_4S_4]^{2+/1+}$	$[Fe_4S_4]^{1+/0}$	Solvent
$(Bu_4N)_2[Fe_4S_4(SEt)_4]$[19]	-1076	--	MeCN
$(Bu_4N)_2[Fe_4S_4(TriS)(SEt)]$	-1026	--	CH_2Cl_2
$(Ph_4P)_2[Fe_4S_4(TriS)(SPh)]$	-894	--	CH_2Cl_2
$(Bu_4N)_2[Fe_4S_4(TriS)(SPy)]$	-746	--	MeCN
$(Bu_4N)_2[Fe_4S_4(TriS)(SEtIm)]$	-843	-1563	MeCN
	-435	--	1,2-dce

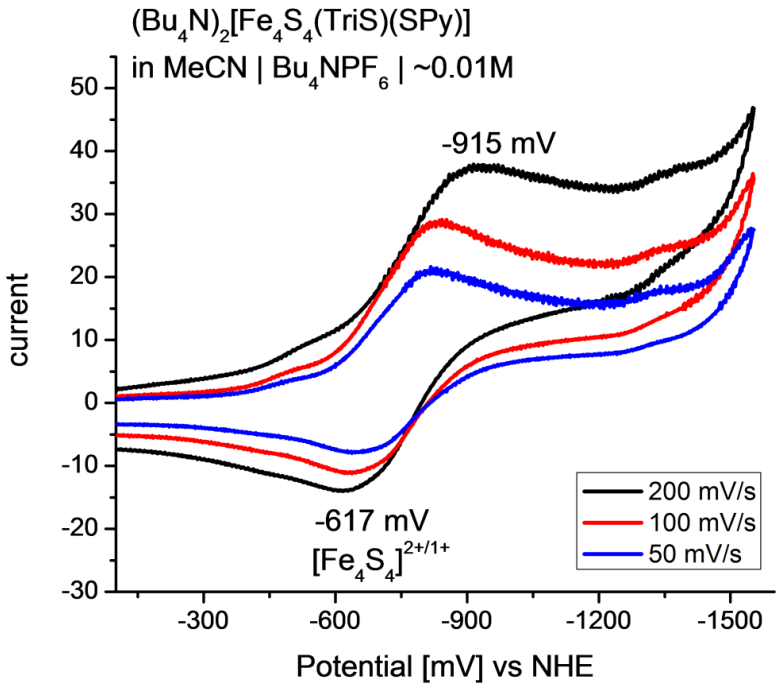

Figure 2.11. Cyclovoltammogram of $(Bu_4N)_2[Fe_4S_4(TriS)(SPy)]$ in MeCN at room temperature.

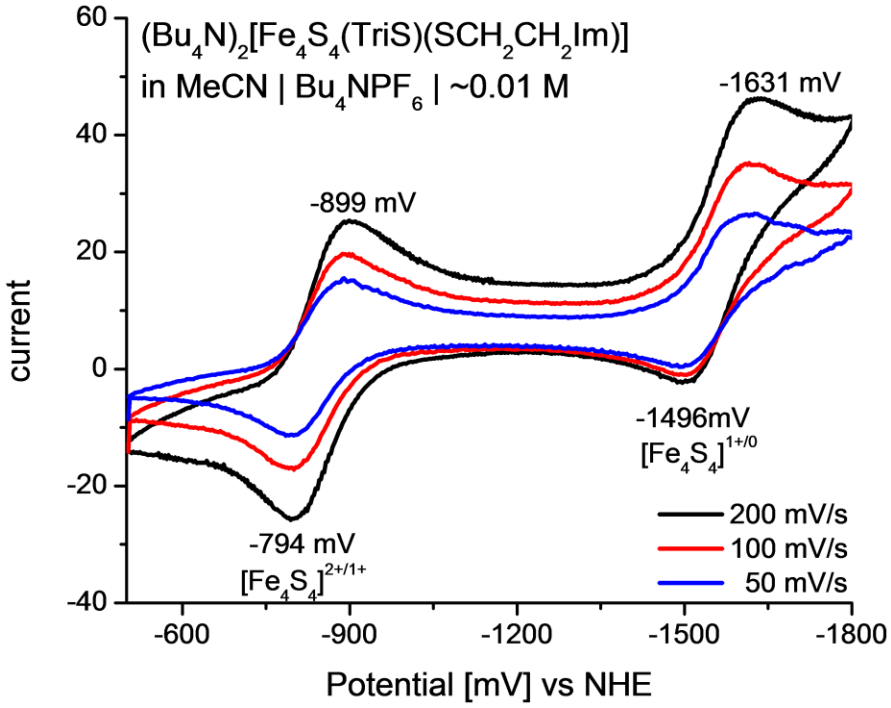

Figure 2.12. Cyclovoltammogram of $(Bu_4N)_2[Fe_4S_4(TriS)(SEtIm)]$ in MeCN at room temperature.

2.4 Axial Coordination of Functionalized Clusters and Metalloporphyrins

Binding Affinities. It is essential that the metal moieties stay attached firmly in solution in order to use our proposed [Fe_4S_4]-heme constructs for catalysis. In order to gauge the binding affinity of the functionalized [4Fe-4S] cluster to different hemes, the corresponding zinc porphyrins were used for initial titrations for their ease of preparation and non-redox active property. In addition, four-coordinate zinc porphyrins bind only one axial ligand to generate five-coordinate complexes, and this process can be followed easily with absorption spectroscopy via a characteristic red shift of the Soret and Q bands of ~10 nm (Figure 2.13 summarizes the zinc and iron porphyrins utilized).

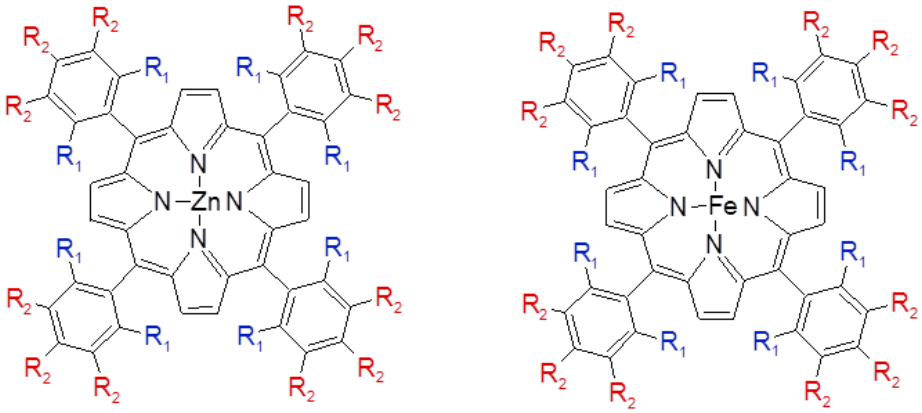

Figure 2.13. Metalloporphyrins [Zn(P)] (left) and [$Fe^{II/III}$(P)] (right) where R_1, R_2 = H : P = TPP, R_1 = F, R_2 = H : P = T*o*-F_2PP, and R_1, R_2 = F : P = T*per*-F_5PP.

Binding constants can be obtained by simply following the change in absorption when binding of an axial ligand to the four-coordinate zinc porphyrin occurs, generating a five-coordinate species (Figure 2.14). These data can then be analysed using Drago's equation (Equation 2.1), which is derived using the Lambert-Beer law, to calculate the binding constant for the introduced ligand.[20]

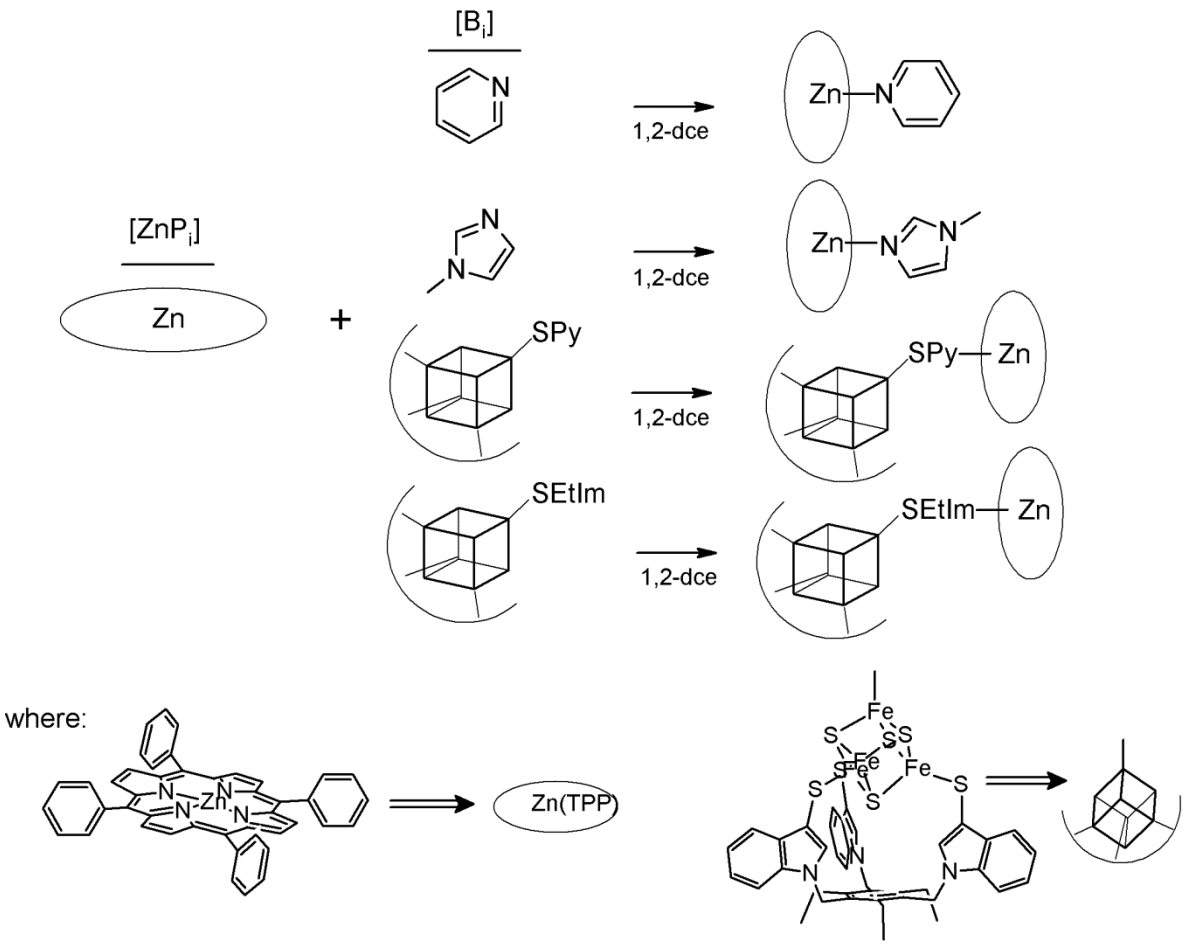

Figure 2.14. Synthetic scheme for the binding of [Zn(P)] and an axial ligand.

Equation 2.1. $$\boldsymbol{K_{eq}^{-1}} = \frac{\boldsymbol{A-A_i}}{\boldsymbol{\varepsilon_{5C}-\varepsilon_{4C}}} - [\boldsymbol{ZnP_i}] - [\boldsymbol{B_i}] + [\boldsymbol{ZnP_i}][\boldsymbol{B_i}]\frac{\boldsymbol{\varepsilon_{5C}-\varepsilon_{4C}}}{\boldsymbol{A-A_i}}$$

Here, K_{eq} is the binding constant calculated from absorption data taken at a specific wavelength, A is the total absorption of the reaction mixture, A_i is the initial absorption, ε_{5C} and ε_{4C} are the extinction coefficients of the five-coordinate and four-coordinate zinc porphyrins, $[ZnP_i]$ is the initial concentration of the zinc porphyrin, and $[B_i]$ is the initial concentration of base. Thus, by independently determining extinction coefficients of the four- and five-coordinate zinc porphyrins, correcting total concentration of the zinc

porphyrin for dilution during the titration, and recording total base concentration, the binding constant can be calculated. The titrations with the functionalized cubane clusters further required subtraction of the absorbance of the cubane cluster from the titration data to obtain accurate changes in absorption for the porphyrin signals. Additionally, the extinction coefficients of the five-coordinate zinc porphyrins with bound clusters are unknown and therefore, these were assumed to be identical to those of the complexes [Zn(P)(MI)] and [Zn(P)(py)] for $(Bu_4N)_2${Zn(P)-[Fe_4S_4(TriS)(SEtIm)]} and $(Bu_4N)_2${Zn(P)-[Fe_4S_4(TriS)(SPy)]}, respectively, for the purposes of calculating binding constants.

Table 2.3. Binding constants (K_{eq}) of [Zn(P)] and an added base [M^{-1}].

Base	[Zn(TPP)]	[Zn(T*o*-F_2PP)]	[Zn(T*per*-F_5PP)]
Pyridine (py)	5,220	20,300	77,900
1-Methylimidizole (MI)	56,800	204,000	819,000
$(Bu_4N)_2$[Fe_4S_4(TriS)(SPy)]	na[a]	7,540	13,200
$(Bu_4N)_2$[Fe_4S_4(TriS)(SEtIm)]	17,100	26,200	124,000

[a] Titration not performed due to low binding affinity

To compare binding affinities, MI and py, which are similar to -SEtIm and -SPy used in the clusters, were also titrated against the zinc porphyrins and binding constants were calculated. Table 2.3 includes all of the experimentally determined K_{eq} values for the titrations of zinc porphyrins, and the absorption plots for the titrations are included in Figures 2.15-2.18. The attained K_{eq} values for [Zn(T*o*-F_2PP)(MI)] and $(Bu_4N)_2${[Zn(T*o*-F_2PP)[Fe_4S_4(TriS)(SEtIm)]} were then used to recalculate the concentration of the five-coordinate zinc porphyrin-cluster complex and of the four coordinate zinc porphyrin. The total absorbance for each titration point was calculated and plotted together with the

experimental total absorbance vs. molar equivalents of base added (insets plots in Figure 2.17). Overall, the calculated and the experimental absorbances match well for the K_{eq} values determined here.

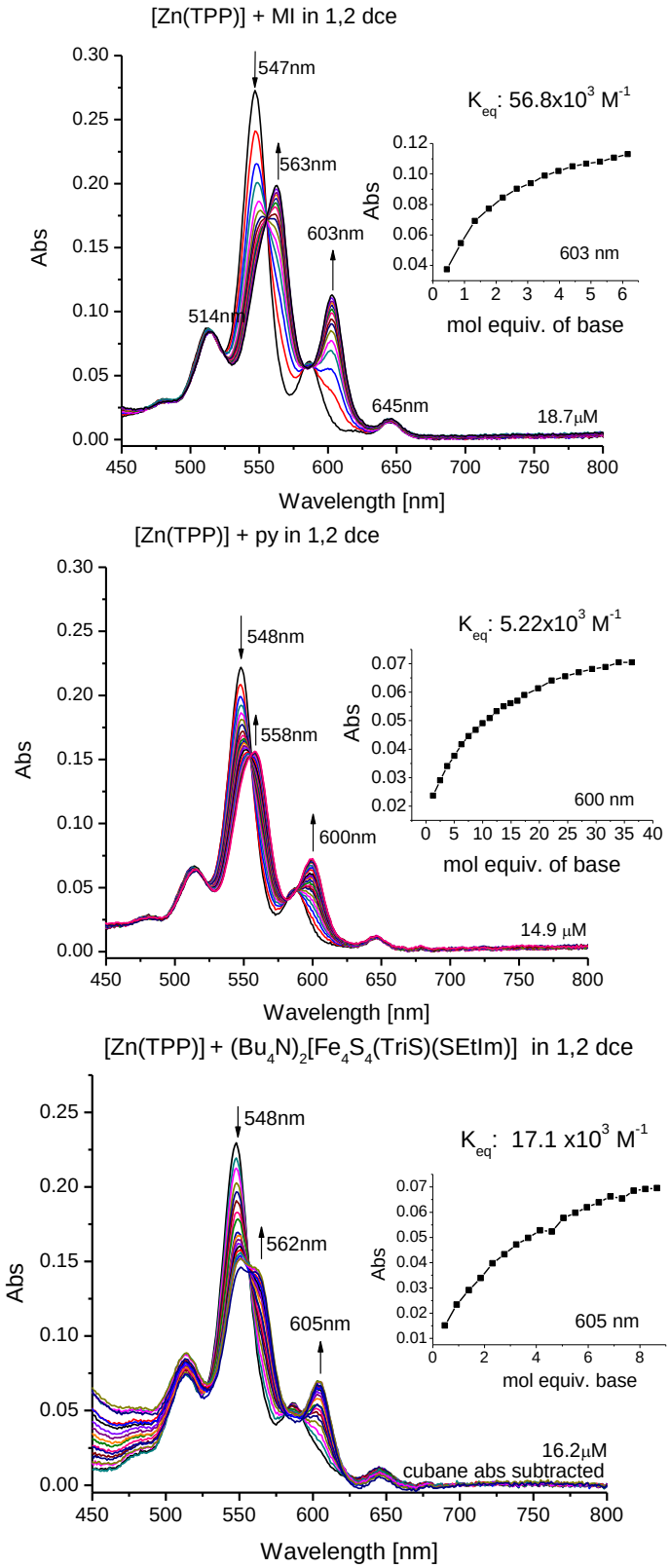

Figure 2.15. Titration plots for [Zn(TPP)] with MI (top), py (middle), and $(Bu_4N)_2$ $[Fe_4S_4(TriS)(SEtIm)]$ (bottom) for the determination of binding constants at 26 °C.

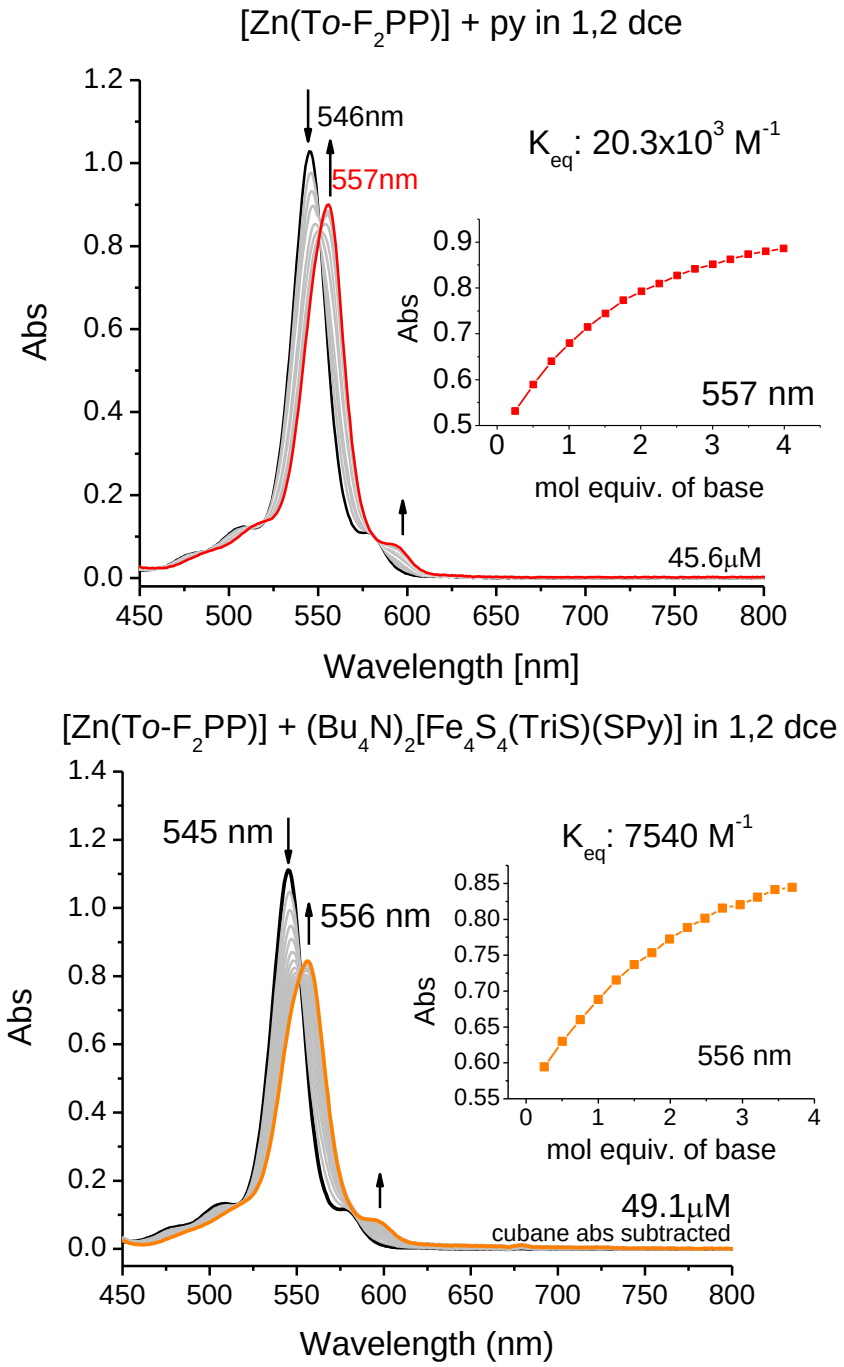

Figure 2.16. Titration plots for [Zn(To-F_2PP)] with pyridine (top), and $(Bu_4N)_2[Fe_4S_4(TriS)(SPy)]$ (bottom) for the determination of binding constants at 26 °C.

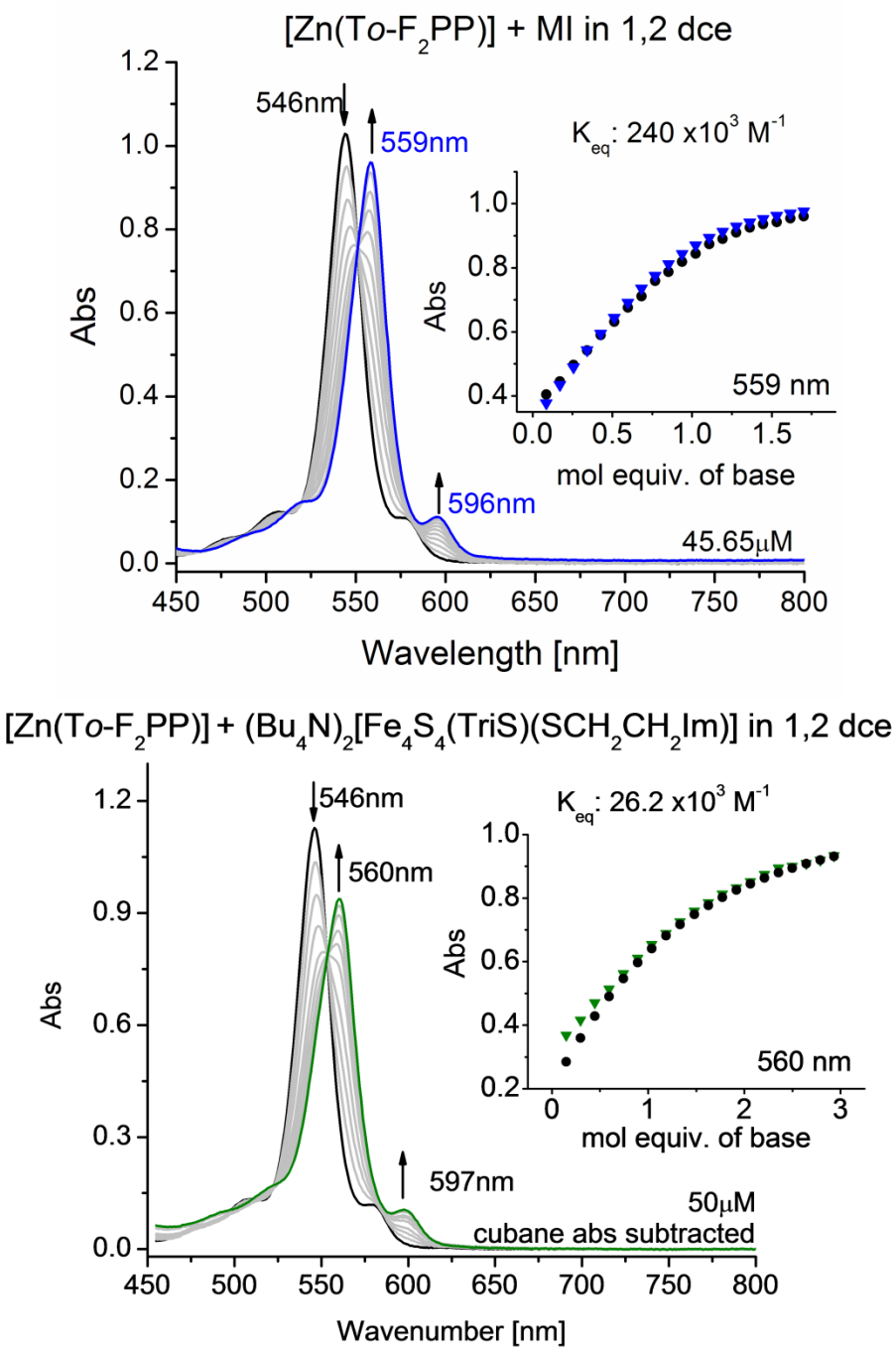

Figure 2.17. Absorption spectra for the titrations of [Zn(T*o*-F_2PP)] with 1-methylimidazole (top) including a comparison plot of the total experimental absorption ▼ vs the calculated total absorption ● from the derived K_{eq} value (inset), and with $(Bu_4N)_2[Fe_4S_4(TriS)(SEtIm)]$ (bottom) including a comparison plot of the total experimental absorption ▼ vs the calculated total absorption ● from the derived K_{eq} value (inset). Both experiments were conducted in in 1,2-dichloroethane (1,2-dce) at 26 °C.

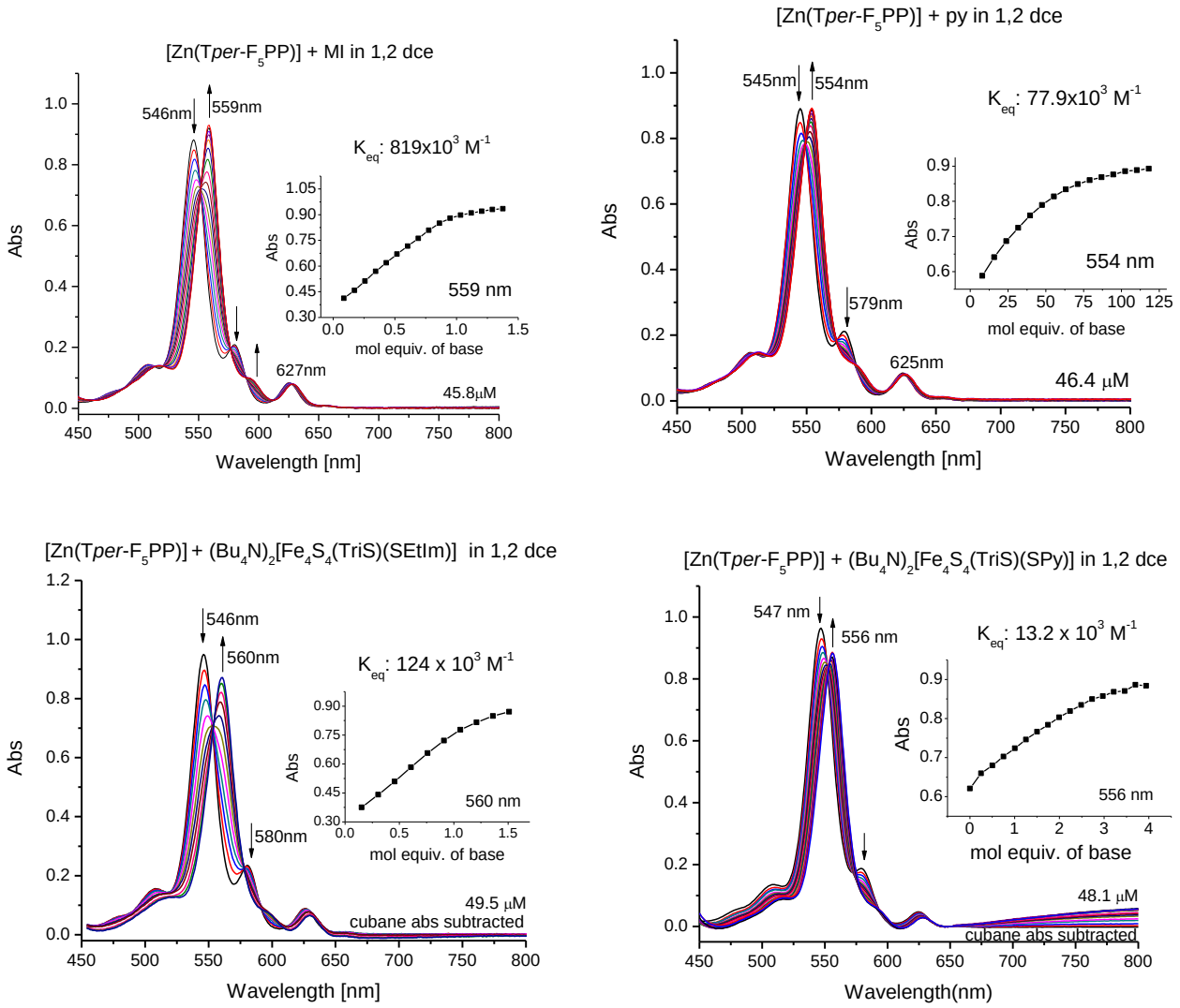

Figure 2.18. Titration plots for [Zn(T*per*-F_5PP)] with 1-methylimidazole (top, left), pyridine (top, right), $(Bu_4N)_2[Fe_4S_4(TriS)(SEtIm)]$ (bottom, left), and $(Bu_4N)_2[Fe_4S_4(TriS)(SPy)]$ (bottom, right) for the determination of binding constants at 26 °C.

The increase in binding affinity of axial ligands for metalloporphyrins with electron withdrawing groups at the ortho positions of the meso-phenyl substitutions has been observed previously.[21] In these cases, it is thought that the electron density is drawn to the periphery of the porphyrin ring in the presence of the electron-withdrawing groups causing the porphyrin ring nitrogens to decrease in donicity and in this way, the

effective nuclear charge of the metal is increased. A strong σ-donor such as the N-donor ligands applied here will thus bind stronger to the open axial position in the fluorinated porphyrins. This trend is reproduced here: with increasing number of electron withdrawing fluorides present at the meso-phenyl rings, a distinct increase in the binding constant of base to the metalloporphyrins is observed. When pyridine is added to [Zn(TPP)], a binding constant of 5,220 M^{-1} is determined for forming the five-coordinate complex [Zn(TPP)(py)]. This value matches well with previously reported value of 6,025 M^{-1} in benzene.[22] The analogous titrations with pyridine added to [Zn(T*o*-F_2PP)] and [Zn(T*per*-F_5PP)] (T*per*-F_5PP^{2-} = *meso*-tetra(penta-fluorophenyl)porphyrin dianion) result in binding constants of 20,300 and 77,900 M^{-1}, respectively. Hence, a four-fold increase in binding constant is observed in going from [Zn(TPP)] to [Zn(T*o*-F_2PP)], which further increases four-fold in [Zn(T*per*-F_5PP)]. The same relative increase in binding constant is observed for this series of zinc porphyrins when 1-methylimidazole is used as base; see Table 2.3. Thus, both of the fluorinated metalloporphyrins are the better options for obtaining heme-cluster adducts that are firmly attached in solution.

In comparing the binding constants determined for pyridine versus 1-methylimidazole for the same zinc porphyrin, the value for the imidazole ligand is always higher by an order of magnitude. [Zn(TPP)] binding with py versus MI affords binding constants of 5,220 and 56,800 M^{-1}, respectively. For [Zn(T*o*-F_2PP)], the binding constants for py and MI are 20,300 and 204,000 M^{-1}, respectively, and for [Zn(T*per*-F_5PP)], the values for py and MI are 77,900 and 819,000 M^{-1}, respectively. Imidazole is a stronger base than pyridine (pKa values of 6.95 and 5.14, respectively),

and therefore, facilitates an increase in binding affinity by forming a stronger σ-bond to the heme, as evident from the binding constants determined here.[23]

Similar trends are also observed for the thiopyridine- and thioethylimidazole-functionalized [4Fe-4S] clusters. For the addition of $(Bu_4N)_2[Fe_4S_4(TriS)(SPy)]$ to [Zn(T*o*-F_2PP)] and [Zn(T*per*-F_5PP)], binding constants of 7,500 and 13,200 M^{-1}, respectively, were determined. A distinct increase in binding affinity is also found when $(Bu_4N)_2[Fe_4S_4(TriS)(SEtIm)]$ is used: for [Zn(TPP)], [Zn(T*o*-F_2PP)] and [Zn(T*per*-F_5PP)] increasing binding constants of 17,100, 26,200 and 124,000 M^{-1}, respectively, were obtained along this series of zinc porphyrins. This corresponds to an increase in K_{eq} of 1.5 and 7.3 relative to [Zn(TPP)]. Likewise, the increased binding affinity for the imidazole-equipped cluster versus the pyridine-containing cluster is apparent from the determined binding constants.

Unfortunately, the binding constants decrease strongly for the pyridine- and imidazole-bound cluster versus the corresponding free ligands. For example, comparison of the binding constants for py versus $(Bu_4N)_2[Fe_4S_4(TriS)(SPy)]$ to [Zn(T*o*-F_2PP)] shows an 2.6-fold decrease in the binding constant from 20,300 to 7,540 M^{-1}, respectively, for the cluster-bound pyridine ligand. Kirksey and coworkers have reported similar observations in the study of substituted pyridines binding to [Zn(TPP)], where the addition of deactivating groups to the pyridine decreases the binding constant.[22] For example, 4-cyanopyridine results in a K_{eq} value of 794 M^{-1} as compared to 6025 M^{-1} for pyridine with [Zn(TPP)] in benzene. Although one would expect that 4-thiopyridine would increase the binding constant because thiols are activating groups, the observed decrease in binding constant must thus be attributed to the electron withdrawing,

deactivating effect of the bound iron-sulfur cluster. Additionally, we believe that this decrease in K_{eq} for the pyridine- and imidazole-bound clusters is in part due to unfavourable steric interactions of these bulky ligands with the zinc porphyrins used here.

In order to better visualize the interaction of the complexes in the bound form to assess the extent of steric interference, structures submitted to the Cambridge Structural Database (CSD) of [Zn(TPP)(py)] • C_6H_{14} and $(Ph_4P)_2[Fe_4S_4(TriS)(SPh)]$ • 2DMF were used to model the most plausible orientation of the bound complex anion $\{Zn(TPP)\text{-}[Fe_4S_4(TriS)(SPy)]\}^{2-}$.[10a, 24] Using the software Mercury CSD 3.0, for both structures the excess solvent molecules and the counter ions for the cluster were omitted as well as all hydrogen atoms. The -SPh ligand of the cubane cluster anion $[Fe_4S_4(TriS)(SPh)]^{2-}$ was aligned to overlay pyridine ring in the structure of [Zn(TPP)(py)]. Lastly, the C_6H_5 phenyl ring was deleted from the -SPh ligand as well as the hydrogen atom at the *para* position of the pyridine ring bound axially to the zinc atom. The resulting structural fit is presented in Figure 2.19. The resulting images of the structural fit indicate that the encapsulating TriS ligand is not in direct contact with the plane of the porphyrin ligand or the phenyl substituents of the porphyrin ring.

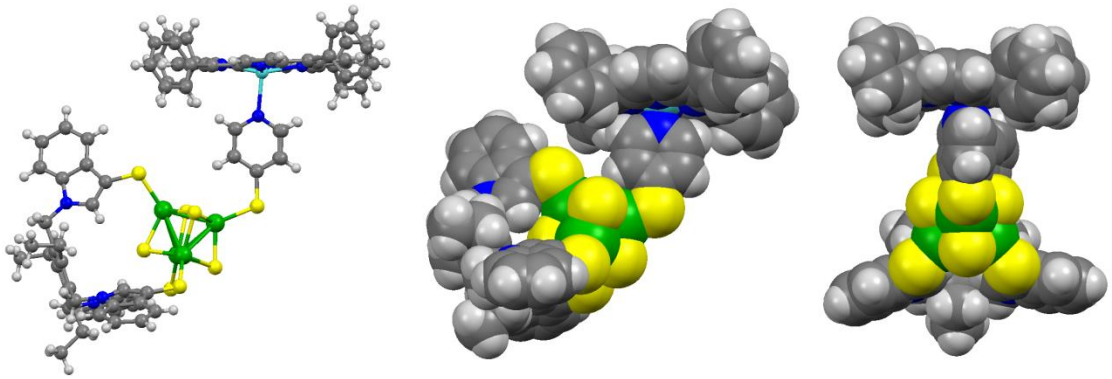

Figure 2.19. Structural representation of the bound complex anion $\{Zn(TPP)\text{-}[Fe_4S_4(TriS)(SPy)]\}^{2-}$ as ball and stick (left), space fill side view (middle), and space fill end view (right).

Although the structural fit indicates that steric hindrance is not prohibiting binding from occurring, the bulkiness of the encapsulated cubane cluster with the bridging ligand is likely the cause of the lowered binding constants for the ligated clusters vs. the free reference ligands. The bridging ligand is a small fraction of the surface area of the cubane complex that needs to be oriented in order to bind to the metalloporphyrin. In the interaction of [Zn(P)] with $[Fe_4S_4(TriS)(SEtIm)]^{2-}$ the -SEtIm ligand has the advantage of the extra carbons of the ethyl chain which aid to separate the bridging ligand from the bulky encapsulating ligand of [4Fe-4S]. Thus, the binding of [Zn(P)] with $[Fe_4S_4(TriS)(SEtIm)]^{2-}$ vs. [Zn(P)] with MI results in less of a decrease in the binding constant as compared to the binding of interaction of [Zn(P)] with $[Fe_4S_4(TriS)(SPy)]^{2-}$ vs. [Zn(P)] with py.

The largest binding constants are found for the imidazole-substituted cluster in combination with the fluorinated metalloporphyrins using our screening experiments. Either fluorinated porphyrin is able to provide stable complexes in solution when the imidazole-functionalized cluster is used. However, the [M(T*per*-F_5PP)] metalloporphyrins have a high solubility to the extent that isolating the heme-cluster adduct from solution by crystallization is likely difficult. Therefore, for these practical reasons, the [M(T*o*-F_2PP)] metalloporphyrins are most suitable for further large scale preparations and spectroscopic investigations of the heme-cluster adducts. For example, for a typical reaction of [Zn(T*o*-F_2PP)] and $(Bu_4N)_2[Fe_4S_4(TriS)(SEtIm)]$ at room temperature with heme and cluster concentrations of about 50 mM, the calculated ratio of bound to unbound complex is 97.3:1.

Cyclovoltammetry of the Complete [4Fe-4S]-Heme Complex. An important property of the bound metalloporphyrin-iron-sulfur cluster array is the ability to transfer electrons from the electron reservoir, the [4Fe-4S] cluster, to the heme. In the SIR/NIR enzymes the [4Fe-4S] cluster is at a more negative reduction potential than the heme as previously indicated (see Introduction). Additionally, the two metal centers are electronically coupled which supports fast electron transfer through the sulfide bridge.[25] In our case, the complex of the [4Fe-4S] cluster and [Zn(T*o*-F_2PP)] does not contain a redox active metal in the macrocycle for catalytic activity. Therefore, any reductions occurring at the metalloporphyrin are localized on the porphyrin ring. Individually, semi-reversible one-electron reduction events within the scanned potential range occur for the cluster at $E_{½}$ of -435 mV and the zinc porphyrin at $E_{½}$ of -1110 mV in 1,2-dce (vs. NHE). Interestingly, when an equivalent of zinc porphyrin is added (in one-fifth increments) to $(Bu_4N)_2[Fe_4S_4(TriS)(SEtIm)]$, the reduction event of the iron-sulfur cluster shifts more negative to -565 mV for a total difference in potential of 130 mV. The porphyrin ring reduction does not differ upon binding to the [4Fe-4S] cluster as shown in Figure 2.20.

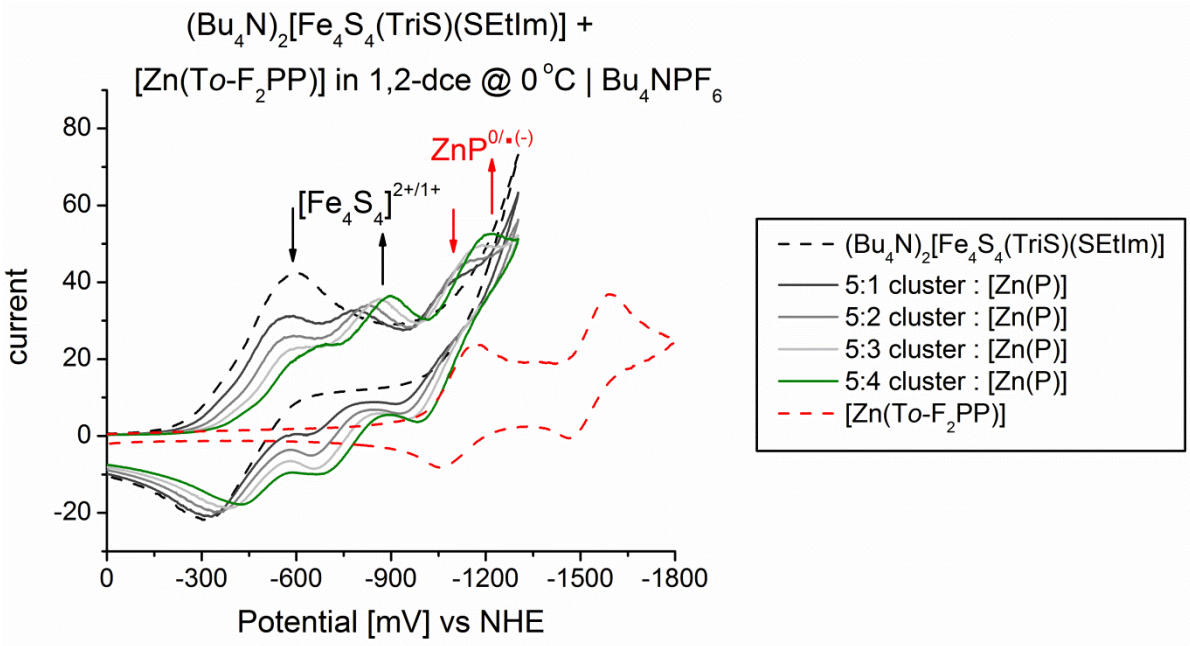

Figure 2.20. Cyclovoltammogram for the titration of 5 mM $(Bu_4N)_2[Fe_4S_4(TriS)(SEtIm)]$ with [Zn(T*o*-F_2PP)] in 1,2-dichloroethane (1,2-dce).

Keeping in mind that the electronic coupling between the heme and the [4Fe-4S] cluster in our complexes is relatively weak compared to the sulfide bridged SIR/NIR cofactor, the large negative shift in cluster potential observed upon heme binding must simply be due to the presence of the heme in close proximity to the cluster. It is in fact known that the first reduction of $(Bu_4N)_2[Fe_4S_4(TriS)(SEtIm)]$ shows a strong dependence on the medium. For example, the redox potential in the polar, coordinating solvent acetonitrile is observed at -843 mV as opposed to the less polar, non-coordinating solvent 1,2-dce where this potential is -435 mV, as reported above, which is a remarkably large effect of the environment. Nature uses ferredoxins in a range of reduction potentials which are highly tuned by the surrounding protein environment.[26] Likewise, the reduction potential of synthetic ferredoxins is tuneable by the bound ligands, the electrolyte of the solution, and the polarity of the solvent.[19] Holm and coworkers

reported the effect of various ligand substitutions at [4Fe-4S] clusters on reduction potentials. A substantial positive shift in the reduction potential of 90 mV is reported for their site-differentiated cluster when the unique ligand SPh^- is substituted for $[SPh\text{-}p\text{-}NO_2]^-$, resulting in reduction potentials of -1,060 mV and -970 mV (vs. NHE), respectively.[19] Thus, the presence of strongly electron-withdrawing groups at the unique ligand can cause a positive shift in the reduction potential for the $[Fe_4S_4]^{2+/1+}$ event. Interestingly, titration of the functionalized site-differentiated [4Fe-4S] cluster with [Zn(T*o*-F_2PP)] in 1,2-dce causes a shift of the reduction potential of the cluster into the negative range (see Figure 3), closer to the value found for MeCN. Since the coupling between the heme and the cluster across the $^-S\text{-}CH_2\text{-}CH_2$-Im bridge is likely weak, this implies an increase of the polarity of the cluster environment upon heme binding, which would then be responsible for the shift in the redox potential of the cluster.

Bulk Scale Reactions. Synthesis of the bound complex $(Bu_4N)_2${Zn(T*o*-F_2PP)-$[Fe_4S_4$(TriS)(SEtIm)]} on a large scale for isolation of bound material and crystal growth for structure determination by x-ray crystallography was repeatedly attempted at concentrations of >50 mM. Thus, at these concentrations >97% of the bound complex is produced in solution. Absorption spectra of these solutions clearly indicate that the heme-cluster complex is formed under these conditions, as indicated by shifts of the Q bands of the metalloporphyrin. IR spectra further confirm that both [Zn(T*o*-F_2PP)] and the iron-sulfur cluster are present in precipitated solids, isolated from these reaction mixtures indicating no decomposition. Continuous efforts to finally attain a crystal structure of the complete catalytic array have unfortunately been fruitless.

Reaction of Ferric Heme with [4Fe-4S] Cluster. Although forming bound complex arrays with the [Zn(P)] is useful for screening experimental conditions and properties of the bound cubane cluster, in order to complete the design of the catalytic array iron porphyrins were used to emulate the catalytic site component of our aSIR model. Ferric heme was first used to observe binding of the functionalized encapsulated cubane clusters. It has been shown that there is a strong binding affinity for ferric heme with N-donor ligands.[21a] However, when reacting the cluster $(Bu_4N)_2[Fe_4S_4(TriS)(SEtIm)]$ with ferric hemes under the same conditions, decomposition of the iron-sulfur clusters occurs as indicated by EPR experiments and by a loss of all spectroscopic signals characteristic for the starting clusters (Figure 2.21). Attempts to collect product with ferrous hemes is on-going, but is challenging due to the high sensitivity of ferrous heme in 1,2-dce toward trace dioxygen resulting in the same observations where ferric hemes are used directly as reactants.

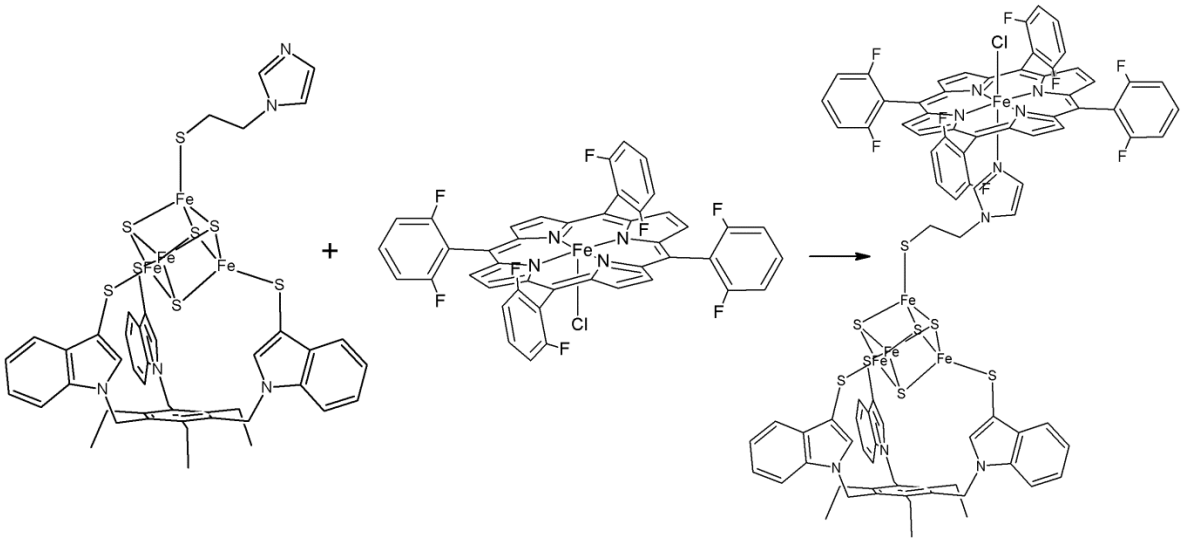

Figure 2.21. The reaction scheme for ferric heme $[Fe^{III}(To\text{-}F_2PP)Cl]$ and $(Bu_4N)_2[Fe_4S_4(TriS)(SEtIm)]$ with the intended bound product shown and the actual product being decomposition.

The screening of the binding constants using zinc porphyrins indicated that [M(T*o*-F_8PP)] gives the highest binding affinity and is most practical to use. In addition, both ferric and ferrous porphyrins have strong binding constants with neutral N-heterocycles.[21a] Typically, the $[Fe_4S_4]^{2+}$ cluster is EPR silent with a spin state of S = 0 and high-spin ferrous heme has an integer spin of S=2. When bound, the complex is expected to remain EPR silent as well, thus the following experiment was expected to show EPR silent spectra throughout.

The susceptibility of $[Fe^{II}$(T*o*-F_8PP)] to oxidation became evident as reactions with intended ferrous heme complexes resulted in substantial decomposition of the clusters (Figure 2.22). When equal equivalents of stock solutions of $(Bu_4N)_2[Fe_4S_4$(TriS)(SEtIm)] and what was thought to be $[Fe^{II}$(T*o*-F_8PP)] (but is more likely to be a mixture of ferrous and ferric heme due to oxygen contamination and will be referred to as "$[Fe^{III}$(T*o*-F_8PP)X]") were combined, the initial EPR silent [4Fe-4S] cluster reduces the ferric heme. Since the redox potentials of the two components are not thermodynamically suited for spontaneous reduction of the heme, this likely indicates decomposition of the cluster prior to heme reduction. The reduction of the ferric heme contaminant is evident from the loss of the high spin S = $^5/_2$ signal and the growth of a new EPR signal likely representing an S = ½ decomposition product of the [4Fe-4S] cluster (Figure 2.23).

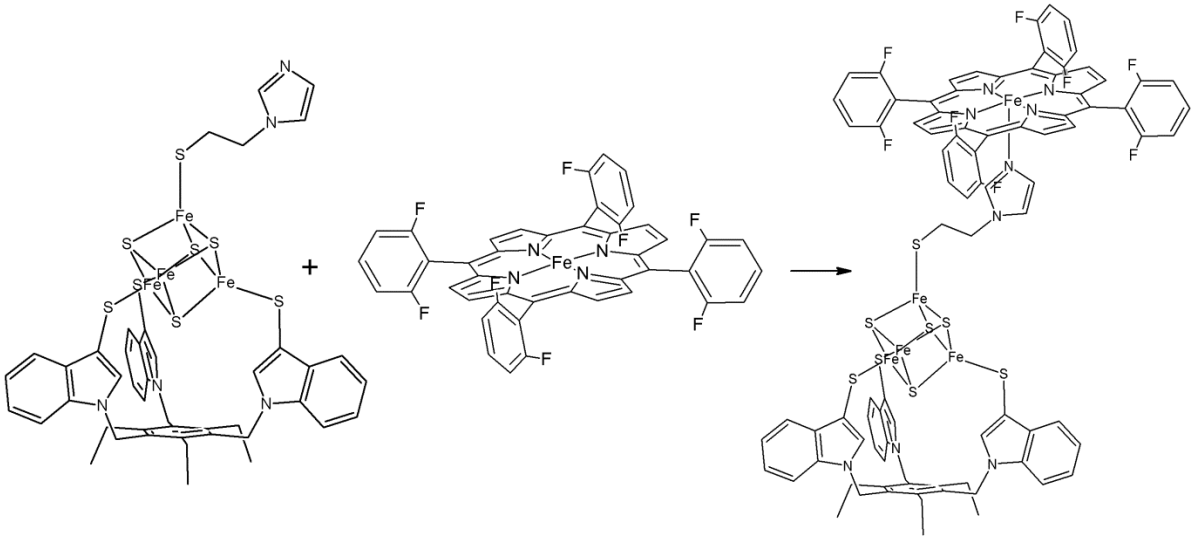

Figure 2.22. The reaction scheme for ferrous heme [Fe^{II}(T*o*-F_2PP)] and $(Bu_4N)_2[Fe_4S_4(TriS)(SEtIm)]$ with the intended bound product shown.

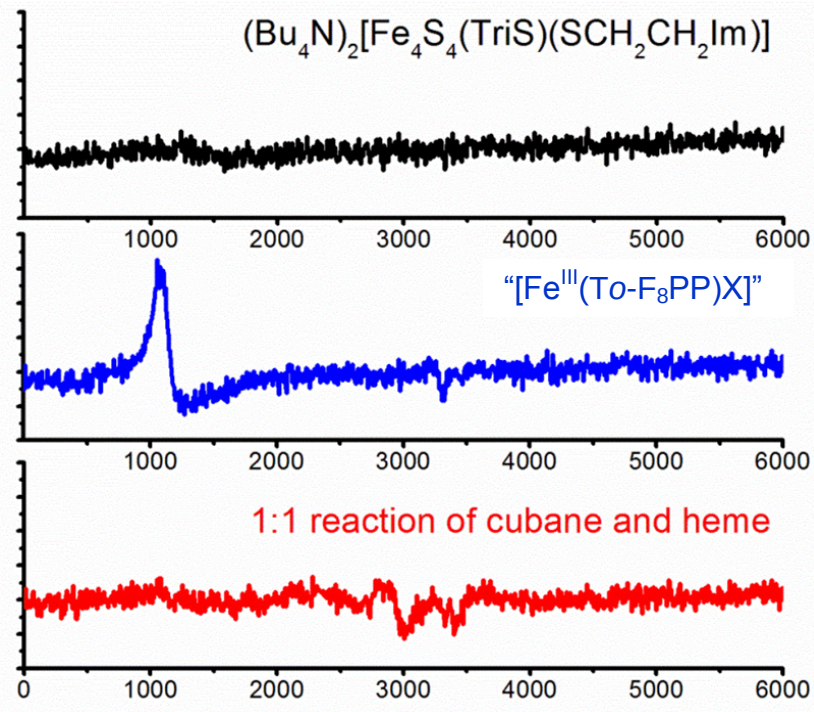

Figure 2.23. EPR spectra of $(Bu_4N)_2[Fe_4S_4(TriS)(SEtIm)]$ (top, black), "[Fe^{III}(T*o*-F_8PP)X]" (middle, blue), and the 1:1 mixture (bottom, red) in MeCN taken at lq. N_2 temperature.

The follow up reaction of $(Bu_4N)_2[Fe_4S_4(TriS)(SEtIm)]$ and $[Fe^{III}(To\text{-}F_8PP)Cl]$ under similar conditions yielded the same reduction of the ferric heme signal (Figure 2.21). To confirm this, half of an equivalent of the cluster was added to the ferric heme and as expected, only half the EPR signal from the heme was lost (Figure 2.24).

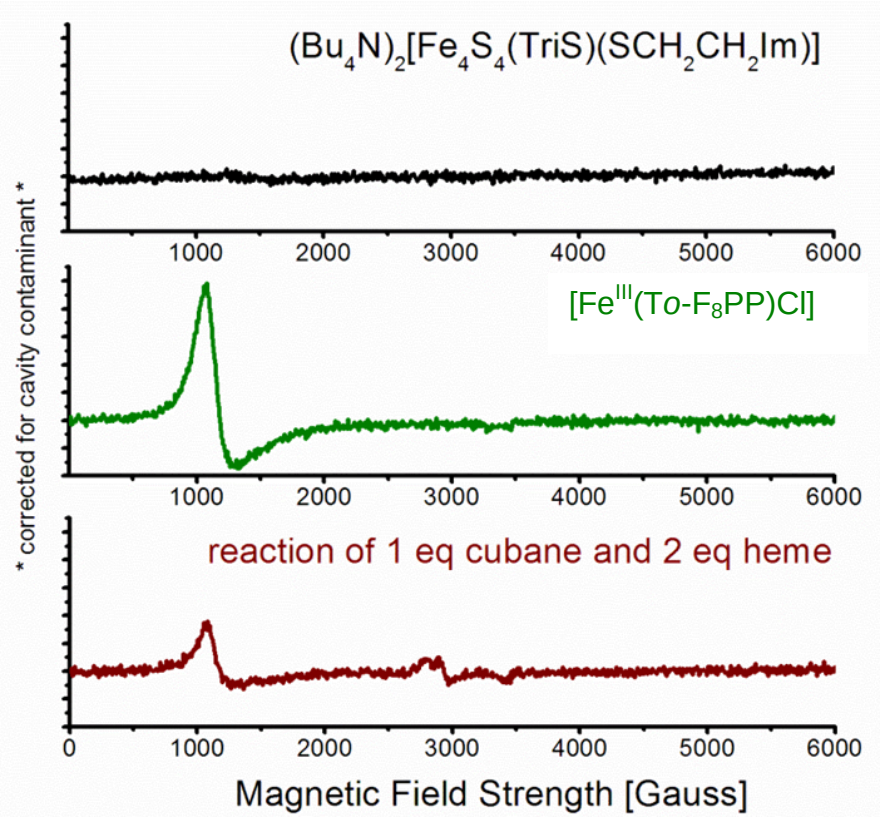

Figure 2.24. EPR spectra of $(Bu_4N)_2[Fe_4S_4(TriS)(SEtIm)]$ (top, black), $[Fe^{III}(To\text{-}F_8PP)Cl]$ (middle, blue), and the 1:1 mixture (bottom, red) in MeCN taken at lq. N_2 temperature.

The suspected reduction of the ferric porphyrin mixture is further supported by the absorption data collected for the titration of a solution of "$[Fe^{III}(To\text{-}F_8PP)X]$" with a solution of $(Bu_4N)_2[Fe_4S_4(TriS)(SEtIm)]$. The initial Soret band at 407 nm, which is representative for the ferric μ-oxo heme, clearly diminishes and a new Soret grows in at

422 nm indicative of ferrous heme formation (Figure 2.25). The cluster is reducing the ferric species in solution.

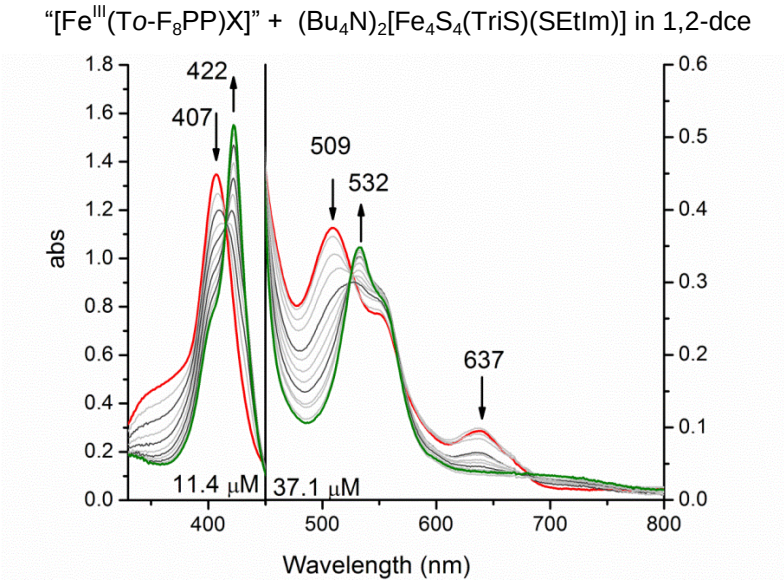

Figure 2.25. UV/Vis spectrum of "[Fe^{III}(T*o*-F_8PP)X]" (red solid line) titrated with $(Bu_4N)_2[Fe_4S_4(TriS)(SEtIm)]$ (left panel: each line represents half mol. equiv.; right panel: each line represents fifth mol. equiv.) corrected for the absorption of the cluster. The red line indicates the last addition of five equivalents of cluster to the heme solution (left), and three equivalents of cluster to the heme solution (right).

Furthermore, repeated crystallization attempts to afford the bound heme-cluster complex $(Bu_4N)_2\{Fe^{II}$(T*o*-F_2PP)-$[Fe_4S_4(TriS)(SEtIm)]\}$ in 1,2-dce resulted in amorphous solids with IR spectra indicating porphyrin and iron-sulfur complexes were likely present. One reaction crystallization attempt produced two different crystals, red plate crystals and black rod crystals, along with the typical amorphous deposits. Both crystals diffracted well and their structures were determined with the hope that bound heme and cluster would be found in either crystal.

The black rod crystals were identified as having two tetrabutylammonium counter ions per one [4Fe-4S] cluster ligated by a single heavy atom, $(Bu_4N)_2[Fe_4S_4X_4]$ where X

is either Cl or S(H). The wine colored plate crystals were identified to have both a heme and iron-sulfur cluster component but not those expected. One μ-oxo ferric heme dimer was found along with two tetrabutylammonium ions and an [2Fe-2S] cluster ligated by a single heavy atom, $(Bu_4N)_2[Fe_2S_2X_4]$ where X is Cl or S(H). It should be noted that the PLATON program was used to "squeeze out" several disordered molecules for each structure: one of the two tetrabutylammonium counterions per asymmetric unit cell of $(Bu_4N)_2[Fe_4S_4X_4]$ and two tetrabutylammonium counterions and approximately one 1,2-dce per asymmetric unit cell of $[(Fe(T\textit{o}\text{-}F_2PP))_2O] \bullet (Bu_4N)_2[Fe_2S_2X_4] \bullet 2$(1,2-dce) were removed via the squeeze function in PLATON. The crystal data and structure refinement parameters are included in Table 2.4 where X is determined to be Cl.

The heavy atoms X were determined to be Cl^- rather than $S(H)^-$ for both clusters by comparing average bond lengths of previously reported iron-sulfur clusters (see Table 2.5). The average Fe-X bond length for the [4Fe-4S] cluster of the black rod crystals is 2.214 Å which matches best with the average Fe-Cl bond length for the tetrachloro cluster $[Fe_4S_4Cl_4]^{2-}$ (difference of 0.006 Å) rather than the average Fe-S bond length of either $[Fe_4S_4(SH)_4]^{2-}$ or $[Fe_4S_4(SPH)_4]^{2-}$ (difference of 0.054 Å). Although no structure has been reported for the $[Fe_2S_2(SH)_4]^{2-}$ cluster, because the Fe-S(H) and Fe-S(Ph) bond lengths are essentially identical for the [4Fe-4S] cubane clusters, these bond lengths are inferred to be the same for the [2Fe-2S] dimer clusters. Thus, the average Fe-X bond length of the [2Fe-2S] cluster in the red plate crystals is 2.249 Å and again matches best with the average Fe-Cl bond length of $[Fe_2S_2Cl_4]^{2-}$ (difference of 0.001 Å) rather than the average Fe-S bond length of $[Fe_2S_2(SPh)_4]^{2-}$ (difference of 0.052 Å).

Table 2.4. Crystal data and structure refinement for $[(Fe(To\text{-}F_2PP))_2O]$ • $(Bu_4N)[Fe_4S_4Cl_4]$ and $(Bu_4N)_2[Fe_4S_4Cl_4]$ with PLATON squeeze applied.

Compound	**$[(Fe(To\text{-}F_2PP))_2O]$ • $[Fe_4S_4Cl_4]^{2-}$ • 1,2-dce* CDCC 961981**	**$(Bu_4N)[Fe_4S_4Cl_4]^{-}$* CDCC 961990**
Empirical formula	$C_{90}\ H_{44}\ Cl_6\ F_{16}\ Fe_4\ N_8\ O\ S_2$	$C_{16}\ H_{36}\ Cl_4\ Fe_4\ N\ S_4$
Appearance	red wine plate	black rod
Formula weight	2057.55	735.9
Temperature	100(2) K	100(2) K
Wavelength	1.54178 Å	0.71073 Å
Crystal system	Orthorhombic	Monoclinic
Space group	Pna2(1)	P2/n
Unit cell dimensions	a = 33.9255(16) Å α= 90°	a = 11.4449(7) Å α= 90°
	b = 23.1335(9) Å β= 90°	b = 11.6827(7) Å β= 98.505(3)°
	c = 17.1901(7) Å γ = 90°	c = 18.6182(10) Å γ = 90°
Volume	13491.1(10) $Å^3$	2462.0(2) $Å^3$
Z	4	2
Density (calculated)	1.013 mg/m^3	0.993 mg/m^3
Absorption coefficient	5.253 mm^{-1}	1.546 mm^{-1}
F(000)	4120	750
Crystal size	0.40 x 0.14 x 0.11 mm^3	0.33 x 0.16 x 0.06 mm^3
Theta range for data collection	2.31° to 64.76°	1.74° to 25.11°
Index ranges	$-38 \le h \le 39$, $-27 \le k \le 26$, $-12 \le l \le 19$	$-13 \le h \le 13$, $-13 \le k \le 11$, $-22 \le l \le 22$
Reflections collected	48976	20405
Independent reflections	16526 [R(int) = 0.0712]	4379 [R(int) = 0.0460]
Completeness to theta	94.5%	99.6%
Absorption correction	SADABS	SADABS
Max. and min. transmission	0.6008 and 0.2290	0.9103 and 0.6311
Refinement method	Full-matrix least-squares on F^2	Full-matrix least-squares on F^2
Data / restraints / parameters	16526 / 25 / 1006	4379 / 60 / 186
Goodness-of-fit on F2	1.76	1.025
Final R indices [I>2sigma(I)]	R1 = 0.0923, wR2 = 0.1594	R1 = 0.0581, wR2 = 0.1963
R indices (all data)	R1 = 0.1317, wR2 = 0.1665	R1 = 0.0686, wR2 = 0.2043
Largest diff. peak and hole	1.005 and -0.659 e.$Å^{-3}$	1.278 and -0.639 e.$Å^{-3}$

*Data collection and structure determination performed by
Chris Ziegler and **James Engle** at the **University of Akron**.

Table 2.5. Exogenous bond lengths [Å] of clusters $[Fe_2S_2X_4]^{2-}$ and $[Fe_4S_4X_4]^{2-}$.

	[2Fe-2S]			[4Fe-4S]		
Bond	bond length [Å]	compound	ref.	bond length [Å]	compound	ref.
Fe-S(H)	--	na	--	2.262	$(Ph_4P)_2$ $[Fe_4S_4(SH)_4]$	[27]
Fe-S(Ph)	2.301	$(Et_4N)_2$ $[Fe_2S_2(SPh)_4]$	[28]	2.263	$(Bu_4N)_2$ $[Fe_4S_4(SPh)_4]$	[29]
Fe-Cl	2.250	$(Et_4N)_2$ $[Fe_2S_2Cl_4]$	[30]	2.208	$(n\text{Pr}_4N)_2$ $[Fe_4S_4Cl_4]$	[31]
Fe-X	2.249	$(Bu_4N)_2$ $[Fe_2S_2Cl_4]$	this work	2.214	$(Bu_4N)_2$ $[Fe_4SCl_4]$	this work

Figures 2.26 and 2.27 show the $[Fe_4S_4Cl_4]^{2-}$ anion and the packing of the unit cell, respectively, of the black rod crystals. The $[Fe_4S_4Cl_4]^{2-}$ anion matches well with previously published structures with varying counter cations.[8, 31] With the highly disordered tetrabutylammonium ion removed from the unit cell packing, the [4Fe-4S] clusters and the remaining tetrabutylammonium counter ions appear to be arranged in alternating layers.

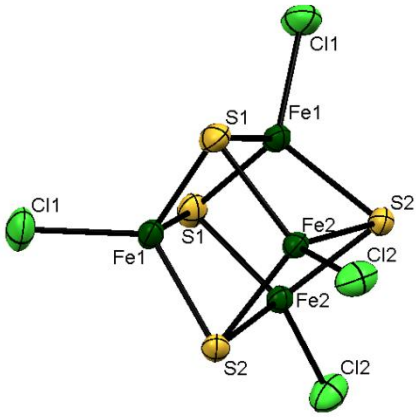

Figure 2.26. ORTEP diagram of $(Bu_4N)_2[Fe_4S_4Cl_4]$ with the $(Bu_4N)^+$ counter ion omitted for clarity. The unit cell packing is shown in Figure 2.27 and the crystal data is included in Table 2.5.

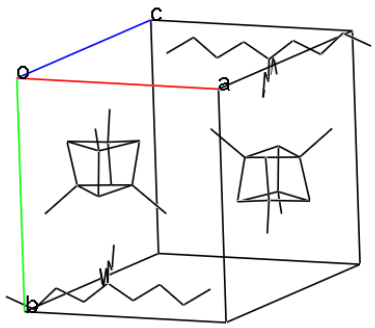

Figure 2.27. Wireframe crystal packing of $(Bu_4N)_2[Fe_4S_4Cl_4]$ (hydrogen atoms and disordered tetrabutylammonium ions are omitted for clarity).

Figures 2.28 and 2.29 show $[(Fe(To\text{-}F_2PP))_2O]$ and the $[Fe_2S_2Cl_4]^{2-}$ anion and the unit cell packing, respectively, for the red plate crystals. The μ-oxo ferric heme structure is analogous to previously reported structures of $[(Fe(TPP^*))_2O]$ where TPP^{*2-} corresponds to different TPP^{2-} derivatives.[32] The structure of the $[Fe_2S_2Cl_4]^{2-}$ cluster is not at all unusual for [2Fe-2S] clusters reported in the literature.[8, 30] Yet, the co-crystallization of these two complexes is unexpected. Both the $[(Fe(To\text{-}F_2PP))_2O]$ and $(Bu_4N)_2[Fe_4S_4Cl_4]$ components are independently neutral. Closer inspection of the interaction of the cluster ion with the heme dimer reveals that the [2Fe-2S] clusters are oriented so that the chloride ligands are directed toward the phenyl rings of the porphyrin ligands. The distance between the chlorides of the cluster and the nearest protons (*para*-hydrogen of the phenyl rings) is between ~3.0 and 3.8 Å; thus, the co-crystallization of these two neutral species is likely due to the electrostatic interaction of the negatively charged chloride ligands of the cluster and the aromatic protons of the porphyrin ligand.

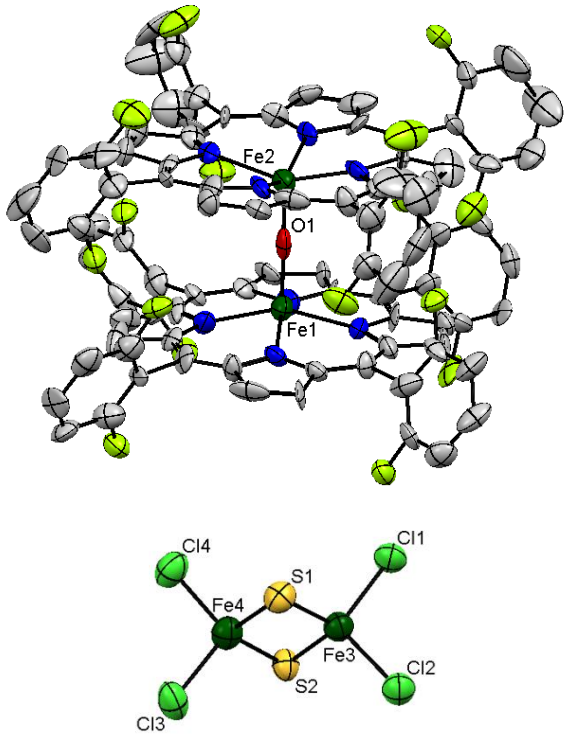

Figure 2.28. ORTEP diagram of $[(Fe(To\text{-}F_2PP))_2O]$ (top) and $(Bu_4N)_2[Fe_2S_2Cl_4]$ (bottom) with the hydrogen atoms and $(Bu_4N)^+$ counter ions omitted for clarity. The unit cell packing is shown in Figure 2.29 and the crystal data is included in Table 2.5.

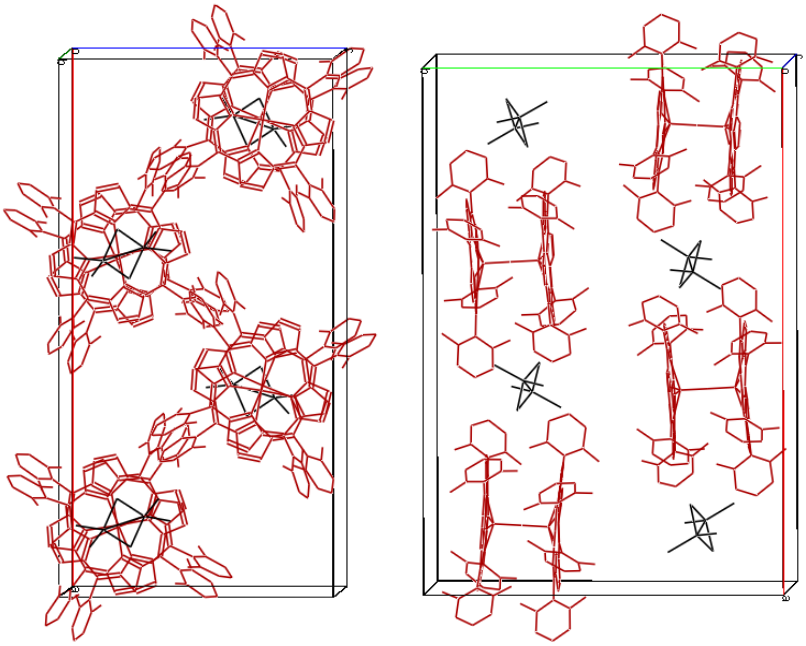

Figure 2.29. Wireframe crystal packing of $[(Fe(To\text{-}F_2PP))_2O] \bullet (Bu_4N)_2[Fe_2S_2Cl_4] \bullet 2$(1,2-dce) (hydrogen atoms, solvent, and disordered tetrabutylammonium cations are omitted for clarity).

Identification of the ferric heme [(Fe(T*o*-F_2PP))$_2$O] in the structure confirms the presence of at least trace quantities of oxygen in the reaction mixture. Both clusters $(Bu_4N)_2[Fe_2S_2Cl_4]$ and $(Bu_4N)_2[Fe_4S_4Cl_4]$ have unexpected chloride exogenous ligands which were initially modeled as -SH groups due to the absence of chloride ions in the starting reaction mixture. The only chlorine source present is the solvent 1,2-dce. However, it has been indicated previously that iron-sulfur clusters in chlorinated solvents will exchange ligands over time to extract chloride, likely through a solvent/cluster decomposition pathway liberating chloride ions to form the very stable all chloro-iron-sulfur clusters by replacing labile thiolate ligands.[8, 31, 33] Although this exchange has been noted several times in literature the mechanism for the extraction of chloride from 1,2-dce is not understood. For the crystallization reactions performed here, it is likely that the redox-active clusters reduce the ferric heme present in solution. In addition, the oxidation of clusters from trace dioxygen is promoting their decomposition, and following reaction with solvent could then cause the liberation of chloride and the formation of the smaller unit iron-sulfur clusters with exogenous chloride ligands.

2.5 Conclusions.

In this chapter, the preparation of the components for a linked catalytic array consisting of a metalloporphyrin and a functionalized site-differentiated [4Fe-4S] cluster, utilizing bridging ligands to connect these units, is reported. These bi-functional bridges contain a thiolate for preferential binding to the [4Fe-4S] cluster and an N-donor ligand for binding to the axial position of the heme. Two new, site-differentiated [4Fe-4S] cluster with bound pyridine and imidazole linkers are reported. Screening of the binding affinities of these pyridine- and imidazole-functionalized clusters to different zinc

porphyrins indicates that imidazoles provide a stronger σ bond, resulting in distinctively higher binding constants. Adding electron-withdrawing substituents at the meso-phenyls of tetraphenylporphyrin (TPP^{2-}) further increases the binding constant of the base. Excitingly, these results demonstrate the formation of the linked [4Fe-4S]-heme catalytic array in solution with high specificity. Due to the high solubility of [M(T*per*-F_5PP)], [M(T*o*-F_2PP)] is the most suitable metalloporphyrin in combination with $(Bu_4N)_2[Fe_4S_4(TriS)(SEtIm)]$ for future spectroscopic and reactivity studies of the linked system. Binding between the chosen complexes was further confirmed by cyclovoltammetry. A significant influence of the solvent environment on the reduction potential of the [4Fe-4S] cluster was observed, and correspondingly, binding of $(Bu_4N)_2[Fe_4S_4(TriS)(SEtIm)]$ to a zinc porphyrin causes a distinct shift in the reduction potential of the cluster by the increase in polarity of the cluster environment in the presence of the metalloporphyrin. These results again confirm the formation of heme-cluster arrays in solution with our bridging ligands. At this point in time a crystal structure has not been obtained for the bound complex. Importantly, our new complex design allows for individual component modifications to optimize binding between the electron reservoir and the catalytic heme component.

Continuation of this research has been directed toward isolating a complex with a redox active heme instead of zinc, thus creating a catalytic site next to the iron-sulfur cluster. Attempts thus far for isolating a heme axially coordinated by the bridging ligand of the iron-sulfur cluster have been limited by the difference in solubility of the heme and iron-sulfur cluster in non-coordinating solvents since coordinating solvents can interfere with the binding of the bridging ligand to the heme. In addition, ferrous heme is highly

sensitive to oxidation by stray dioxygen forming the ferric heme which requires an anion to stabilize the charge at the cost of the stability of the iron-sulfur cluster. As the iron-sulfur clusters fall apart with decomposition of chlorinated solvents, chloride ions are generated, resulting in the generation of the all chloro [2Fe-2S] and [4Fe-4S] clusters as described above. Therefore, ferric heme cannot be used for the initial [4Fe-4S]-heme adduct formation, as they efficiently decompose the iron-sulfur cluster.

The axially bound design allows for the separate development of each individual component thus producing metalloporphyrins bound by an axial coordinating bridging ligand to a site-differentiated cluster. Further modifications to the heme or cluster to increase solubility and to decrease oxygen sensitivity of the heme by shifting the redox potential to a more positive potential are future avenues to explore for later generations of the axially coordinated model complex design.

2.6 References

[1] B. R. Crane, E. D. Getzoff, *Curr. Opin. Struct. Biol.* **1996**, *6*, 744.

[2] M. J. Murphy, L. M. Siegel, S. R. Tove, H. Kamin, *Proc. Natl. Acad. Sci. U. S. A.* **1974**, *71*, 612-616.

[3] E. M. Cameron, *Nature* **1982**, *1982*, 145-148.

[4] L. Kang, J. LeGall, A. T. Kowal, M. K. Johnson, *J. Inorg. Biochem.* **1987**, *30*, 273-290.

[5] a) K. Parey, E. Warkentin, P. M. H. Kroneck, U. Ermler, *Biochemistry* **2010**, *49*, 8912-8921; b) K. W. Smith, M. E. Stroupe, *Biochemistry* **2012**, *51*, 9857-9868.

[6] M. E. Stroupe, E. D. Getzoff, in *Handb. Metalloproteins* (Eds.: A. Messerschmidt, R. Huber, T. Poulos, K. Wieghardt), John Wiley & Sons, Ltd., Chichester, **2001**, pp. 471-485.

[7] L. Cai, R. H. Holm, *J. Am. Chem. Soc.* **1994**, *116*, 7177-7188.

[8] P. V. Rao, R. H. Holm, *Chem. Rev.* **2004**, *104*, 527-559.

[9] C. Zhou, L. Cai, R. H. Holm, *Inorg. Chem.* **1996**, *35*, 2767-2772.

[10] a) C. Walsdorff, W. Saak, S. Pohl, *J. Chem. Soc., Dalton Trans.* **1997**, 1857-1861; b) E. P. L. van der Geer, G. van Koten, R. J. M. Klein Gebbink, B. Hessen, *Inorg. Chem.* **2008**, *47*, 2849-2857; c) A. Vacca, C. Nativi, M. Cacciarini, R. Pergoli, S. Roelens, *J. Am. Chem. Soc.* **2004**, *126*, 16456-16465.

[11] C. A. M. Afonso, N. M. T. Lourenço, A. de A. Rosatella, *Molecules* **2006**, *11*, 81-102.

[12] a) A. D. Adler, F. R. Longo, J. D. Finarelli, J. Goldmacher, J. Assour, L. Korsakoff, *J. Org. Chem.* **1967**, *32*, 476-476; b) T. P. Wijesekera, D. A. Dolphin, in *In Metalloporphyrins in Catalytic Oxidations* (Eds.: R. A. Sheldon, Ed., M. Dekker), New York, NY, **1994**, pp. 193-239.

[13] J. S. Lindsay, R. W. Wagner, *J. Org. Chem.* **1989**, *54*, 828-836.

[14] H. Quast, T. Dietz, A. Witzel, *Liebigs Ann.* **1995**, 1495-1501.

[15] R. A. Ghiladi, R. M. Kretzer, I. Guzei, A. L. Rheingold, Y.-M. Neuhold, K. R. Hatwell, A. D. Zuberbu, K. D. Karlin, *Inorg. Chem.* **2001**, *40*, 5754-5767.

[16] B. A. Averill, T. Herskovitz, R. H. Holm, J. A. Ibers, *J. Am. Chem. Soc.* **1973**, *95*, 3523-3534.

[17] C. Hansch, A. Leo, R. W. Taft, *Chem. Rev.* **1991**, *91*, 165-195.

[18] B. V. DePamphilis, B. A. Averill, T. Herskovitz, J. L. Que, R.H.Holm, *J. Am. Chem. Soc.* **1974**, *96*, 4159-4167.

[19] C. Zhou, J. W. Raebiger, B. M. Segal, R. H. Holm, *Inorg. Chim. Acta* **2000**, *300-302*, 892-902.

[20] N. J. Rose, R. S. Drago, *J. Am. Chem. Soc.* **1959**, *81*, 6138-6141.

[21] a) F. A. Walker, U. Simonis, in *Encycl. Inorg. Chem.*, John Wiley & Sons, Ltd., **2006**, pp. 1-132; b) G. C. Vogel, B. A. Beckmann, *Inorg. Chem.* **1976**, *15*, 483-484; c) V. K. K. Praneeth, C. Näther, G. Peters, N. Lehnert, *Inorg. Chem.* **2006**, *45*, 2795-2811.

[22] C. H. Kirksey, P. Hambright, C. B. Storm, *Inorg. Chem.* **1969**, *8*, 2141-2144.

[23] a) H. C. Brown, D. H. McDaniel, O. Ha¨fliger, in *Determination of Organic Structures by Physical Methods* (Eds.: E. A. Braude, F. C. Nachod), Academic Press, New York, **1955**; b) T. C. Bruice, G. L. Schmir, *J. Am. Chem. Soc.* **1958**, *80*, 148-156.

[24] S. G. DiMagno, V. S. Y. Lin, M. J. Therien, *J. Org. Chem.* **1993**, *58*, 5983-5993.

[25] a) P. A. Janick, L. M. Siegel, *Biochemistry* **1982**, *21*, 3538-3547; b) J. A. Christner, E. Münck, P. A. Janick, L. M. Siegel, *J. Biol. Chem.* **1983**, *258*, 11147-11156.

[26] H. Beinert, R. H. Holm, E. Münck, *Science* **1997**, *277*, 653659.

[27] A. Müller, N. H. Schladerbeck, H. Bögge, *J. Chem. Soc., Chem. Commun.*, **1987**, 35-36.

[28] L. E. Maelia, S. A. Koch, *Inorg. Chem.* **1986**, *25*, 1896-1904.

[29] L. Guodong, Z. Hongtu, H. Sheng-Zhi, T. C. W. Mak, *Acta Cryst.* **1987**, *C43*, 352-353.

[30] M. A. Bobrik, K. O. Hodgson, R. H. Holm, *Inorg. Chem.* **1977**, *16*, 1851-1858.

[31] B.M.Segal, H.R.Hoveyda, R.H.Holm, *Inorg. Chem.* **1998**, *37*, 3440-3443.

[32] a) K. D. Karlin, A. Nanthakumar, S. Fox, N. N. Murthy, N. Ravi, B. H. Huynh, R. D. Orosz, E. P. Day, *J. Am. Chem. Soc.* **1994**, *116*, 4753-4763; b) A. Gold, K. Jayaraj, P. Doppelt, J. Fischer, R. Weiss, *Inorg. Chim. Acta* **1988**, *150*, 177-181.

[33] F. Osterloh, W. Saak, S. Pohl, *J. Am. Chem. Soc.* **1997**, *119*, 5648-5656.

CHAPTER 3

Assimilatory Sulfite Reductase Inspired Complexes for Catalysis

Covalently Bound Model

3.1 Introduction

In an effort to synthesize biologically inspired catalysts for multi-electron reductions utilizing the basic components of the active site of aSIR, the importance of the bridging ligand has been evident from the work presented in Chapter 2. The biological sulfide or cysteinate bridge between the siroheme catalytic site and the [4Fe-4S] electron reservoir is maintained by structural stabilization from the protein which locks the iron-sulfur cluster in place and orients the siroheme for axial ligation to the cluster. The resulting distance between the Fe of the siroheme and the closest Fe center of the iron-sulfur cluster, bound to the bridge, is 4.48 Å (aSIR of *E. coli*) .[1] The non-linear $Fe_{siroheme}$-S(cys)-$Fe_{[4Fe-4S]}$ bond angle of 126° results in the iron-sulfur cluster being quite close to the siroheme. The S(cys)-$Fe_{[4Fe-4S]}$ bond which lies below the plane of the siroheme bisects the N-$Fe_{siroheme}$-N angle (see Figure 3.1). As a result, one inorganic sulfide of the iron-sulfur cluster is within just 3.63 Å of a *meso*-carbon of the siroheme as illustrated in Figure 3.1.[2] This distance is within van der Waals contact between a carbon (1.7 Å radius) and sulfur (1.8 Å radius).[3] The protein restricts the siroheme and iron-sulfur cluster to maintain this interaction which could be an alternative route by which electrons could transfer from the electron reservoir iron-sulfur cluster to the catalytic site siroheme iron center.

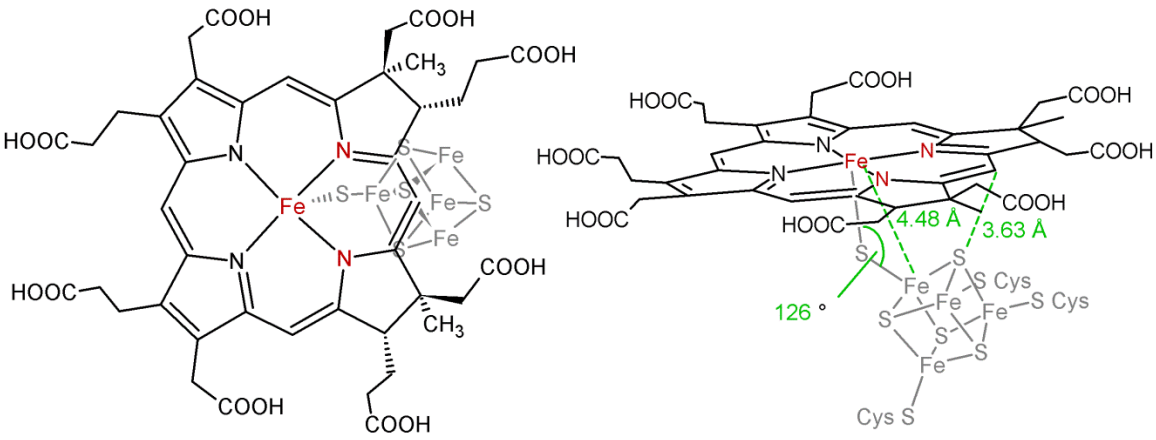

Figure 3.1. An illustration of the dimensions and orientation of the siroheme and the [4Fe-4S] cofactor of aSIR of *E coli*.

In order to circumvent the difficulties faced in bridging a heme system to an iron-sulfur cluster via axial binding, in particular the assurance that the components remain bound in solution through redox activity (see Chapter 2), an alternative biologically inspired design utilizing a covalent attachment of the two components was devised. The evidence for the potential transfer of electrons from the iron-sulfur cluster to the Fe of the siroheme via the S···C contact of the isobacteriochlorin supports prospective designs linking an iron-sulfur cluster to the porphyrin ligand of the heme. Our covalently linked biologically inspired SIR catalyst design utilizes this idea while maintaining the basic components of the active site of aSIR, a catalytic site heme, a bridge, and an electron reservoir [4Fe-4S] cluster. The site-differentiated [4Fe-4S] cluster, which was introduced as a precursor in Chapter 2, is again used for the covalent design as the electron reservoir component in order to prohibit oligomer formation. A porphyrin which has been modified to include a hydroxyl functional group is used as the catalytic site and the bridge. As seen in Figure 3.2, three positions have been highlighted in which a functional group could be introduced for ligation to a [4Fe-4S] cluster. Position X1 (at the β pyrrole)

for the functional group provides for the most biologically relevant connection and, as well as position X2 (at the *meso*-carbon), should provide for the most efficient electron transfer to the heme iron directly via the conjugated porphyrin core. However, functionalizing a porphyrin at either position X1 or X2 is synthetically challenging. Alternatively, inclusion of a functional group at position X3 (at the *para* position of the phenyl substituent) of the tetraphenylporphyrin ligand is relatively trivial in comparison and is the position targeted for our first generation model design.

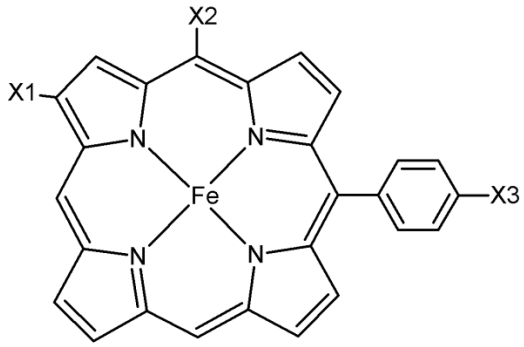

Figure 3.2. Scheme of the positions on the porphyrin ligand that could be utilized for inclusion of a functional group for ligation to a [4Fe-4S] cluster.

Thus, the functionalized porphyrin is formally a large ligand for the unique iron center of the site-differentiated [4Fe-4S] cubane, forming a covalent bond to link the two components (Figure 3.3). Supporting the expected stability of the covalent bond to be formed by the functional group at position X3 of the porphyrin is the fact that iron-sulfur clusters form stable bonds with phenylthiolate and phenolate ligands.[4] A considerable flexibility for fine tuning the properties of the heme is accessible in this design by inclusion of electron-withdrawing or donating groups at the easily modifiable phenyl groups of TPP. In addition, a neutral ligand for axial coordination to the heme iron can also be included.

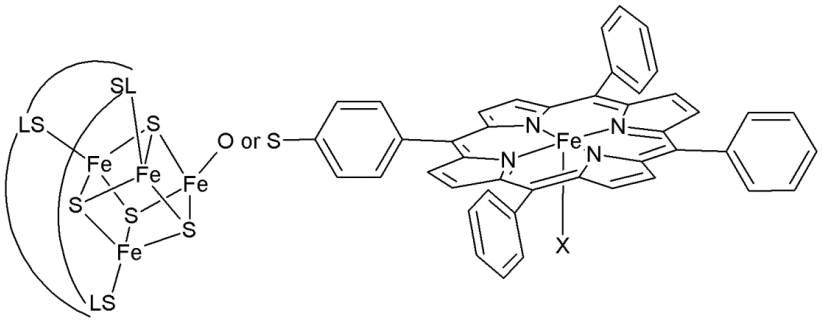

Figure 3.3. Scheme of the biologically-inspired covalently bound design applied here.

One previous attempt at a similar design was reported by Bradshaw and coworkers in which four equivalents of thiol-functionalized TPP (*p*-H_2TPP(SH)) as the free base was reacted with one equivalent of the ethylthiolate cluster $[Fe_4S_4(SEt)_4]^{2-}$, and the reaction was monitored by ^{1}H-NMR.[5] The complete loss of the characteristic ~13 ppm proton signal for the ethylthiolate ligand bound to the cubane cluster was observed with the addition of the thiol porphyrin as the volatile ethanethiol generated in the reaction evaporates. The phenylthiolate of the porphyrin therefore ligates to the cluster, presumably generating an iron-sulfur cubane cluster tetra-ligated by the thiolate-functionalized porphyrin, $[Fe_4S_4(p\text{-}H_2TPP(S))_4]^{2-}$ (Figure 3.4).

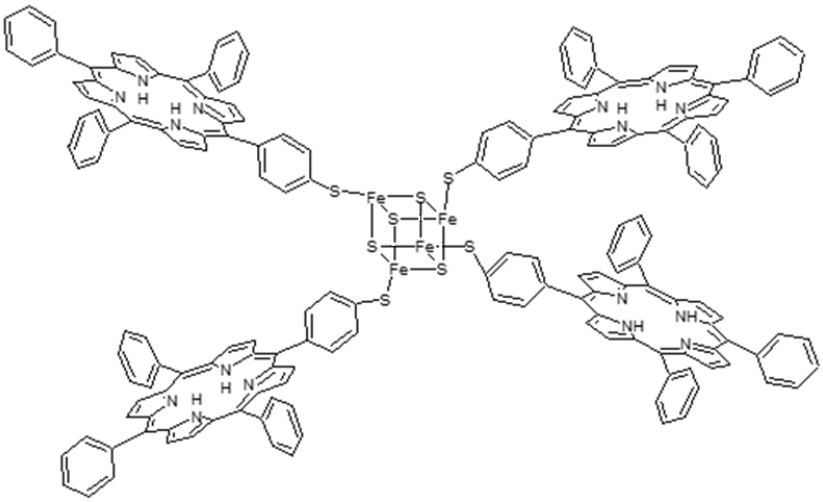

Figure 3.4. Representation of the heme-[4Fe-4S] array reported by Bradshaw and coworkers.[5]

The obvious disadvantage of the synthetic analogue of SIR prepared by Bradshaw and coworkers is the ratio of catalytic sites (porphyrins/hemes) to electron reservoirs ([4Fe-4S] clusters). However, if one would prepare a system where the ratio is reverse, i.e. one catalytic site to four electron reservoirs, then this complex could hold five electrons for reducing substrate. This is an alluring prospect and would provide a system with superior catalytic properties. Therefore, the tetra functionalized porphyrin was the first to be used for our covalently bound design. Unfortunately, deprotection of the -SMe thioether groups of tetra(para-methylthiolate)phenyl porphyrin, H_2(T*p*-(SMe)PP), was not possible due to the extreme insolubility of this tetra-substituted porphyrin. Thus, the following efforts toward obtaining the covalently bound biologically inspired catalyst design entail the use of one porphyrin with one functional group for ligation to one iron-sulfur cluster, as shown in Figure 3.3. This model is presented in this chapter.

3.2 Methods and Experimental Procedures

General Procedures. All cluster and ferrous heme synthetises were performed under a nitrogen atmosphere in a glove box or by utilizing common Schlenk line techniques. ^{1}H- and ^{19}F-NMR spectra were acquired on a Varian MR400 400 MHz spectrometer and referenced to solvent. Mid-IR spectra were collected on a Perkin Elmer Spectrum BX FT-IR spectrometer in KBr pellets. Mass spectrometric data were collected on a Micromass LCT Time-of Flight mass spectrometer. Elemental analyses were performed by Atlantic Mircolab, Inc., Norcross, GA. Electronic spectra were measured on a Varian CARY 1E UV-Visible spectrometer. Cyclic voltammetry experiments were conducted in 0.1 M solutions of Bu_4NPF_6 in acetonitrile (MeCN) or in 1,2-dichloroethane

(1,2-dce) with a glassy carbon working electrode, a Pt counter electrode and a Ag/AgCl reference electrode on a EG&G Princeton Potentiostat/Galvanostat model 263A. The redox potentials are calibrated to Fc/Fc^+ and reported vs. NHE.

Materials. All solvents were purified by distillation and degassed as needed. Pyrrole was distilled under an inert atmosphere and used immediately. All reagents were used as purchased and degassed under vacuum as needed. $(Bu_4N)_2[Fe_4S_4(SEt)_4]$[6] was prepared according to published procedures. The synthesis of $(Bu_4N)_2[Fe_4S_4(TriS)(SEt)]$ from $(Bu_4N)_2[Fe_4S_4(SEt)_4]$ and a solution of $TriSH_3$ is described in Chapter 2.2, Methods and Experimental.[7]

Synthesis of 5-(*p*-hydroxyphenyl)-10,15,20-triphenylporphyrin [H_2(*p*-TPP(OH))]. The previously reported synthesis of H_2(*p*-TPP(OMe)) was slightly modified.[8] Benzaldehyde (17 mL, 0.165 mol) and anisaldehyde (2 mL, 0.0165 mol) were added with stirring to refluxing propionic acid (1 L) in a 2 L two neck round bottom flask equipped with a condenser and an addition funnel. Freshly distilled pyrrole (15 mL, 0.21 mol) dissolved in 50 mL propionic acid was loaded in the addition funnel and subsequently added dropwise to the refluxing aldehyde solution. The resulting purple, black solution was refluxed an addition 3 hours with stirring. The solution was heated with a high vacuum applied to remove the propionic acid. The remaining black tar was dissolved into 200 mL of chloroform to which a saturated solution of $NaHCO_{3(aq)}$ was added. The resulting solution was vigorously stirred until the generation of gas ceased to remove residual propionic acid. The organic phase was washed twice with dilute $Na_2CO_{3(aq)}$ and brine (x3) until the pH of the solution was maintained at 7. The organic phase was taken to dryness and the residue was dissolved in 200 mL of CH_2Cl_2. With

stirring, ~10 g of silica powder was added to extract large chain polymers from the solution. The suspension was then filtered through medium grade filter paper with suction. The remaining black silica gel was washed with CH_2Cl_2 while checking the wash for porphyrin by TLC. The filtrate was concentrated and loaded onto a silica column with 100% CH_2Cl_2 eluent. The first fluorescent, colored band collected was identified as H_2TPP by LCT-MS. The second fluorescent, colored band was collected by changing the eluent to 1:3 EtOAc to CH_2Cl_2. The fraction collected this way was dried over $MgSO_4$, filtered, and taken to dryness to yield 2.68 g of a purple solid (25.3% yield) of the desired product H_2(*p*-TPP(OMe)). ^{1}H-NMR (400 MHz, $CDCl_3$, rt, ppm): 8.86 and 8.82 (2 d, 8H, *β*-H pyrrole), 8.20 (m, 6H), 8.11 (d, 2H) 7.78-7.71 (m, 9H), 7.28 (d, 2H), 4.08 (s, 3H, OMe), -2.77 (s, 2H). (ESI+) *m/z* 645.2 $[H_3(p\text{-TPP(OMe)}]^+$, 323.1 $[H_4(p\text{-TPP(OMe)}]^{2+}$. UV-vis ($CH_2Cl_2$, λ nm): 417, 514, 549, 589, 645.

The formation of the hydroxyl group from the methyl ether was accomplished via a slightly modified procedure from a previously reported synthesis.[9] H_2(*p*-TPP(OMe)) (1.0 g, 1.55 mmol) was loaded in a 500 mL Schlenk flask with a stir bar. The flask was sealed with a rubber septum and evacuated. Distilled and degassed CH_2Cl_2 (~200 mL) was added via cannula and the flask was repressurized with N_2 gas. BBr_3 (2.9 mL, 31.0 mmol) was added via syringe to the red solution which turned green with the addition. This solution was left to stir overnight under a flow of nitrogen gas. The green solution was slowly poured over 200 mL of ice and water. A saturated $Na_2CO_{3(aq)}$ solution (~25 mL) was added to the stirring solution until the pH of the mixture maintained was maintained between 7-8. The mixture was stirred an additional half hour resulting in a red solution. The mixture was transferred to a separatory funnel and 100 mL of EtOAc was

added. The combined organic phase was washed with DI water (x3), brine (x2), dried over MgSO4, filtered, and taken to dryness to yield 0.94 g (96% yield) of a purple solid, identified as the desired product. ^{1}H-NMR (400 MHz, $CDCl_3$, rt, ppm): 8.85 and 8.82 (2 d, 8H, *β*-H pyrrole), 8.20 (m, 6H), 8.06 (d, 2H) 7.76-7.71 (m, 9H), 7.17 (d, 2H), -2.79 (s, 2H). (ESI+) *m/z* 631.2 $[H_3(p\text{-TPP(OH)}]^+$. UV-vis (CH_2Cl_2, λ nm): 418, 515, 550, 591, 647.

Synthesis of 5-(*p*-hydroxyphenyl)-10,15,20-tri-(pentafluorophenyl)porphyrin [H_2(TPPF_{15}(OH))]. H_2(TPPF_{15}(OMe)) was prepared by a modification to a previously reported porphyrin synthesis.[10] Pentafluorobenzaldehyde (4.404 g, 22.5 mmol), anisaldehyde (0.91 mL, 7.5 mmol), and freshly distilled pyrrole (2.1 mL, 30.3 mmol) were dissolved in 250 mL dry CH_2Cl_2 and 1.25 mL EtOH in a 500 mL round bottom (RB) flask under N_2 gas and stirred for 15 minutes. To the stirring solution, BF_3•Et_2O (1.25 mL, 6.7 mmol) was added via syringe. The reaction flask was covered with foil to minimize exposure to light. After stirring for 4 h under a gentle flow of N_2, Et_3N (5 mL, 26 mmol) was added via syringe, and 5 minutes later 2,3-dichloro-5,6-dicyanobenzoquinone (DDQ) (10.0 g, 44.1 mmol) was added to the solution. The reaction mixture was stirred overnight in minimal light. The mixture was taken to dryness, dissolved in a minimum of 1:1 CH_2Cl_2/hexane mix and loaded on a silica column with the same solvent ratio for the eluent. The first two bands of colored product collected were identified as the fluorinated porphyrin H_2(T*per*-F_5PP) and the fluorinated hexaphyrin. The third colored band to elute was identified as the desired product. The solution was taken to dryness, and recrystallized from CH_2Cl_2 layered with hexane. Purple, rod crystals were collected by filtration for a yield of 0.980 g (14.3% yield). ^{1}H-

NMR (400 MHz, $CDCl_3$, rt, ppm): 8.99 (d, 2H), 8.86 (dd, 4H), 8.79 (d, 2H), 8.12 (d, 2H), 7.32 (d, 2H), 4.10 (s, 3H, OMe), -2.85 (s, 2H). ^{19}F-NMR (400 MHz, $CDCl_3$, rt, ppm): -136.65 (m, 6F), -151.82 (m, 3F), -161.66 (m, 6F). (ESI+) *m/z* 914.6 $H_3[TPPF_{15}(OMe)]^+$. UV-vis (CH_2Cl_2, λ nm): 416, 511, 585.

The demethylation of $H_2(TPPF_{15}(OMe))$ to $H_2(TPPF_{15}(OH))$ was performed analogously to the synthesis described above, with the addition of a silica column with 1:1 CH_2Cl_2/ hexane eluent for purification. The first compound to elute was the starting material porphyrin and the second porphyrin to elute was the desire product for a percent yield of 76%. (ESI+) *m/z* 900.7 $H_3[TPPF_{15}(OH)]^+$.

The **synthesis of [Zn(TPPF$_{15}$(OH))] and [Zn(*p*TPP(OH))]** was performed as previously reported, and is typical for the zinc metallation of a porphyrin with $Zn(OAc)_2$.[11] The **synthesis of [Fe^{II}(*p*TPP(OH))]** was performed as previously reported, and is typical for the metallation of a free-base porphyrin with $FeCl_2$, followed by formation of the ferric μ-oxo dimer, and finally reduction with EtSH.[12]

Synthesis of $(Bu_4N)_2[Fe_4S_4(TriS)(OPh)]$. $(Bu_4N)_2[Fe_4S_4(TriS)(SEt)]$ (0.3 g, 0.195 mmol) was dissolved in 15 mL of MeCN and solid phenol (0.03 g, 0.333mmol) was added while stirring in a glove box. The reaction vessel was sealed and a vacuum was applied. The reaction was allowed to stir for 1 hour under static vacuum. The reaction mixture was filtered, and the filtrate was layered with 100 mL of Et_2O. The black precipitate was collected by vacuum filtration, washed with ether, and dried under vacuum. The yield was not measured. ^{1}H NMR (400 MHz, CD_3CN, rt, ppm): δ TriS: 7.89 (broad s), 7.73 (d), 7.32 (t), 6.98 (s), 6.59 (s), 2.41 (broad s), 1.18 (s); δ OPh: 8.91 (s),

7.76 (s), 6.82 (s); δ $\underline{Bu_4N^+}$: 3.05, 1.59, 1.34, 0.96. CV (MeCN, 0.01 M): -750 mV (irr.) $[Fe_4S_4]^{2+/1+}$.

Synthesis of $(Bu_4N)_2[Fe_4S_4(TriS)(OPhF)]$. The same reaction conditions were used as for $(Bu_4N)_2[Fe_4S_4(TriS)(OPh)]$, with the difference that *p*-fluorophenol was used instead of phenol. ^{1}H NMR (400 MHz, CD_3CN, rt, ppm): δ TriS: 7.88 (broad s), 7.76 (d), 7.32 (t), 6.98 (s), 6.57 (s), 2.42 (broad s), 1.18 (s); δ OPhF: 8.60 (d), 6.51 (broad); δ $\underline{Bu_4N^+}$: 3.04, 1.59, 1.34, 0.96. ^{19}F NMR (400 MHz, CD_3CN, rt, ppm): -125.86 (s). CV (MeCN, 0.01 M): -769 mV $[Fe_4S_4]^{2+/1+}$ (quasi-rev.).

Structure Determination. Purple plates of [Zn(*p*TPP(OH))] were grown from a CH_2Cl_2 solution of the compound at 23 °C. A crystal of dimensions 0.19 x 0.08 x 0.02 mm was mounted on a Rigaku AFC10K Saturn 944+ CCD-based X-ray diffractometer equipped with a low temperature device and Micromax-007HF Cu-target micro-focus rotating anode (l = 1.54187 A) operated at 1.2 kW power (40 kV, 30 mA). The X-ray intensities were measured at 85(1) K with the detector placed at a distance of 42.00 mm from the crystal. A total of 3770 images were collected with an oscillation width of 1.0° in ω. The exposure time was 5 sec. for the low angle images, 20 sec. for high angle images. The integration of the data yielded a total of 20877 reflections to a maximum 2q value of 136.48° of which 2831 were independent and 2702 were greater than 2s(I). The final cell constants (Table 3.1) were based on the xyz centroids of 15730 reflections above 10s(I). Analysis of the data showed negligible decay during data collection; the data were processed with CrystalClear 2.0 and corrected for absorption. The structure was solved and refined with the Bruker SHELXTL (version 2008/4) software package, using the space group P1bar with Z = 1 for the formula $C_{44}H_{28}N_4OZn$. Full matrix least-

squares refinement based on F2 converged at R1 = 0.0396 and wR2 = 0.1084 [based on I > 2σ (I)], R1 = 0.0406 and wR2 = 0.1095 for all data. The hydroxyphenyl substituent is site disordered over four positions. Additional details are presented in Table 3.1 and via the Cambridge Structural Database (CSD) CCDC 948446.

3.3 Synthesis and Properties of the Molecular Components

The synthesis of singly functionalized porphyrins is necessary for the completion of the covalently bound complex design. As indicated in the Introduction, functionalization of a phenyl group at the *para* position is the least synthetically demanding option of the three possibilities shown in Figure 3.2. A hydroxyl functional group was chosen as the linking group to the iron-sulfur cluster due to the ease of deprotection of a methyl ether group to form the required hydroxyl group. The two most popular syntheses of tetraphenylporphyrins from aldehyde and pyrrole are (i) the Adler method, via refluxing in propionic acid for both the condensation and the oxidation of the formed ring (see Figure 3.5), and (ii) the Lindsey method, via condensation with BF_3•Et_2O and oxidation of the ring with an organic oxidant such as DDQ.[13] By both routes a considerable amount of oligomerization and polymerization occurs rather than ring closure in the condensation step; therefore, column chromatography is usually necessary for purification. Using either of these methods for the synthesis of a singly functionalized porphyrin further diminishes the already low yields of symmetric porphyrins, because the major porphyrin product will still be the completely symmetric porphyrin. Decent yields of 25% and 14% were achieved for the methoxy-functionalized porphyrins prepared here, using the conditions described in the Experimental Section.

The two methoxy-functionalized porphyrins prepared here were demethylated using BBr_3 and protonated using water (see Figure 3.5). The simple TPP derivative featuring one hydroxyl group, 5-(p-hydroxyphenyl)-triphenylporphyrin, is referred to in this work as H_2(*p*-TPP(OH)). Inclusion of fluorine atoms at the three phenyl rings not functionalized in this compound was achieved by incorporating pentafluorobenzaldehyde rather than benzaldehyde in the condensation. The resulting hydroxyl-functionalized porphyrin, 5-(p-hydroxyphenyl)-10,15,20-tri-(pentafluorophenyl)porphyrin, is referred to here as $H_2(TPPF_{15}(OH))$ (see Figure 3.5). This hydroxyl porphyrin was synthesized with added electron withdrawing groups to investigate the effect on the redox potential of the $Fe^{2+/3+}$ couple of the heme component, and how this affects the properties of the resulting heme-[4Fe-4S] catalytic array.

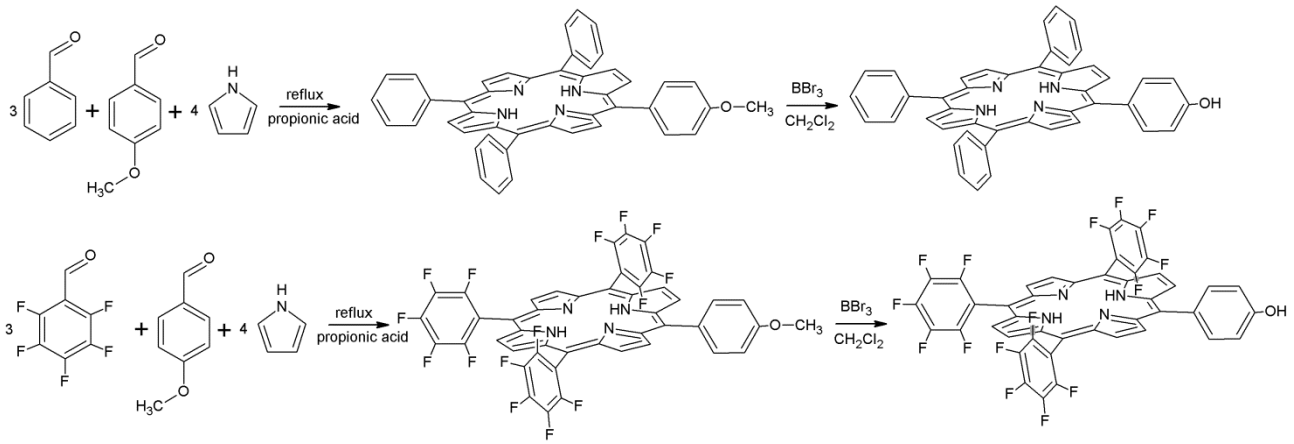

Figure 3.5. Synthetic scheme for H_2(*p*-TPP(OH)) (top) and $H_2(TPPF_{15}(OH))$ (bottom).

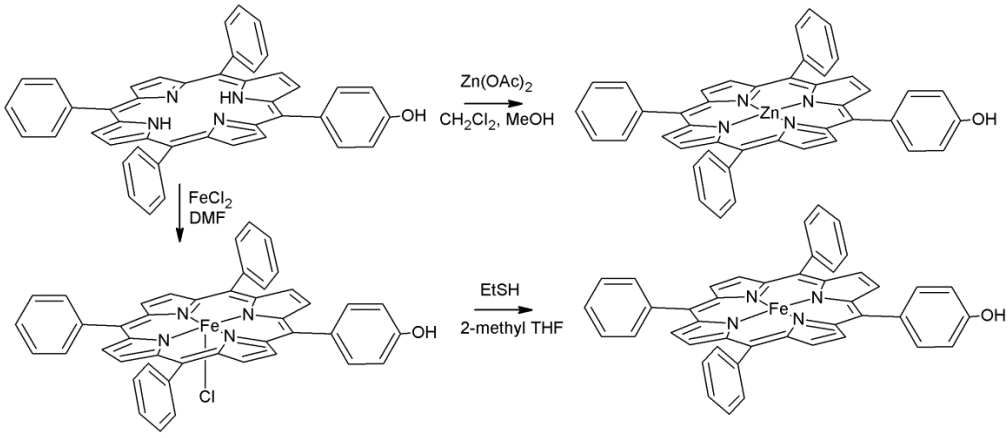

Figure 3.6. Synthetic scheme for the metallation of H_2(*p*-TPP(OH)) with zinc (top) and iron (bottom).

Metallation of these functionalized porphyrins was completed with zinc and iron (Figure 3.6). Purple rod crystals were acquired for [Zn(*p*-TPP(OH))] and a structure was determined for this compound by x-ray crystallography, since a structure for this porphyrin has not been reported previously. The geometric structure of this complex is shown in Figure 3.7 and the crystal packing is shown in Figure 3.8. The hydroxyl group is disordered over all four phenyl substituents of the heme in the crystal structure. It should be noted that the porphyrin ligand in this complex shows minimal ruffling and no saddling.

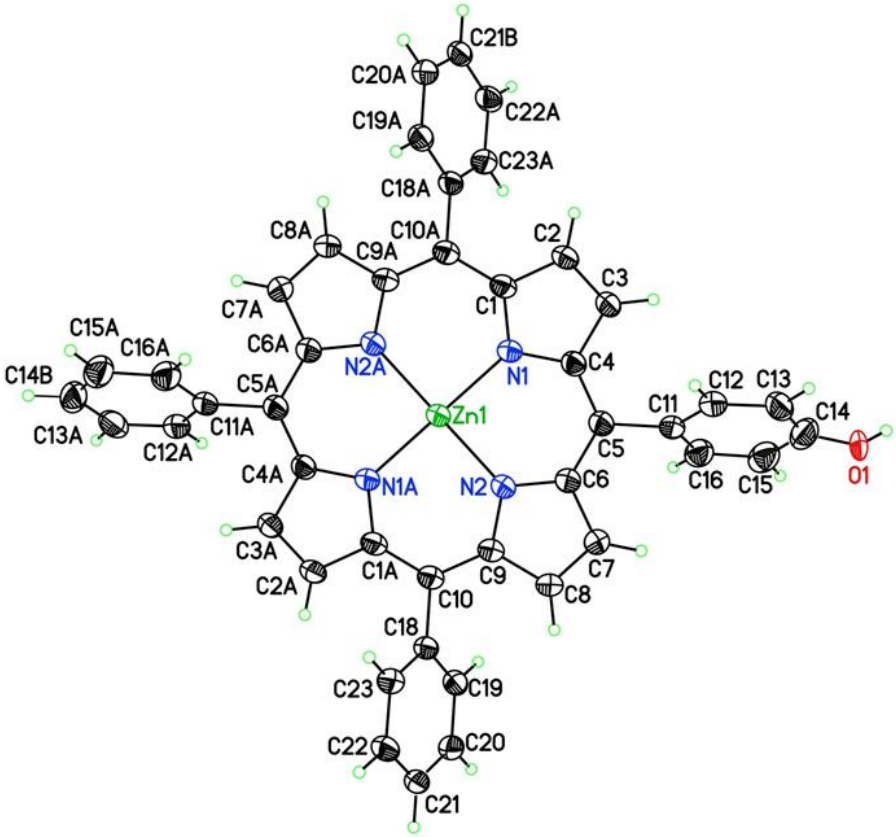

Figure 3.7. ORTEP diagram of [Zn(*p*TPP(OH))], depicting the hydroxyl group at one of the four disordered positions.

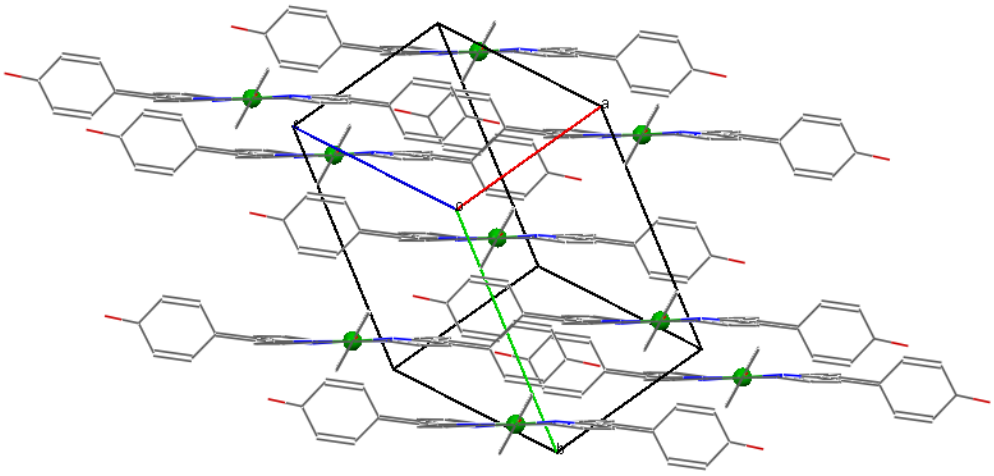

Figure 3.8. Wire frame diagram of the crystal packing of [Zn(*p*TPP(OH))] with the hydrogen atoms removed for clarity, the zinc atom represented as a ball for reference to the porphyrin center, and showing two of the four disordered positions of the hydroxyl group. The unit cell contains one zinc porphyrin molecule. The structural information is included in Table 3.1.

Table 3.1. Crystal data and structure refinement for [Zn(*p*TPP(OH))].

Compound	**[Zn(*p*TPP(OH))]* CCDC 948446**
Empirical formula	$C_{44}\ H_{28}\ N_4\ O\ Zn$
Appearance	purple plate
Formula weight	694.07
Temperature	85(2) K
Wavelength	1.54178 Å
Crystal system	Triclinic
Space group	P-1
Unit cell dimensions	a = 6.43310(10) Å α = 93.799(7)°
	b = 10.1465(2) Å β = 99.392(7)°
	c = 12.4688(9) Å γ = 99.958(7)°
Volume	787.13(6) A^3
Z	1
Density (calculated)	1.460 Mg/m^3
Absorption coefficient	1.430 mm^{-1}
F(000)	358
Crystal size	0.19 x 0.08 x 0.02 mm
Theta range for data collection	3.61° to 68.24°
Index ranges	$-7 \leq h \leq 7$, $-12 \leq k \leq 12$, $-14 \leq l \leq 15$
Reflections collected	20877
Independent reflections	2831 [R(int) = 0.0508]
Completeness to theta	98.2 %
Absorption correction	Semi-empirical from equivalents
Max. and min. transmission	0.9720 and 0.7728
Refinement method	Full-matrix least-squares on F^2
Data / restraints / parameters	2831 / 0 / 244
Goodness-of-fit on F2	1.030
Final R indices [I>2sigma(I)]	R1 = 0.0396, wR2 = 0.1084
R indices (all data)	R1 = 0.0406, wR2 = 0.1095
Largest diff. peak and hole	0.624 and -0.371 e.$Å^{-3}$

*Data collection and structure determination performed by **Jeff Kampf** at the **University of Michigan**.

The iron-sulfur cluster component of the covalently bound complex design, $(Bu_4N)_2[Fe_4S_4(TriS)(SEt)]$, is the same that was used (as a precursor) in Chapter 2. The encapsulating $TriS^{3-}$ ligand aids in the stabilization of the [4Fe-4S] cluster and generates a site-differentiated iron center ideal for ligand exchange to the bridging ligand or, in this design, the functional (hydroxyl) group of the porphyrin.

Previously demonstrated in Chapter 2 is the ease of ligand exchange between thiols and thiolates, especially for the case of the bound ethylthiolate ligand, by an introduced thiol (Figure 3.9). To ensure that ligation of the hydroxyl-functionalized porphyrin to the [4Fe-4S] cluster would occur, the phenolate ligated complex $(Bu_4N)_2[Fe_4S_4(TriS)(OPh)]$ was synthesized as a control (proof of concept). The successful synthesis of the phenolate site-differentiated cluster from the ethylthiolate cluster proves that the hydroxyl group of the functionalized porphyrin should have the ability to protonate the ethylthiolate ligand leaving the phenolate porphyrin to ligate to the cluster.

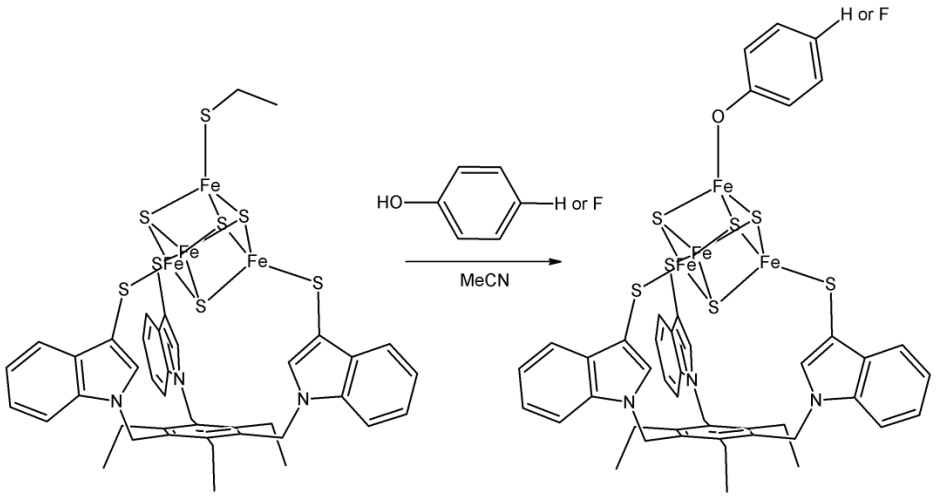

Figure 3.9. Synthetic scheme for the phenolate ligated cubane clusters $(Bu_4N)_2[Fe_4S_4(TriS)(OPh)]$ and $(Bu_4N)_2[Fe_4S_4(TriS)(OPhF)]$.

Synthesis of the fluorinated phenolate site-differentiated cluster, $(Bu_4N)_2[Fe_4S_4(TriS)(OPhF)]$, was undertaken to gauge the sensitivity of the redox potential of the $[Fe_4S_4]^{2+/+}$ couple with respect to the properties of the bound phenolate (similar to the motivation to prepare the fluorinated porphyrin). The reduction potential of the site-differentiated cluster with phenolate ligation is more positive at -750 mV (vs. NHE) compared to that of the ethylthiolate-ligated cluster (-881 mV), analogous to the effect seen in Chapter 2 for the substitution of the less electron donating aromatic thiolates vs. the ethylthiolate ligand (Table 3.2). The redox event for the phenolate ligated cluster is only slightly reversible compared to the typical essentially completely or quasi reversible $[Fe_4S_4]^{2+/+}$ redox couples observed for other site-differentiated cubanes. The fluorine atom substituted at the *para* position of the phenolate ligand has a minimal effect on the redox potential (shifts the potential ~20 mV more negative). Thus, the reduced electron donicity of the aromatic ring, though slight, has a small effect on the redox potential of the [4Fe-4S] core. A larger effect can be expected for the cluster ligated by the functionalized porphyrin. Unusually, the redox process for $(Bu_4N)_2[Fe_4S_4(TriS)(OPhF)]$ is reversible compared to $(Bu_4N)_2[Fe_4S_4(TriS)(OPh)]$, which has an irreversible reduction event. The reason for this difference is not clear.

Table 3.2. Redox potentials of functionalized heme-chloro-complexes and site-differentiated [4Fe-4S] clusters with phenolate ligation (potentials [mV] vs. NHE).

Complex	$E_{½}$ [mV]	redox couple	solvent
$(Bu_4N)_2[Fe_4S_4(TriS)(SEt)]$	-881	$[Fe_4S_4]^{2+/+}$	MeCN
$(Bu_4N)_2[Fe_4S_4(TriS)(OPh)]$	~750 (irr.)	$[Fe_4S_4]^{2+/+}$	MeCN
$(Bu_4N)_2[Fe_4S_4(TriS)(OPhF)]$	-769	$[Fe_4S_4]^{2+/+}$	MeCN
[Fe(*p*TPPOH)Cl]	-298	$Fe^{3+/2+}$	1,2-dce
$[Fe(TPPF_{15}OH)Cl]$	-270	$Fe^{3+/2+}$	1,2-dce

Interestingly, tuning of the redox potential of the heme by introducing fluorine substituents at the phenyl groups has the opposite effect compared to the iron-sulfur cluster as shown in Table 3.2. The ferric heme-chloro-complex [Fe(*p*TPPOH)Cl] has an observed redox event for the ferric/ferrous couple at -298 mV vs NHE. The corresponding fluorinated complex $[Fe(TPPF_{15}OH)Cl]$ shows the $Fe^{3+/2+}$ redox couple at -270 mV, ~30 mV more positive compared to [Fe(*p*TPPOH)Cl]. Since the phenyl groups are attached at the *meso* position of the porphyrin, decreased electron density at these groups does not directly relate to reduced electron density in the π-system of the porphyrin core. Instead, the heavily electron withdrawing fluorine substituents pull electron density from the porphyrin ring (inductive effect) and thus the bound iron center has a slightly increase effective nuclear charge, and correspondingly, the ferric iron is more readily reduced in this case. Thus, it can be speculated that ligation of the iron-sulfur cluster, having an abundance of electron density and being negatively charged, will have an electron donating effect to the phenyl group of the porphyrin ring, and hence this could cause a small shift of the redox potential of the heme iron toward more negative

potentials. In summary, the ligation of the two components of the covalent design will potentially cause the catalytic site heme to be less easily reduced.

3.4 Covalent Bond Formation

The ethylthiolate site-differentiated iron-sulfur cluster $(Bu_4N)_2[Fe_4S_4(TriS)(SEt)]$ was reacted with a molar equivalent of the hydroxyl functionalized porphyrin H_2(*p*-TPP(OH)) in deuterated 1,2-dce-D_4 under static vacuum (Figure 3.10). An ^{1}H-NMR spectrum of the reaction mixture was collected at 5 min, 1 hour, and 36 h. At 5 min and 1 hour, the signal of the ethylthiolate ligand near 13 ppm was still observed; yet, new broad peaks appeared in the aromatic region. After 36 h, neither the signal at 13 ppm for the ethylthiolate ligand nor the signal at 5.66 ppm for the hydroxyl group was observed, and the new broadened peaks in the aromatic region grew in intensity. Hence, while the peaks that matched with the superimposed spectra of the two components declined in intensity, the new signals indicate formation of a product complex. Figure 3.11 shows the final spectrum of the reaction mixture in comparison to the two precursor components for the range of 5.5-14 ppm.

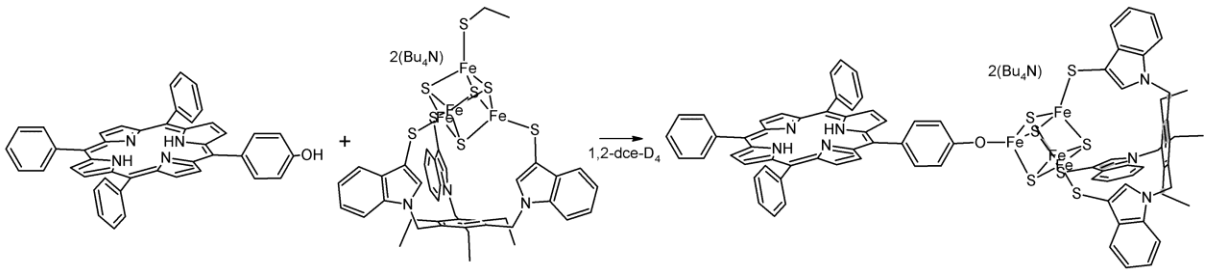

Figure 3.10. Synthetic scheme for the reaction of H_2(*p*-TPP(OH)) and $(Bu_4N)_2[Fe_4S_4(TriS)(SEt)]$ in 1,2-dce-D_4 at room temperature.

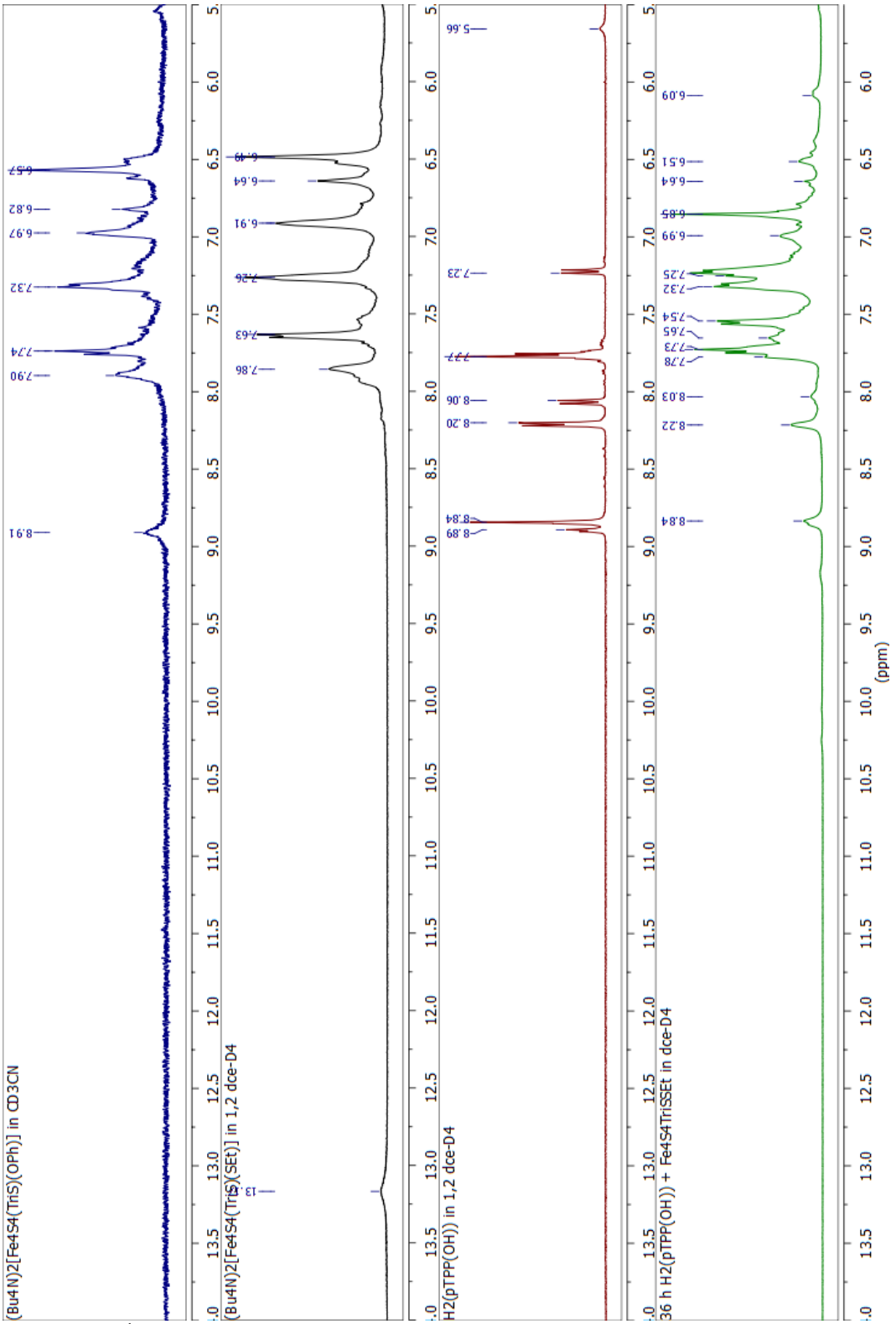

Figure 3.11. ^{1}H-NMR spectra of $(Bu_4N)_2[Fe_4S_4(TriS)(OPh)]$ (blue line), $(Bu_4N)_2[Fe_4S_4(TriS)(SEt)]$ (black line), H_2(*p*-TPP(OH)) (red line), and the reaction mixture of the two after 36 hours reaction time (green line) in 1,2-dce-D4.

The new broad signals in the aromatic region at 8.84, 8.22, 8.03, 7.65, 7.25, 6.64, 6.51, and 6.09 ppm are attributed mostly to the porphyrin. The signals above 8 ppm are likely the β pyrrole protons which did not shift much, and the signals below 6.7 ppm could be the aromatic proton signals of the phenolate of the porphyrin newly ligated to the [4Fe-4S] cluster. In addition, the peaks for the $TriS^{3-}$ ligand protons shifted considerably; for example, the signal at 6.49 shifted to 6.85 ppm and the signal at 6.91 shifted to either 7.32 or 7.25 ppm. It should be noted that the peaks found for the phenolate ligand for the cluster $(Bu_4N)_2[Fe_4S_4(TriS)(OPh)]$ are found in the same region as those for the broadened porphyrin.

The positive result from the reaction of the unmetallated hydroxyl-functionalized porphyrin with the [4Fe-4S] cluster led to multiple crystallization reactions of $(Bu_4N)_2[Fe_4S_4(TriS)(SEt)]$ with [Zn(*p*-TPP(OH))] and [Fe^{II}(*p*-TPP(OH))] in varying solvents. Unfortunately, no growth of crystalline material was observed.

The reaction of [Fe^{II}(*p*-TPP(OH))] with a molar equivalent of the cluster $(Bu_4N)_2[Fe_4S_4(TriS)(SEt)]$ was performed in nitromethane ($MeNO_2$) as an alternative non-coordinating solvent to 1,2-dce in which both components are soluble (Figure 3.12). The bulk-scale reaction solution was split into two equivalent volumes, taken to dryness, and the obtained residue was dissolved in deuterated CD_2Cl_2 and CD_3CN, respectively (Figure 3.13). In addition to the loss of the ethylthiolate ligand from the iron-sulfur cluster, considerable shifting was observed for the signals of the ferrous heme. Further spectroscopic evidence indicated that the heme not only potentially ligated to the site-differentiated iron-sulfur cluster, but also gained an axial ligand, nitric oxide (NO). A qualitative EPR spectrum revealed the typical three line hyperfine signal at a g value ~2

for a ferrous heme nitrosyl complex (S= ½) due to the integer nuclear spin of the nitrogen atom of NO. The UV/Vis absorption spectrum of the product in 1,2-dce shows the Soret absorbance at 408 nm, the same value as for [Fe^{II}(TPP)(NO)], and the FT-IR spectra of the solid shows the N–O stretch at 1671 cm^{-1}. Note that the solvent of this reaction, $MeNO_2$, is known to generate NO via oxidative decomposition over time. For the reaction reported here, freshly distilled $MeNO_2$ was used, but trace amounts of NO were still present in the reaction mixture as evident from [Fe(*p*TPP(OH)(NO)] generation. Residual oxygen or even trace ferric heme or stray Fe^{3+} contaminants from the original cluster synthesis could be the responsible oxidant for NO formation.

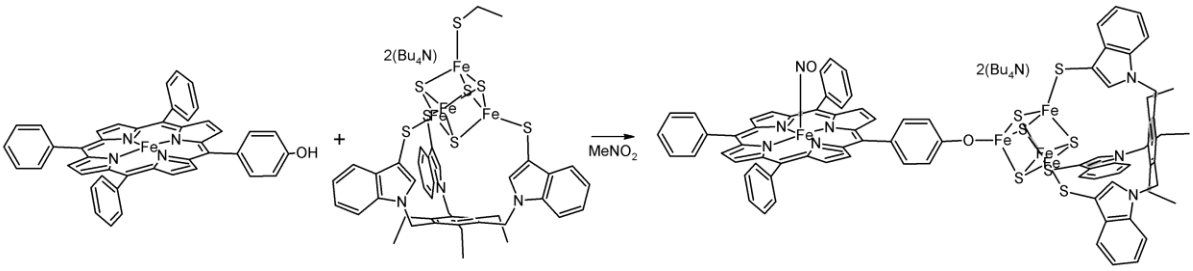

Figure 3.12. Synthetic scheme for the reaction of [Fe^{II}(*p*-TPP(OH))] and $(Bu_4N)_2[Fe_4S_4(TriS)(SEt)]$ in $MeNO_2$ at room temperature.

^{1}H-NMR spectra of [Fe^{II}(*p*-TPP(OH))] and [Fe^{II}(*p*-TPP(OH))(NO)] in the same solvent as the spectra shown in Figure 3.13 are needed to confirm for certain if the shifts in the porphyrin signals are due to ligation to the iron-sulfur cluster or primarily due to the axial coordination of NO and the resulting spin state change of the heme. The consistent shifting of the TriS proton signals as much as 0.1 ppm indicates that the cluster experiences a change in ligation. This effect is larger than what would be expected if the two components were simply coexisting in solution.

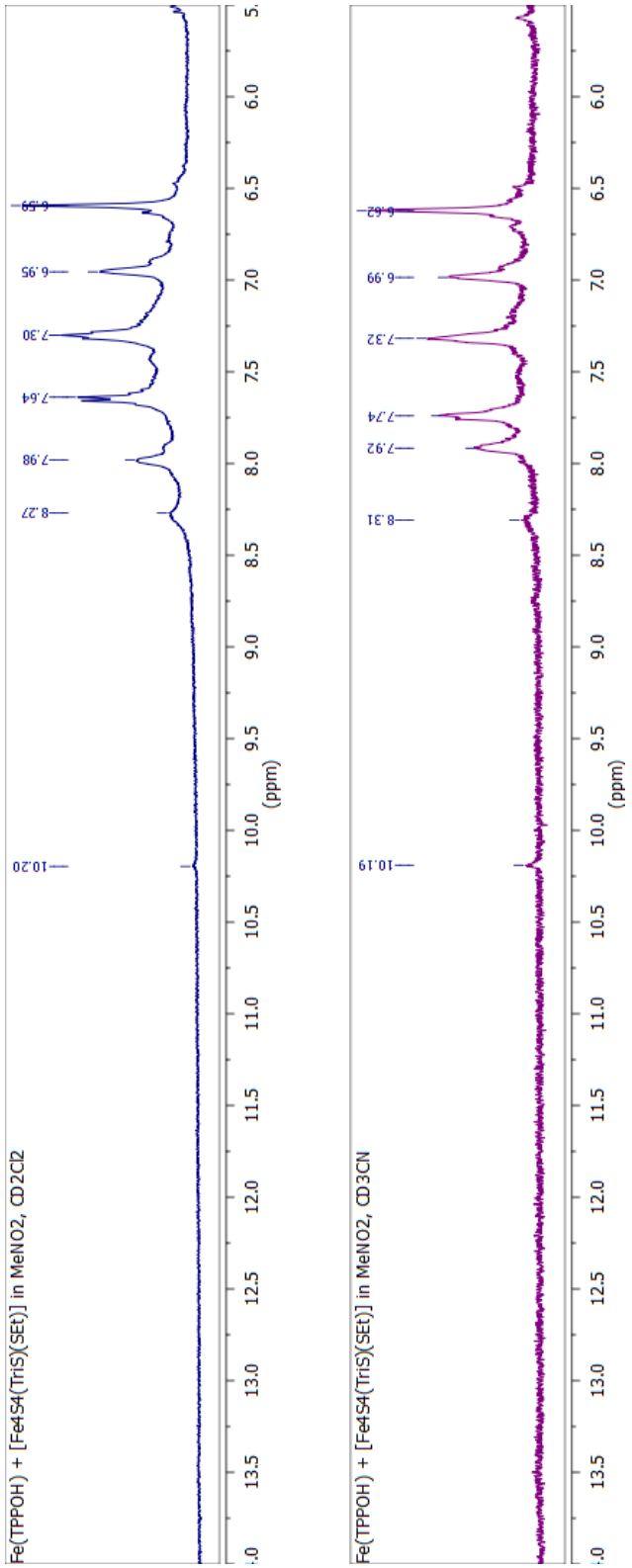

Figure 3.13. ^{1}H-NMR spectra of the isolated product of the reaction of $(Bu_4N)_2[Fe_4S_4(TriS)(SEt)]$ with $[Fe^{II}(p\text{-TPP(OH)})]$ in $MeNO_2$ to form $[Fe^{II}(p\text{-TPP(OH)})(NO)]$. Spectra were taken in CD_2Cl_2 (blue line) and CD_3CN (purple line).

The reaction of $(Bu_4N)_2[Fe_4S_4(TriS)(SEt)]$ with $[Fe^{II}(p\text{-TPP(OH)})]$ in 1,2-dce as monitored by cyclovoltammetry gave inconclusive data that suggest that reaction with dioxygen may have occurred. The plot of the redox events are presented in Figure 3.14, but these plots do not capture the entire result. The resting potential of the heme started at -400 mV which is the reduced state, ferrous iron. With addition of the cluster the redox event at $E_{½}$ ~-250 mV vs Ag/AgCl is no longer present within the potential window, and the resting potential of the mixture increased to -280 mV.

Curiously, the potential of the redox event of the cluster does not seem to have changed upon ligation. The cluster and the heme are at equal concentrations, and the porphyrin ligand reduction occurs at the same potential as the [4Fe-4S] cluster (E_{pc} ~-1100 mV vs Ag/AgCl). Therefore, any shifting in redox potential for the [4Fe-4S] cluster is not visible and cyclovoltammetry is therefore not a good method to monitor binding in this case. The current passed for the cluster and porphyrin ligand reductions at ~-1100 mV is about twice as large as that for the two more positive redox events of the heme iron at E_{pc} ~-300 and -550 mV. This indicates a mixture of two hemes, likely a ferrous and a ferric heme, the latter with an axial ligand like the μ-oxo dimer, creating the two CV signals at E_{pc} ~-300 and -550 mV.

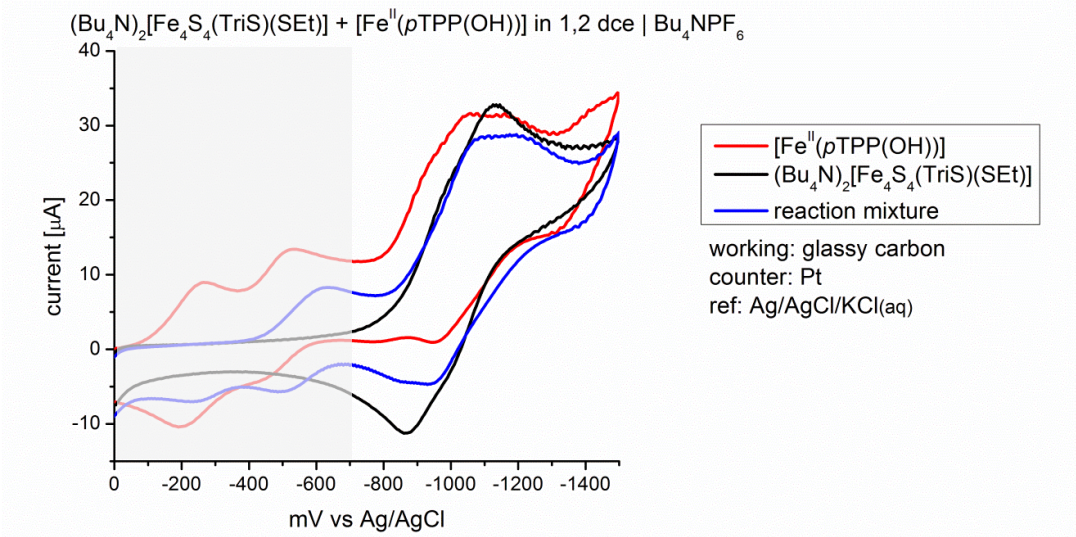

Figure 3.14. Cyclovoltammetry of $(Bu_4N)_2[Fe_4S_4(TriS)(SEt)]$ and $[Fe^{II}(p\text{-}TPP(OH))]$ in 1,2-dce at room temperature (impurity indicated by shaded box).

3.5 Conclusions

As an alternative to the axially coordinated SIR-inspired catalyst design presented in Chapter 2, the covalently bound SIR-inspired catalyst design presented here was derived. The three components of the active site of SIR, the catalytic site, the electron reservoir, and the bridging ligand between the two metal moieties, are maintained in the covalently bound design. The advantage of the covalently bound design is the elimination of the need for strong binding of the axially coordinated bridging ligand to the heme. The synthesis of singly functionalized porphyrins and subsequent metallation with zinc and iron, [M(*p*-TPP(OH))], provides the catalytic site of the design. The first generation catalyst is comprised of a TPP derivative functionalized at a single phenyl group with a hydroxyl group in the *para* position. Here, the hydroxyl group is the designed ligand for coordination to the electron reservoir. The ethylthiolate site-differentiated [4Fe-4S] cluster used as a precursor in Chapter 2 is used here for the covalently bound design as well. The readily protonated ethylthiolate ligand and resulting volatile ethanethiol make

$(Bu_4N)_2[Fe_4S_4(TriS)(SEt)]$ an ideal precursor for cluster ligand exchange. Ligation of phenolate donors to $(Bu_4N)_2[Fe_4S_4(TriS)(SEt)]$ was shown using simple phenols, which readily protonated and replaced the ethylthiolate ligand.

It was further shown that the addition of electron withdrawing fluorine substituents to both the porphyrin at the phenyl groups and to the phenolate ligand of the cluster shifted the redox potentials of the metal centers by ~20-30 mV to more negative and more positive values, respectively. At best this effect can be used to fine tune the redox potentials in a later generation of the catalyst design.

The covalent binding of the two components was initially established by ^{1}H-NMR spectroscopy using the unmetallated, singly functionalized porphyrin, H_2(*p*-TPP(OH)), and reacting it with $(Bu_4N)_2[Fe_4S_4(TriS)(SEt)]$. The loss of the 13 ppm signal for the protons of the ethylthiolate ligand and of the signal at 5.66 for the hydroxyl proton as well as the emergence of new broad aromatic signals all indicate the covalent attachment of the components as desired. The analogous reaction using the ferrous porphyrin [Fe^{II}(*p*-TPP(OH))] in $MeNO_2$ resulted in the formation of the ferrous nitrosyl complex [Fe^{II}(*p*-TPP(OH))(NO)]. However, concomitant shifting of the $TriS^{3-}$ ligands proton signals indicates that the ferrous nitrosyl heme is also bound to the iron-sulfur cluster. Unfortunately, the CV reaction of the same components in MeCN indicates that the porphyrin ring reduction and the cluster reduction occur at similar potentials so that shifting in the cluster CV signals is not discernible to confirm covalent attachment. In addition, a possible oxygen contaminant could be responsible for the two low current redox events observed for the iron of the heme. Insight into the redox behavior of the bound complexes is therefore not available at this point in time. It is likely required to

crystalize the product in order to ultimately confirm the heme-[4Fe-4S] attachment. Further experimentation with [Zn(*p*-TPP(OH))] under the same conditions as used for the CV experiments with the ferrous porphyrins could shed some light on the possible effect of covalent attachment on the [4Fe-4S] cubanes. Electrolysis of the ferrous heme solution to first ensure that the heme is entirely ferrous and not contaminated by ferric complex should be performed in the future before the cluster is added to the reaction mixture.

3.6 References

[1] M. E. Stroupe, E. D. Getzoff, in *Handb. Metalloproteins* (Eds.: A. Messerschmidt, R. Huber, T. Poulos, K. Wieghardt), John Wiley & Sons, Ltd., Chichester, **2001**, pp. 471-485.

[2] B. R. Crane, L. M. Siegel, E. D. Getzoff, *Science* **1995**, *270*, 59.

[3] A. Bondi, *J. Phys. Chem.* **1964**, *68*, 441-451.

[4] P. V. Rao, R. H. Holm, *Chem. Rev.* **2004**, *104*, 527-559.

[5] J. E. Bradshaw, S. Moghaddas, L. J. Wilson, *Gazzetta Chim. Ital.* **1994**, *124*, 159-162.

[6] B. A. Averill, T. Herskovitz, R. H. Holm, J. A. Ibers, *J. Am. Chem. Soc.* **1973**, *95*, 3523-3534.

[7] E. P. L. van der Geer, G. van Koten, R. J. M. Klein Gebbink, B. Hessen, *Inorg. Chem.* **2008**, *47*, 2849-2857.

[8] D. Monti, M. Venanzi, G. Mancini, F. Marotti, L. L. Monica, T. Boschi, *Eur. J. Org. Chem.* **1999**, *1999*, 1901-1906.

[9] L. Huang, Y. Chen, G.-Y. Gao, X. P. Zhang, *J. Org. Chem.* **2003**, *68*, 8179-8184.

[10] K. D. Karlin, A. Nanthakumar, S. Fox, N. N. Murthy, N. Ravi, B. H. Huynh, R. D. Orosz, E. P. Day, *J. Am. Chem. Soc.* **1994**, *116*, 4753-4763.

[11] T. P. Wijesekera, D. A. Dolphin, in *In Metalloporphyrins in Catalytic Oxidations* (Eds.: R. A. Sheldon, Ed., M. Dekker), New York, NY, **1994**, pp. 193-239.

[12] R. A. Ghiladi, R. M. Kretzer, I. Guzei, A. L. Rheingold, Y.-M. Neuhold, K. R. Hatwell, A. D. Zuberbu, K. D. Karlin, *Inorg. Chem.* **2001**, *40*, 5754-5767.

[13] a) A. D. Adler, F. R. Longo, J. D. Finarelli, J. Goldmacher, J. Assour, L. Korsakoff, *J. Org. Chem.* **1967**, *32*, 476-476; b) J. S. Lindsey, R. W. Wagner, *J. Org. Chem.* **1989**, *54*, 828-836.

CHAPTER 4

Bridging Pyridinethiolato Ligated [4Fe-4S] Clusters

(**Deidra L. Gerlach**, Dimitri Coucouvanis, Jeff Kampf, Nicolai Lehnert, "Isolation and Characterization of Single and Sulfide-Bridged Double [4Fe-4S] Cubane Clusters with 4-Pyridinethiolato Ligands"
European Journal of Inorganic Chemistry **2013**, early view.)

4.1 Introduction

The thermodynamic stability of the ferredoxins allows for self-assembly syntheses of clusters of type $[Fe_4S_4(SR)_4]^{2-}$ and $[Fe_4S_4X_4]^{2-}$ in a one pot reaction from ferric chloride, sulfide, a strong base, and mercaptans.[1] The lability of the exogenous ligands of the iron-sulfur clusters in polar coordinating solvents allows for easy ligand exchange for the rational synthesis of clusters with desired properties and structures. Previous publications on iron-sulfur clusters have reported a large variety of thiolate (-SR) clusters synthesized by this method, including those with aliphatic and aromatic R groups incorporating electron withdrawing and electron donating groups, various degrees of side chain lengths and branching, peptides, dendrimer thiolates, di- and tri-thiolates, and site-differentiating thiolate ligands.[2] Other strong σ donor ligands such as phenolates, halides, amines, cyanide, amides, phosphines and crown ethers have also been used as ligands to [4Fe-4S] clusters.[1a, 2-3] A recent publication from the Holm group explores the use of β-cyclodextrin dithiolate ligands to afford water soluble, stable [4Fe-4S] clusters.[4] Thiol exchange of pyridinethiolate ligands with [4Fe-4S] clusters, as

applied here, has been published by Mochida and coworkers with focus on ortho-pyrdinethiol as a bidentate ligand.[5]

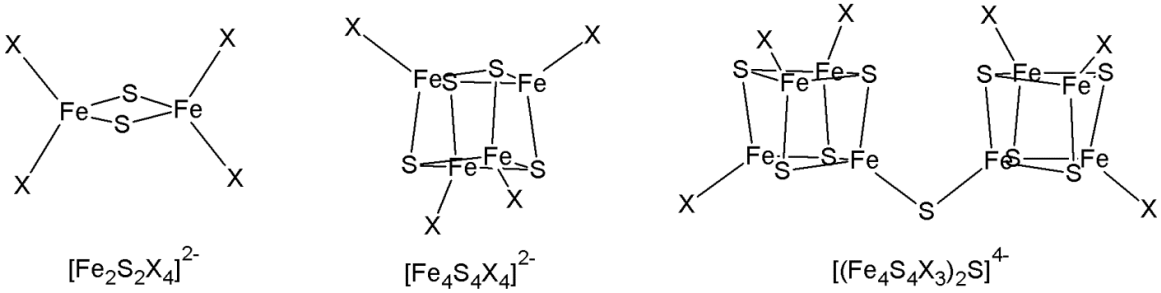

Figure 4.1. Structures of the iron-sulfur dimer cluster $[Fe_2S_2X_4]^{2-}$ (left), cubane cluster $[Fe_4S_4X_4]^{2-}$ (middle), and sulfide-bridged double clubane cluster $[(Fe_4S_4X_3)_2S]^{4-}$ (right), where 'X' is an appropriate anion such as -S-(Cys) in ferredoxins and halides or thiolates in synthetic iron-sulfur clusters.

As previously shown, addition of sulfide to synthetic [4Fe-4S] clusters results in singly μ-sulfido-bridged double cubane clusters (Figure 4.1, right). Crystal structures of these clusters are highly pursued to aid in the structural elucidation and biomimetic synthesis of models of the (Mo/Fe)Fe-cofactor and P-cluster of nitrogenase. Although spectroscopic evidence had previously shown that sulfide-bridged double cubanes do form, only three crystal structures of sulfide bridged cubane clusters have been published so far.[3b, 6] The first structure was reported by Paul Challen from the Coucouvanis group and was obtained for the all chloro-cubane using mixed counter ions.[6b] Recently, two sulfide-bridged cubane clusters ligated by newly reported encapsulating ligands, $Temp(SH)_3$ and $Tefp(SH)_3$, were prepared and structurally characterized by the Tatsumi group (Figure 4.2).[6d] Each one of these sulfide-bridged clusters is unique within a range of Fe-S-Fe bond angles for the bridge, and rotations of the iron-sulfur cubanes with respect to each other. Challen's all-chloro bridged-cubane is the most symmetrical with C_{2v} symmetry. On the other hand, Tatsumi's bridged cluster using the $TefpS_3$

encapsulating ligand has a near linear (and disordered) sulfide bridge between the two clusters. It is not clear whether it is the polarity of the *para*-group of the phenylthiolate of Tatsumi's encapsulating ligand or if it is the crystal packing that is responsible for the large effect on the bond angle for these complexes in the solid state. Further analysis is provided below in the Structural Details and Comparison section.

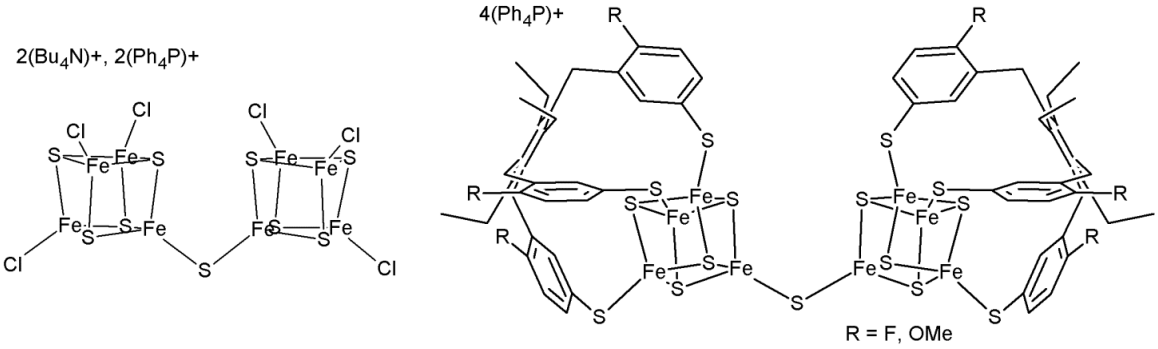

Figure 4.2. Structures of previously published sulfide-bridged [4Fe-4S] cubane clusters: $(Bu_4N)_2(Ph_4P)_2[(Fe_4S_4Cl_3)_2S]$ (left)[6b] and $(Ph_4P)_4[(Fe_4S_4(TempS_3))_2S]$ (R = OMe) and $(Ph_4P)_4[(Fe_4S_4(TefpS_3))_2S]$ (R = F, right).[6d]

The motivation of this research was for the isolation of simple cubane clusters equipped with bridging ligands. We report the synthesis and characterization of two new iron-sulfur clusters coordinated by *para*-substituted pyrdinethiolate ligands, $(Bu_4N)_2[Fe_4S_4(SPy)_4]$ and $(Bu_4N)_2[Fe_4S_4(SMePy)_4]$, which are ligated by 4-pyridinethiolate ($^-$SPy) and 4-pyridinemethylthiolate ($^-$SMePy), respectively. Excitingly, we also present the fourth crystal structure of a sulfide-bridged cubane cluster with 4-pyridinethiolate as the exogenous ligand, $(Bu_4N)_4[(Fe_4S_4(SPy)_3)_2S]$. Finally, we report the properties of the one electron reduced sulfide-bridged cubane cluster using electron paramagnetic resonance (EPR) spectroscopy.

4.2 Methods and Experimental Procedures

General Procedures. All cluster syntheses were performed under a nitrogen atmosphere in a glove box and by utilizing common Schlenk line techniques. ^{1}H-NMR spectra were acquired on a Varian MR400 400 MHz spectrometer and referenced to solvent. Mid-IR spectra were collected on a Perkin Elmer Spectrum BX FT-IR spectrometer and Far-IR data were obtained on a Nicolet 740 FT-IR spectrometer in KBr pellets. Elemental analyses were performed by Atlantic Mircolab, Inc., Norcross, GA. Electronic spectra were measured on a Varian CARY 1E UV-Visible spectrometer. Cyclic voltammetry experiments were conducted in 0.1 M solutions of Bu_4NPF_6 in acetonitrile (MeCN) with a glassy carbon working electrode, a Pt counter electrode and a Ag/AgCl reference electrode on a EG&G Princeton Potentiostat/Galvanostat model 263A. The redox potentials are calibrated to Fc/Fc^+ and reported vs. NHE. Electron paramagnetic resonance (EPR) spectra were collected on a Bruker X-Band EMX electron spin resonance spectrometer equipped with a Varian liquid nitrogen cryostat (at approximately 80 K) and with an Oxford Instruments liquid helium cryostat (at temperatures ranging from 4 to 65 K). EPR spectra were collected on frozen solutions using 20 mW microwave power and 100 kHz field modulation with the amplitude set to 1 G.

Materials. All solvents were purified by distillation and degassed. All reagents were used as purchased. $(Bu_4N)_2[Fe_4S_4(SEt)_4]$ was prepared according to published procedures. [1a]

Synthesis of 4-pyridinemethylthiol (PyMeSH). Previously reported syntheses were modified as described in the following.[7] 4-Chloromethylpyridine hydrochloride

(5.00 g, 30.5 mmol) was dissolved in 30 mL of MeOH and heated to reflux while stirring in a round bottom flask equipped with a reflux condenser and a slow addition funnel loaded with thiourea (5.80 g, 76.2 mmol) dissolved in 100 mL of MeOH. The thiourea solution was added drop wise to the refluxing reaction mixture. After the addition was complete the solution was refluxed for an additional 1 ½ to 2 h. The solution was allowed to cool to room temperature, and the volume of solvent was reduced under vacuum until solid precipitate was observed. The resulting concentrated solution was cooled to -10 °C overnight. The resulting beige precipitate was collected via suction filtration, washed with cold MeOH, and dried under vacuum over P_2O_5. The filtrate volume was reduced and cooled again to afford additional collections of solid 4-methylpyridineisothiouronium chloride for a total yield of 4.93 g (82 % yield).

The thiouronium salt (2.5 g, 12.3 mmol) was dissolved in 50 mL of deionized (DI) water, and excess solid $NaBH_4$ (2.3 g, 60.8 mmol) was added slowly with stirring. The solution was stirred for 30 minutes and then acidified with 6 M HCl until a pH of 6 was reached (and maintained). The resulting thiol was extracted with 70 mL of $CHCl_3$ (x4), washed with DI water, and dried over Na_2SO_4. The solvent was then removed via vacuum to afford a yellow oil (2.6 g, 83 %). ^{1}H-NMR (400 MHz, CD_3OD, rt, ppm): δ 8.45 (d, 2 H), 7.43 (d, 2 H), 3.74 (s, C*H*$_2$, 2 H).

Synthesis of $(Bu_4N)_2[Fe_4S_4(SPy)_4]$. $(Bu_4N)_2[Fe_4S_4(SEt)_4]$ (0.88 g, 0.81 mmol) was dissolved in 30 mL of MeCN and stirred in a glove box. Solid 4-pyrdinethiol (PySH) (0.45 g, 4.05 mmol) was added to the solution, and the flask was sealed and evacuated. The reaction mixture was allowed to stir under static vacuum for 1 hour. The resulting solution was filtered through a medium frit. The filtrate was layered with 100 mL Et_2O to

diffuse overnight. The resulting black solid was a mixture of crystals and amorphous solid and collected by suction filtration, washed with 5 mL of Et_2O, and dried under vacuum. The bulk of the resulting solid when analyzed by ^{1}H-NMR indicated a ratio of 12:1 of $(Bu_4N)_2[Fe_4S_4(SPy)_4]$ to $(Bu_4N)_4[(Fe_4S_4(SPy)_3)_2S]$. The resulting solid mixture was recrystallized several times from MeCN solution, layered with Et_2O, until discernible black, cubic crystals were collected. ^{1}H-NMR (400 MHz, CD_3CN, rt, ppm): δ SPy: 8.96 (s), 5.92 (broad s), δ Bu_4N^+: 3.10 (broad m, 16 H), 1.63 (broad m, 16 H), 1.36 (broad m, 16 H), and 0.98 (broad m, 24 H) (see Figure 4.5). FT-IR (KBr, cm^{-1}): 2958 (m), 2871 (m), 1567 (s), 1527 (w), 1475 (s), 1405 (w), 1378 (w), 1261 (w), 1213 (w), 1099 (m), 1062 (w), 1025 (w), 982 (w), 875 (w), 803 (m), 703 (s), 495 (w), 426 (w), 357 (w) (see Figure 4.8). CV (MeCN, 0.01 M): -401.2 mV $[Fe_4S_4]^{2+/1+}$ (see Figure 4.21). Anal. Calcd. for $C_{52}H_{88}N_6S_8Fe_4$: C, 48.90%; H, 6.90%; N, 6.60 %; S, 20.10%. Found: C, 48.82%; H, 6.84%; N, 6.48%; S, 20.24%.

Synthesis of $(Bu_4N)_2[Fe_4S_4(SMePy)_4]$. $(Bu_4N)_2[Fe_4S_4(SEt)_4]$ (0.44g, 0.41 mmol) was dissolved in 20 mL of MeCN, and the oil PyMeSH (0.26 g, 2.1 mmol) was added via syringe while stirring in a glove box. The reaction vessel was sealed and a vacuum was applied. The reaction was allowed to stir for 3 hours under static vacuum. The reaction mixture was filtered, and the filtrate was layered with 100 mL of Et_2O. The black precipitate was collected by vacuum filtration, washed with ether, and dried under vacuum to yield 0.43 g of a black solid product (79% yield). ^{1}H-NMR (400 MHz, CD_3CN, rt, ppm): δ SMePy: 13.29 (broad s, C*H*$_2$S), 8.50 (broad s), 7.55 (broad s), δ Bu_4N^+: 3.05, 1.58, 1.35, 0.95 (see Figure 4.6). FT-IR (KBr, cm^{-1}): 2961 (m), 2870 (w), 1596 (m), 1557 (w), 1480 (m), 1409 (m), 1380 (w), 1261 (s), 1203 (w), 1098 (broad s),

1023 (broad s), 990 (m), 869 (m), 736 (w), 687 (w), 561 (w), 483 (w), 424 (w), 356 (w) (see Figure 4.7). CV (MeCN, 0.01 M): -742 mV $[Fe_4S_4]^{2+/1+}$ and -1459 mV $[Fe_4S_4]^{1+/0}$ (see Figure 4.20).

Synthesis of $(Bu_4N)_4[(Fe_4S_4(SPy)_3)_2S]$. $(Bu_4N)_2[Fe_4S_4(SEt)_4]$ (0.44 g, 0.41 mmol) was dissolved in 30 mL of MeCN and solid PySH (0.27 g, 2.43 mmol) and Na_2S (0.03 g, 0.38 mmol) were added while stirring in a glove box. The reaction vessel was sealed and a vacuum was applied. The reaction was allowed to stir for 24 hours under static vacuum. The reaction mixture was filtered and the filtrate was layered with 100 mL of Et_2O. The resulting black solid was a mixture of crystals and amorphous solid and collected by suction filtration, washed with 5 mL of Et_2O, and dried under vacuum. The bulk of the resulting solid when analyzed by ^{1}H-NMR indicated a ratio of 5:1 of $(Bu_4N)_4[(Fe_4S_4(SPy)_3)_2S]$ to $(Bu_4N)_2[Fe_4S_4(SPy)_4]$ or better. The resulting solid mixture was recrystallized several times from MeCN solution, layered with Et_2O, until discernible black, rod-like crystals were collected. Often the crystals were accompanied by other solid material and manual separation was necessary to collect pure product. ^{1}H-NMR (400 MHz, CD_3CN, rt, ppm): $\underline{\delta\ SPy}$: 9.15 (broad s), 5.13 (broad s), $\underline{\delta\ Bu_4N^+}$: 3.09, 1.64, 1.37, 0.97 (see Figure 4.5, right). FT-IR (KBr, cm^{-1}): 2955(m), 2869(m), 1567 (s), 1524 (w), 1474 (s), 1403 (m), 1377 (m), 1309 (w), 1261 (w), 1214 (w), 1100 (m), 1062 (w), 1022 (w), 981 (m), 876 (w), 803 (s), 704 (s), 495 (m), 427 (w), 367 (w) (see Figure 4.9). CV (MeCN, 0.01 M): $E_{½}$: -528 mV $[(Fe_4S_4)_2S]^{4+/3+}$, E_{pc}:-828 mV $[(Fe_4S_4)_2S]^{3+/2+}$, ~-1050 mV $[(Fe_4S_4)_2S]^{2+/1+}$, ~ -1370 mV $[(Fe_4S_4)_2S]^{1+/0}$ (see Figure 4.22). Anal. Calcd. for $C_{94}H_{168}N_{10}S_{15}Fe_8$: C, 47.70%; H, 7.20%; N, 5.90%; S, 20.30%. Found: C, 47.13%; H, 7.11%; N, 5.91%; S, 20.47%.

Reduction of $(Bu_4N)_2[Fe_4S_4(SPy)_4]$ and $(Bu_4N)_4[(Fe_4S_4(SPy)_3)_2S]$.[8] Solid $(Bu_4N)_2[Fe_4S_4(SPy)_4]$ (5.4 mg, 0.00423 mmol) and $(Bu_4N)_4[(Fe_4S_4(SPy)_3)_2S]$ (9.8 mg, 0.00414 mmol) were deposited into two separate 2 mL volumetric flasks. A stock solution of the reductant, 36 mM Na•acenaphthylene, was prepared in a 10 mL volumetric flask by dissolving 65.1 mg acenaphthylene (0.428 mmol) in ~ 6 mL THF, adding 8.3 mg Na metal (0.361 mmol), diluting to 10 mL with THF, and letting the suspension stir for several hours. A 8.31 mM stock solution of Bu_4NBr was prepared by dissolving 13.4 mg (0.0416 mmol) in a ~4:1 THF/MeCN mixture in a 5 mL volumetric flask. Each cluster was dissolved in 0.3 mL MeCN in the volumetric flask to which 0.5 mL of the 8.31 mM Bu_4NBr solution and 0.12 mL of the 36 mM Na•acenaphthylene solution were added. The resulting solutions were shaken and let sit for 20 minutes. The resulting dark solutions were then filtered through celite which collected an insignificant amount of black precipitate. The resulting filtrate was loaded into quartz EPR tubes, sealed, and frozen for EPR spectroscopy.

4.3 Pyridinethiolate Cluster Syntheses

The precursor iron-sulfur cubane cluster $[Fe_4S_4(SEt)_4]^{2-}$ with exogenous ethylthiolate ligands is easily prepared in a one pot, self-assembly reaction under anaerobic conditions.[1a] From the straightforwardly obtained tetraethylthiolate cubane cluster, thiol-exchange is often readily accomplished by addition of an acidic thiol. Here, the acidic thiol will transfer the thiol proton to the ethylthiolate ligand in polar solvents where the ethylthiolate ligand is labile. The highly volatile ethanethiol is readily removed under vacuum, allowing the direct ligation of the introduced thiol to the iron-sulfur

cluster. This synthetic route works well with 4-pyridinemethylthiol and is evidently occurring for 4-thiolpyridine as well to produce the clusters $(Bu_4N)_2[Fe_4S_4(SMePy)_4]$ and $(Bu_4N)_2[Fe_4S_4(SPy)_4]$, respectively. However, in the presence of just 4-thiolpyridine without added sulfide, free sulfide is also liberated from the cubanes in solution, indicating that a decomposition of some of the iron-sulfur clusters aided by ligation to 4-thiolpyridine is also occurring, which is quite unusual. Importantly, it has been shown previously that in a polar solvent, particularly protic solvents, the tautomerization of 4-pyrdinethiol to 4-pyridinethione readily occurs with strong preference for the thione (Figure 4.3).[9] Hence, most of the pyrdinethiol is in the thione form in the reaction mixture with acetonitrile as the solvent. The presence of the pyridinethione in solution apparently destabilizes the cluster possibly due to the increased acidity of the pyridinium over thiol leading to the liberation of sulfide from the iron-sulfur cluster core..[10] As a result, a mixture of the single cubane and the singly sulfide-bridged double cubane $(Bu_4N)_4[(Fe_4S_4(SPy)_3)_2S]$ is formed in solution, and appears to be in equilibrium in polar solvents. For example, when recrystallizing the pure single cubane, a minor fraction of the precipitated solid is identified as the sulfide-bridged double cubane cluster generated in the recrystallization process. In reactions where free sulfide is introduced as the sodium salt, the concentration of the sulfide-bridged iron-sulfur cubane increases to become the major cubane cluster present in solution, although a minor fraction of the single cubane is also generated in the synthesis. In contrast, no cluster decomposition and formation of double cubanes is observed with 4-pyridinemethylthiol, providing further support to the idea that the decomposition is linked to the tautomerization of the pyrdinethiol. Figure 4.4 shows the syntheses of these iron-sulfur clusters.

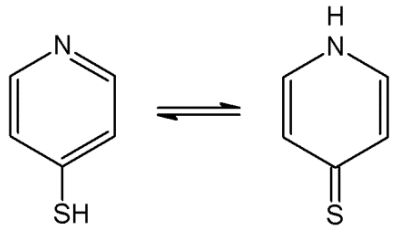

Figure 4.3. The tautomerization of 4-pyrdinethiol to 4-pyridinethione.

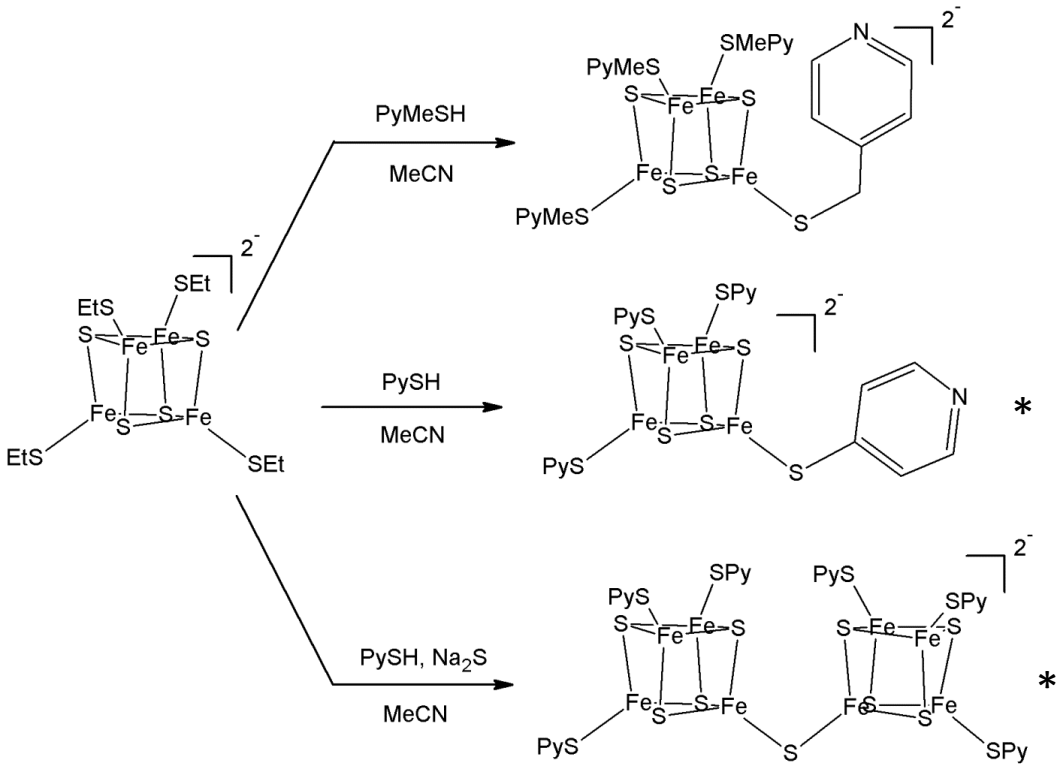

Figure 4.4. Synthesis of $(Bu_4N)_2[Fe_4S_4(SMePy)_4]$ (top right), $(Bu_4N)_2[Fe_4S_4(SPy)_4]$ (middle right), and $(Bu_4N)_4[(Fe_4S_4(SPy)_3)_2S]$ (bottom right). The asterisk indicates the major product of a synthesis.

Unfortunately, the similarity in polarity of the single and double cubane clusters with pyrdinethiolate ligands, and thus the similarity in solubility, makes separation by crystallization nearly impossible. Chromatography has not been a viable means for separation of these clusters either, as most separation media either irreversibly trap the clusters or decompose the clusters. Successful individual crystallization of the single

cubane cluster and the singly sulfide-bridged double cubane was achieved by slow diffusion of ether into acetonitrile solutions of the cluster mixtures. Separation was only possible by physical (manual) separation of individual crystals of the two iron-sulfur clusters in the recrystallization batches. The single cubane crystallizes as square and rectangular block crystals, whereas the singly sulfide-bridged double cubane crystalizes as thin rod-like crystals and larger thin plate crystals. Most often both clusters will precipitate as powder together or will crystallize partially as the other cluster deposits on the growing crystals. The ability to distinguish the crystals of the pure cubane clusters from each other by eye and to grow larger crystals permits physical separation of the crystals by hand with a needle and static. Milligrams of crystals can be collected over a few hours of separation by this means. The purity of these collections can be easily verified by ^{1}H-NMR via the unique signals of the aromatic protons of the pyridinethiolate ligands (Figures 4.5 for the pure compounds versus Figure 4.6 (left) for the crude material collected from a synthesis of the sulfide-bridged double cubane). Due to the added steric hindrance in the sulfide-bridged double cubane, the free rotation of the pyridine rings about the iron-thiolate sulfur bonds as well as the rotation of the exogenous Fe-S bond of the sulfide is limited and thus, the *ortho*-hydrogen peak at 5.13 ppm is observed to be sharper in the double cubane complex compared to the analogous peak for the single cluster (at 5.92 ppm). In addition, the extra electron density due to the sulfide-bridge shifts the *ortho*- and *meta*-hydrogen signals up-field and down-field (5.13 and 9.15 ppm), respectively, compared to the analogous signals for $(Bu_4N)_2[Fe_4S_4(SPy)_4]$ at 5.92 and 8.96 ppm. This distinction of the peak positions in the ^{1}H-NMR spectra was used to gather pure materials for further characterization.

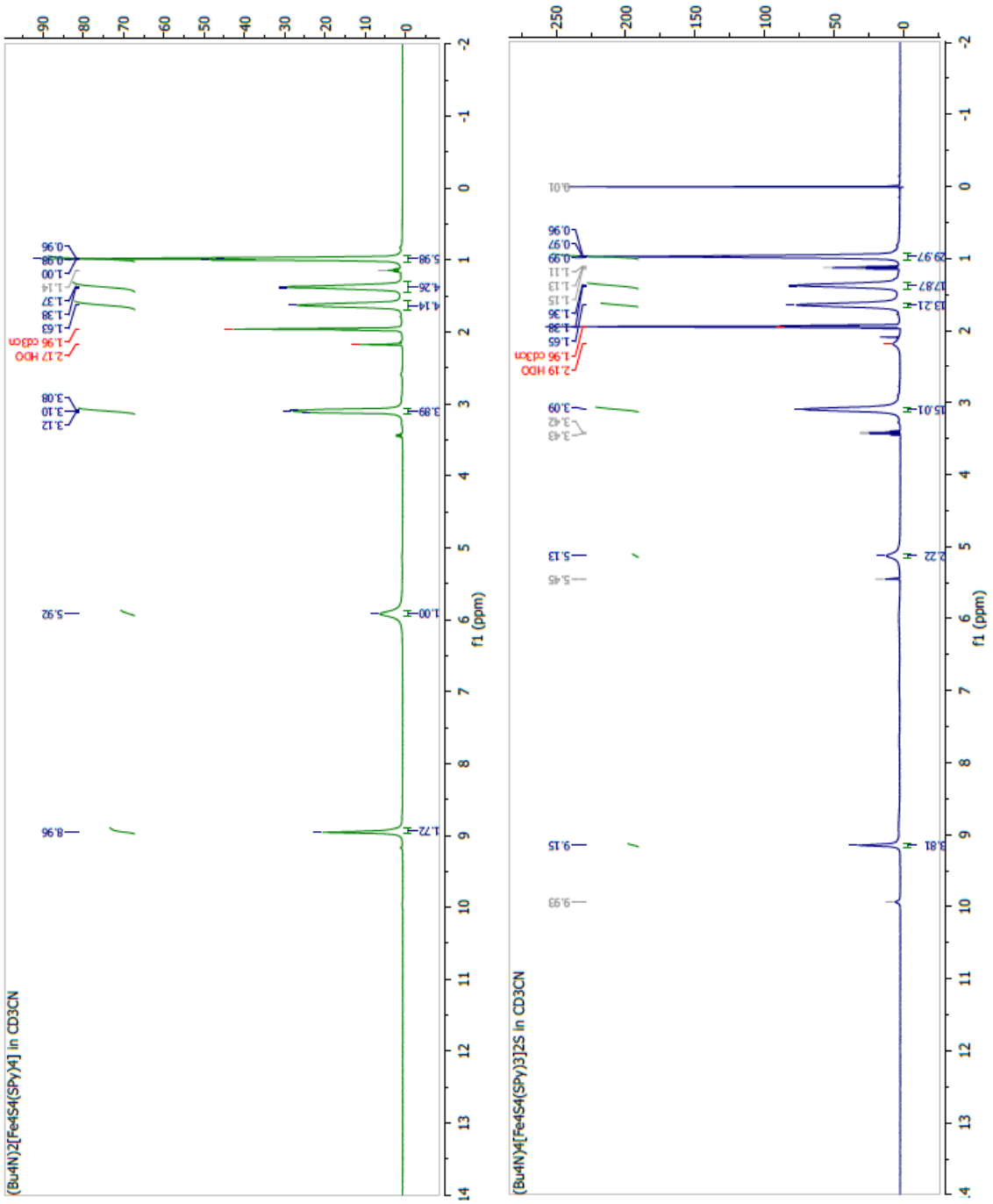

Figure 4.5. ^{1}H-NMR spectra of $(Bu_4N)_2[Fe_4S_4(SPy)_4]$ (left) and $(Bu_4N)_4[(Fe_4S_4(SPy)_3)_2S]$ (right) in CD_3CN.

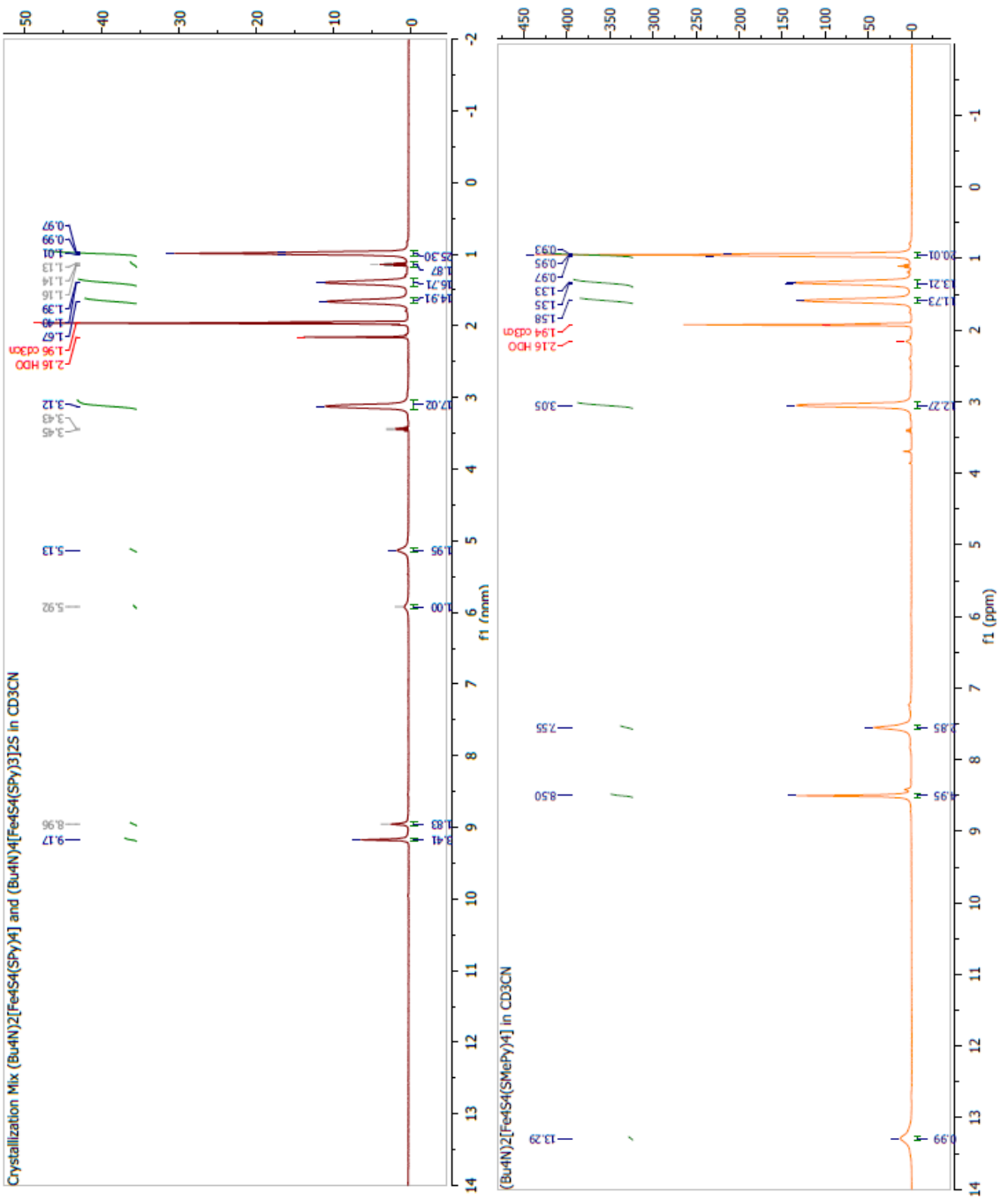

Figure 4.6. ^{1}H-NMR spectra of a mixture of $(Bu_4N)_4[(Fe_4S_4(SPy)_3)_2S]$ and $(Bu_4N)_2[Fe_4S_4(SPy)_4]$ (left) and $(Bu_4N)_2[Fe_4S_4(SMePy)_4]$ (right) in CD_3CN.

The Fe-S stretch observed in the far-infrared region is often used as a fingerprint for iron-sulfur clusters undergoing ligand exchange. Not surprisingly, the far-IR spectra of $(Bu_4N)_2[Fe_4S_4(SPy)_4]$ and $(Bu_4N)_2[Fe_4S_4(SMePy)_4]$ (shown in Figures 4.8 and 4.7, respectively), are similar: both exhibit the most intense signal at 356 cm^{-1}, which is relatively sharp for this spectral region, indicating a high degree of symmetry in the Fe-S bonds. In contrast, the Fe-S stretch of the sulfide-bridged cluster $(Bu_4N)_4[(Fe_4S_4(SPy)_3)_2S]$ at 367 cm^{-1} is broader, and multiple shoulders are visible on the main signal indicating a loss of symmetry for the two bridged [4Fe-4S] clusters (Figures 4.8 and 4.9, respectively). A similar spectrum results for Challen's sulfide-bridged cluster $(Bu_4N)_2(Ph_4P)_2[(Fe_4S_4Cl_3)_2S]$ where five distinct shoulders are observed on the Fe-S stretching band.[11]

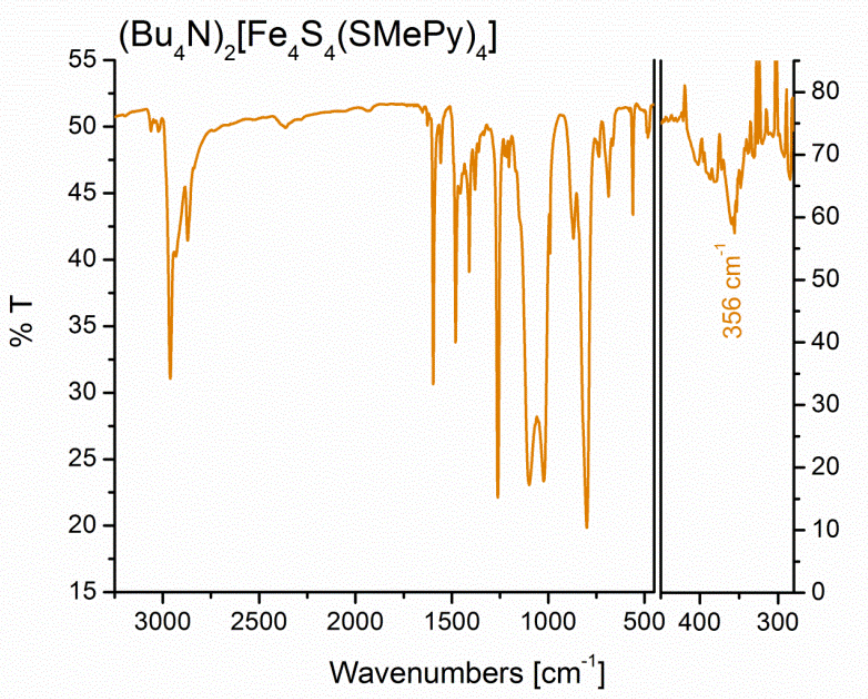

Figure 4.7. Mid- (left) and Far-IR (right) spectra of $(Bu_4N)_2[Fe_4S_4(SMePy)_4]$.

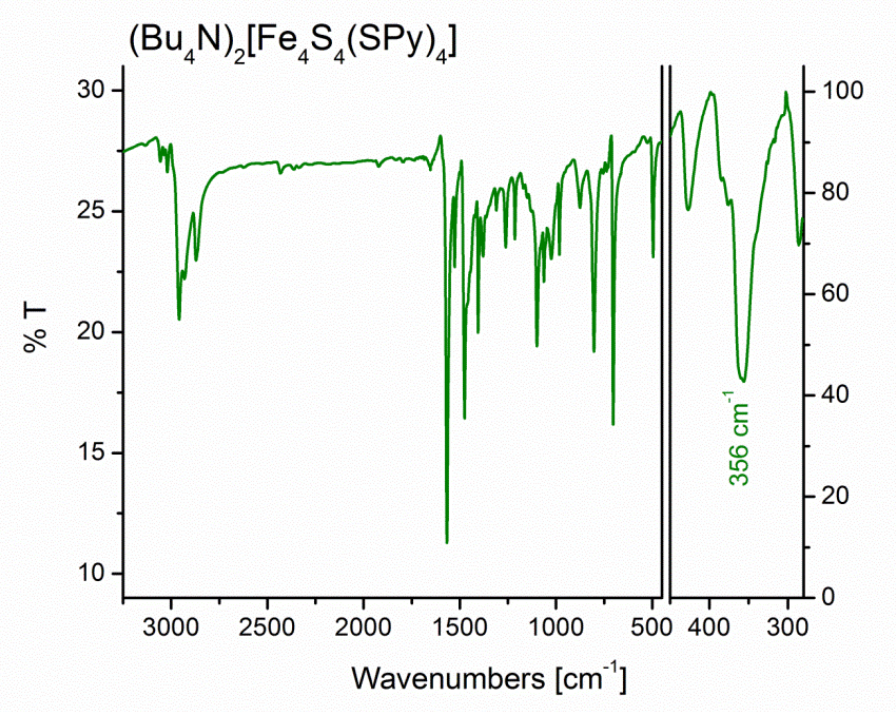

Figure 4.8. Mid- (left) and Far-IR (right) spectra of $(Bu_4N)_2[Fe_4S_4(SPy)_4]$.

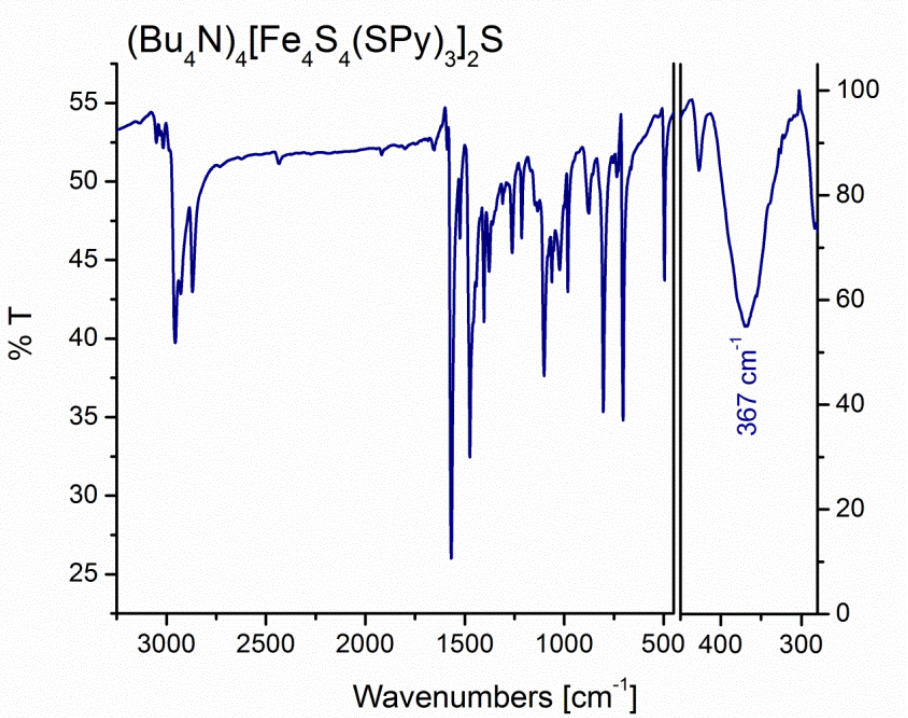

Figure 4.9. Mid- (left) and Far-IR (right) spectra of $(Bu_4N)_4[(Fe_4S_4(SPy)_3)_2S]$.

FT-IR spectroscopy is also helpful in identifying decomposition of the iron-sulfur clusters in the presence of chlorinated solvents. Seen in Figure 4.10 is the Mid- and Far IR spectra for the material that results when $(Bu_4N)_2[Fe_4S_4(SPy)_4]$ is left in chlorinated solvent over several days to produce the all chloro-cluster $(Bu_4N)_2[Fe_4S_4Cl_4]$.

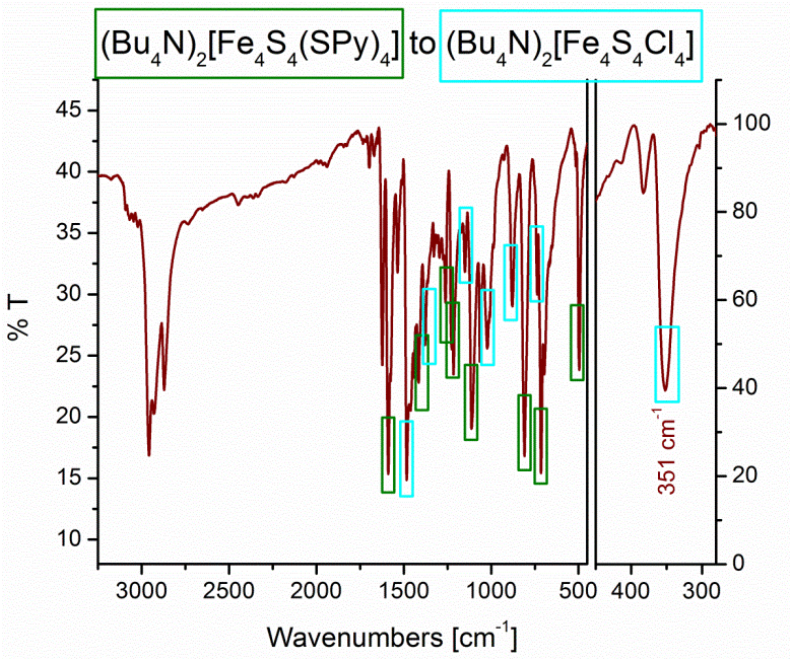

Figure 4.10. Mid- (left) and Far-IR (right) spectra of solid isolated after $(Bu_4N)_2[Fe_4S_4(SPy)_4]$ was dissolved in 1,2-dichloroethane for several days and recollected by precipitation. The boxes in green indicate signals assigned to $(Bu_4N)_2[Fe_4S_4(SPy)_4]$ and boxes in teal indicate signals assigned to $(Bu_4N)_2[Fe_4S_4Cl_4]$.

4.4 Crystal Structures of $(Bu_4N)_2[Fe_4S_4(SPy)_4]$ and $(Bu_4N)_4[(Fe_4S_4(SPy)_3)_2S]$

Black needles of **$(Bu_4N)_4[(Fe_4S_4(SPy)_3)_2S]$** were grown by layering Et_2O over a MeCN solution of the compound at room temperature. A crystal of dimensions 0.47 x 0.22 x 0.005 mm was mounted on a Bruker SMART APEX-I CCD-based X-ray diffractometer equipped with a low temperature device and fine focus Mo-target X-ray tube (λ = 0.71073 Å) operated at 1500 W power (50 kV, 30 mA). The X-ray intensities were measured at 85(1) K; the detector was placed at a distance of 5.055 cm from the

crystal. A total of 2220 frames were collected with a scan width of 0.5° in ω and 0.45° in φ with an exposure time of 75 s/frame. The integration of the data yielded a total of 164432 reflections to a maximum 2θ value of 48.78° of which 18681 were independent and 12528 were greater than 2σ(I). The final cell constants (Table 4.1) were based on the xyz centroids of 9849 reflections above 10σ(I). Analysis of the data showed negligible decay during data collection; the data were processed with SADABS and corrected for absorption. The structure was solved and refined with the Bruker SHELXTL (version 2008/4) software package, using the space group P1bar with Z = 2 for the formula $C_{94}H_{168}N_{10}S_{15}Fe_8$. All non-hydrogen atoms were refined anisotropically with the hydrogen atoms placed in idealized positions. Full matrix least-squares refinement based on F^2 converged at R1 = 0.0562 and wR2 = 0.1280 [based on I > 2σ(I)], and R1 = 0.1009 and wR2 = 0.1476 for all data. Additional details are presented in Table 4.1.

Statement for structure determination of $(Bu_4N)_2[Fe_4S_4(SPy)_4]$. Although the GooF and R-factors are high but not severe for the preliminary structure of $(Bu_4N)_2[Fe_4S_4(SPy)_4]$, the connectivity and chemical identity of the crystal components are readily confirmed for the anion and the two ammonium counter ions. Unfortunately, even though sharp diffraction signals were collected, some unresolved problem (possibly twinning or pseudo-symmetry in the crystal) exists which prevents the determination of a final model and is evident in the number of A- and B-alerts in the checkcif file seen in the excerpt included in Figure 4.11.

Table 4.1. Crystal data and structure refinement for $(Bu_4N)_4[(Fe_4S_4(SPy)_3)_2S]$.

Compound	**$(Bu_4N)_4[(Fe_4S_4(SPy)_3)_2S]$* CCDC 947515**
Empirical formula	$C_{94}\ H_{168}\ Fe_8\ N_{10}\ S_{15}$
Appearance	black rod
Formula weight	2366.08
Temperature	85(2) K
Wavelength	0.71073 Å
Crystal system	Monoclinic
Space group	P2(1)/n
Unit cell dimensions	a = 19.807(2) Å α = 90 ° b = 23.032(3) Å β = 97.860(2) ° c = 25.315(3) Å γ = 90 °
Volume	11440(2) $Å^3$
Z	4
Density (calculated)	1.374 Mg/m^3
Absorption coefficient	1.304 mm^{-1}
F(000)	5000
Crystal size	0.47 x 0.22 x 0.01 mm
Theta range for data collection	1.85 to 24.39 °
Index ranges	$-22 \le h \le 22$, $-26 \le k \le 26$, $-29 \le l \le 29$
Reflections collected	164432
Independent reflections	18681 [R(int) = 0.1135]
Completeness to theta	99.4 %
Absorption correction	Semi-empirical from equivalents
Max. and min. transmission	0.9935 and 0.5794
Refinement method	Full-matrix least-squares on F^2
Data / restraints / parameters	18681 / 266 / 1244
Goodness-of-fit on F2	1.055
Final R indices [I>2sigma(I)]	R1 = 0.0562, wR2 = 0.1280
R indices (all data)	R1 = 0.1009, wR2 = 0.1476
Largest diff. peak and hole	1.333 and -0.843 e. $Å^{-3}$

*Data collection and structure determination performed by **Jeff Kampf** at the **University of Michigan**.

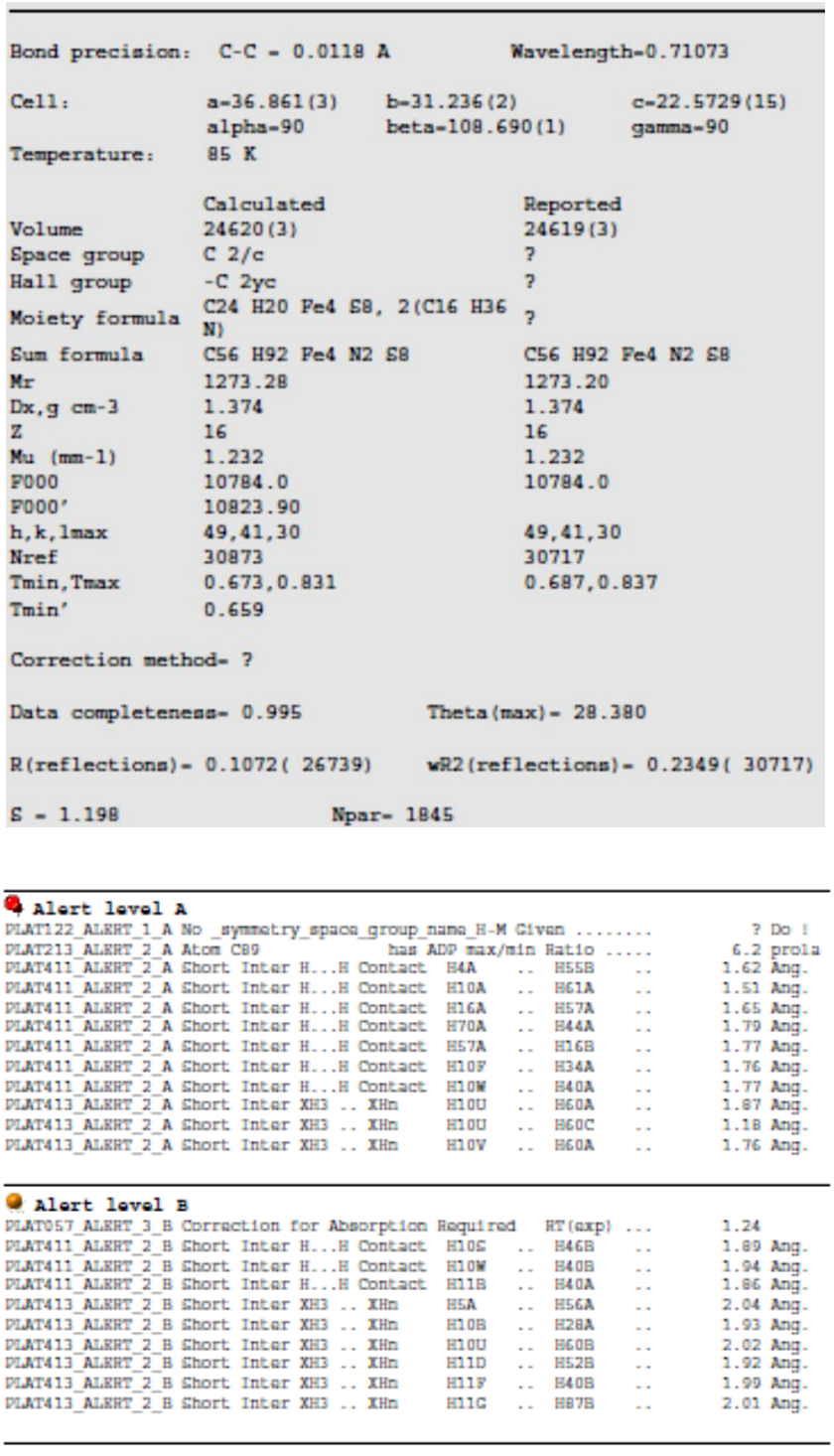

```
Bond precision:  C-C = 0.0118 A          Wavelength=0.71073

Cell:            a=36.861(3)    b=31.236(2)         c=22.5729(15)
                 alpha=90       beta=108.690(1)     gamma=90
Temperature:     85 K

                 Calculated                 Reported
Volume           24620(3)                   24619(3)
Space group      C 2/c                      ?
Hall group       -C 2yc                     ?
Moiety formula   C24 H20 Fe4 S8, 2(C16 H36  ?
                 N)
Sum formula      C56 H92 Fe4 N2 S8          C56 H92 Fe4 N2 S8
Mr               1273.28                    1273.20
Dx,g cm-3        1.374                      1.374
Z                16                         16
Mu (mm-1)        1.232                      1.232
F000             10784.0                    10784.0
F000'            10823.90
h,k,lmax         49,41,30                   49,41,30
Nref             30873                      30717
Tmin,Tmax        0.673,0.831                0.687,0.837
Tmin'            0.659

Correction method= ?

Data completeness= 0.995          Theta(max)= 28.380

R(reflections)= 0.1072( 26739)    wR2(reflections)= 0.2349( 30717)

S = 1.198                 Npar= 1845
```

Alert level A

```
PLAT122_ALERT_1_A No _symmetry_space_group_name_H-M Given .....          ? Do !
PLAT213_ALERT_2_A Atom C89           has ADP max/min Ratio .....        6.2 prola
PLAT411_ALERT_2_A Short Inter H...H Contact  H4A    ..  H55B   ..     1.62 Ang.
PLAT411_ALERT_2_A Short Inter H...H Contact  H10A   ..  H61A   ..     1.51 Ang.
PLAT411_ALERT_2_A Short Inter H...H Contact  H16A   ..  H57A   ..     1.65 Ang.
PLAT411_ALERT_2_A Short Inter H...H Contact  H70A   ..  H44A   ..     1.79 Ang.
PLAT411_ALERT_2_A Short Inter H...H Contact  H57A   ..  H16B   ..     1.77 Ang.
PLAT411_ALERT_2_A Short Inter H...H Contact  H10F   ..  H34A   ..     1.76 Ang.
PLAT411_ALERT_2_A Short Inter H...H Contact  H10W   ..  H40A   ..     1.77 Ang.
PLAT413_ALERT_2_A Short Inter XH3 .. XHn     H10U   ..  H60A   ..     1.87 Ang.
PLAT413_ALERT_2_A Short Inter XH3 .. XHn     H10U   ..  H60C   ..     1.18 Ang.
PLAT413_ALERT_2_A Short Inter XH3 .. XHn     H10V   ..  H60A   ..     1.76 Ang.
```

Alert level B

```
PLAT057_ALERT_3_B Correction for Absorption Required   RT(exp) ...     1.24
PLAT411_ALERT_2_B Short Inter H...H Contact  H10S   ..  H46B   ..     1.89 Ang.
PLAT411_ALERT_2_B Short Inter H...H Contact  H10W   ..  H40B   ..     1.94 Ang.
PLAT411_ALERT_2_B Short Inter H...H Contact  H11B   ..  H40A   ..     1.86 Ang.
PLAT413_ALERT_2_B Short Inter XH3 .. XHn     H5A    ..  H56A   ..     2.04 Ang.
PLAT413_ALERT_2_B Short Inter XH3 .. XHn     H10B   ..  H28A   ..     1.93 Ang.
PLAT413_ALERT_2_B Short Inter XH3 .. XHn     H10U   ..  H60B   ..     2.02 Ang.
PLAT413_ALERT_2_B Short Inter XH3 .. XHn     H11D   ..  H52B   ..     1.92 Ang.
PLAT413_ALERT_2_B Short Inter XH3 .. XHn     H11F   ..  H40B   ..     1.99 Ang.
PLAT413_ALERT_2_B Short Inter XH3 .. XHn     H11G   ..  H87B   ..     2.01 Ang.
```

Figure 4.11. Excerpt of the checkcif file for the structure of $(Bu_4N)_2[Fe_4S_4(SPy)_4]$.

Structural Details and Comparisons. Both the 4-pyridinethiolate single cubane and the sulfide-bridged double cubane afforded single crystals for structure

determination. In each crystal structure the [4Fe-4S] cores are conserved with geometries typical for tetrahedrally distorted iron centers of iron-sulfur cubanes with D_{3d} symmetry. Internal and external Fe-S bond lengths of the $[Fe_4S_4(SR)_x]^{2-}$ anions are on average in the 2.2-2.4 Å range with more obtuse S-Fe-S angles and more acute Fe-S-Fe angles in the $[Fe_4S_4]$ cores as is expected for typical tetra-thiolate ligated [4Fe-4S] cubane clusters. At this time single crystals for structural determination have not been collected for our $(Bu_4N)_2[Fe_4S_4(SMePy)_4]$ cubane; however, a structure was recently published for the analogous cluster with *meta*-$PyMeS^-$ ligands.[12]

The single cubane, $(Bu_4N)_2[Fe_4S_4(SPy)_4]$, crystallizes as black cubic crystals with two unique clusters and four unique tetrabutylammonium counter-ions in the monoclinic C2/c unit cell. Unfortunately, this structure is inherently disordered, and hence, could not be refined satisfactorily. This structure should therefore be considered a preliminary, although the fit for the cluster anion itself is of high quality (see the statement on the structural determination of $(Bu_4N)_2[Fe_4S_4(SPy)_4]$ and Figure 4.11 above). The crystal packing shows two alternating layers: the first one is comprised of three unique counter-ions, which are spread out laterally within the layer, and the second one contains the [4Fe-4S] clusters and one unique counter-ion oriented orthogonally to those in the counter-ion layer (Figure 4.12). The ORTEP structure plotted with 50% thermal ellipsoids of the cluster anions is shown in Figure 4.13 with disordered atoms, hydrogen atoms and counter-ions omitted for clarity. Each one of the pyridinethiolate ligands has a second position as defined in the structure in Figure 4.14.

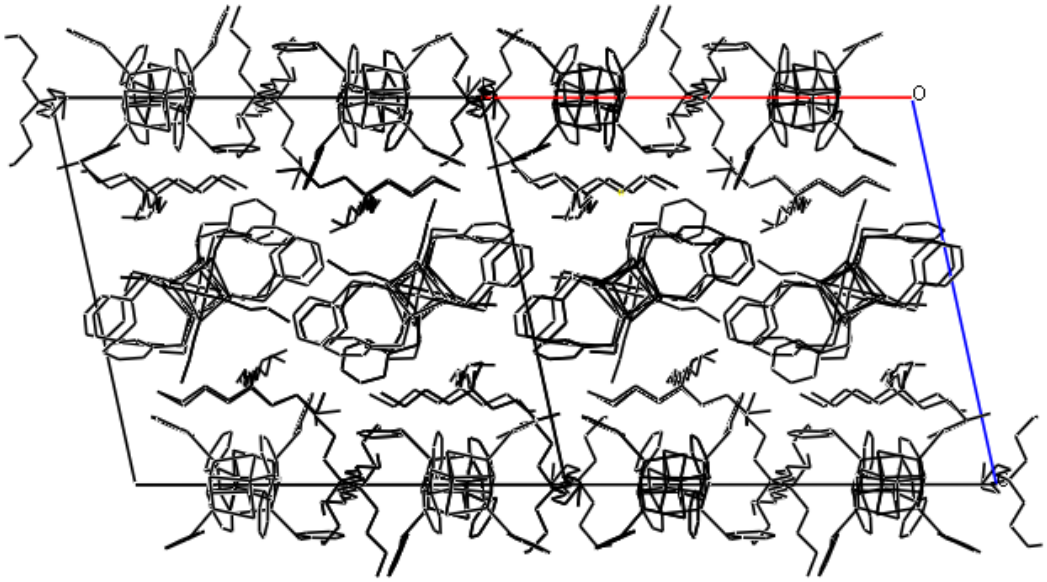

Figure 4.12. Wireframe crystal packing of $(Bu_4N)_2[Fe_4S_4(SPy)_4]$ (hydrogen atoms and disordered ligands are omitted for clarity).

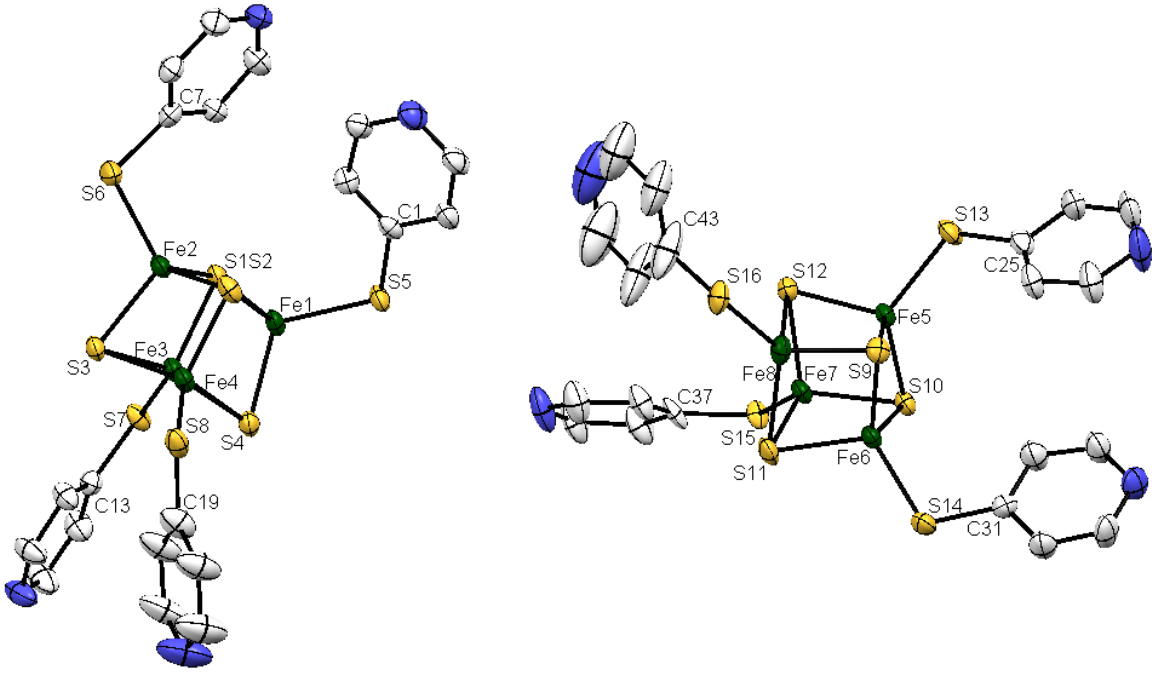

Figure 4.13. ORTEP diagram of $(Bu_4N)_2[(Fe_4S_4(SPy)_4]$ with disordered pyridinethiolate ligands, hydrogen atoms and $(Bu_4N)^+$ counter ions omitted for clarity. Structural parameters are listed in Figure 4.11.

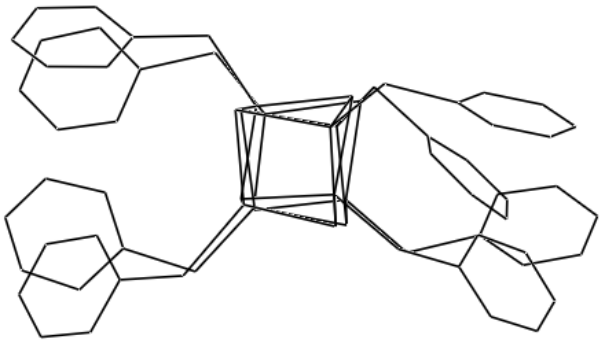

Figure 4.14. Wireframe overlay of the two symmetry unique anions in the crystal structure of $(Bu_4N)_2[Fe_4S_4(SPy)_4]$ (hydrogen atoms, disordered ligands, and counter-ions are omitted for clarity).

The structure of $(Bu_4N)_2[Fe_4S_4(SPy)_4]$ is not at all an exception for a $[Fe_4S_4(SR)_4]^{2-}$ cubane cluster structure. With typical average bond lengths and core bond angles, the only significant differences in structure in comparison to the well-known iron-sulfur cubane $[Fe_4S_4(SPh)_4]^{2-}$ with the same tetrabutylammonium counter ion lie in the rotation of the exogenous thiolate ligands (Figure 4.15).[13] These ligands are free to rotate and bend as is observed for the two separate cluster ions in the unit cell of $(Bu_4N)_2[Fe_4S_4(SPy)_4]$, but overall, the phenyl residues of the ligands are oriented in a way that two ligands reach in the same direction and the other two point the opposite way (see Figure 4.15). The obvious difference in the crystal packing between $(Bu_4N)_2[Fe_4S_4(SPh)_4]$ and $(Bu_4N)_2[Fe_4S_4(SPy)_4]$ is that the phenylthiolate cluster all stack the same way in the solid state, whereas the pyridinethiolate cluster are rotated with respect to each other.

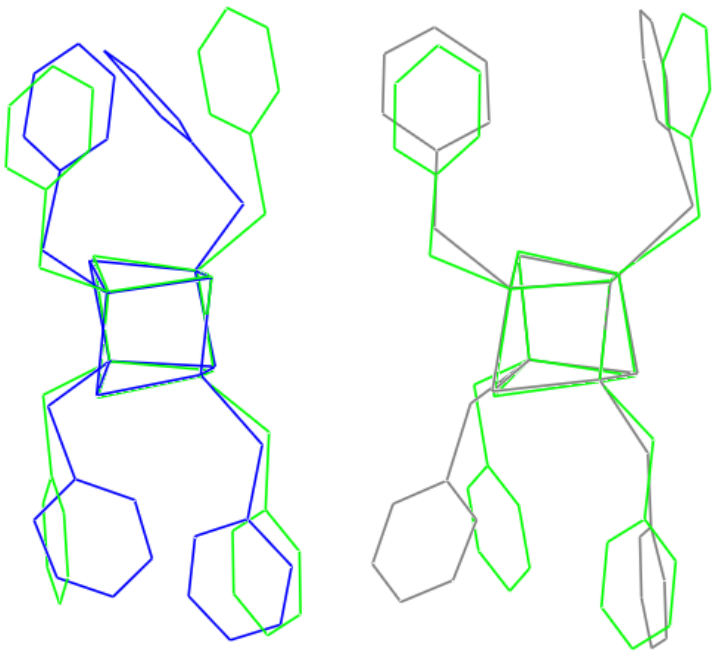

Figure 4.15. Wireframe overlay of the two equivalent anions of $[Fe_4S_4(SPy)_4]^{2-}$ in the structure (blue, grey) and $[Fe_4S_4(SPh)_4]^{2-}$ (green) with counter ions and hydrogen atoms omitted for clarity.

The sulfide-bridged double cubane crystallizes as wide, black needles. The monoclinic P2(1)/n unit cell of $(Bu_4N)_4[(Fe_4S_4(SPy)_3)_2S]$ contains one unique complex with four unique counter ions (Figure 4.16). The ORTEP structure with 50% thermal ellipsoids of the cluster anions is shown in Figure 4.17. Here, disordered atoms, hydrogen atoms and counter-ions are omitted for clarity. Remarkably, very little disorder is found in this structure. Of the six pyridinethiolate ligands only two have more than one orientation, and in addition, the tetrabutylammonium counter-ions that are notorious for having disordered crystal packing are also well ordered in this structure. The usual orientation of the pyrdinethiolate or phenyl groups in the single $[Fe_4S_4(SR)_4]^{2-}$ clusters is also observed here for each cubane. The only exception of this is found for the Fe4-S5-Fe5 sulfide bridge, see Figure 4.17. Here, for the cubane containing Fe4, the Fe4-S5-Fe5

bond angle and position is in the proper “down” position as the aromatic group would be. However, for the cubane containing Fe5, the Fe5-S5-Fe4 bond angle and position is rotated ~180° from the expected position so that the Fe4 cubane “ligand” is in a “down” position when it would be expected to be in an “up” position. Steric crowding of the pyridine rings likely enforces this orientation: as seen in Figure 4.17, the pyridinethiolate ligand with (S12, C11) is pinched between the ligands with (S13, C16) and (S15, C26), opposite the bridging sulfide atom at the center of the double cubane, which likely locks this orientation in place in the solid state. Despite these structural peculiarities in the solid state, it seems that all pyrdinethiolate ligands are equivalent in solution, as seen by ^{1}H-NMR spectroscopy at room temperature, which shows one broad signal for each the *meta*- and *ortho*-hydrogens of the pyridinethiolate rings at 9.15 and 5.13 ppm, respectively (Figure 4.5).

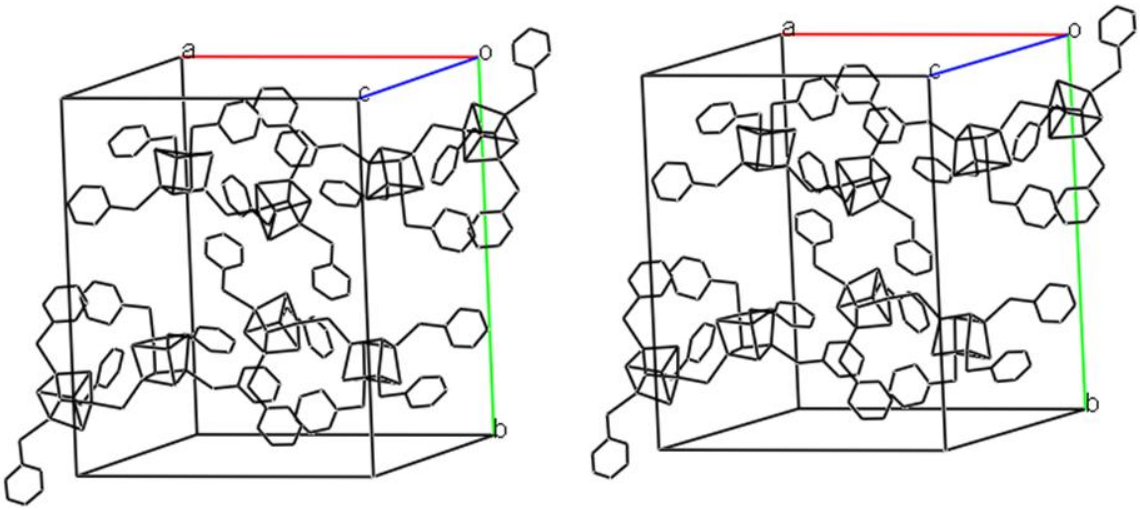

Figure 4.16. Wireframe stereo view of the crystal packing of $(Bu_4N)_4[(Fe_4S_4(SPy)_3)_2S]$ with hydrogen atoms, disordered ligands, and counter-ions omitted for clarity.

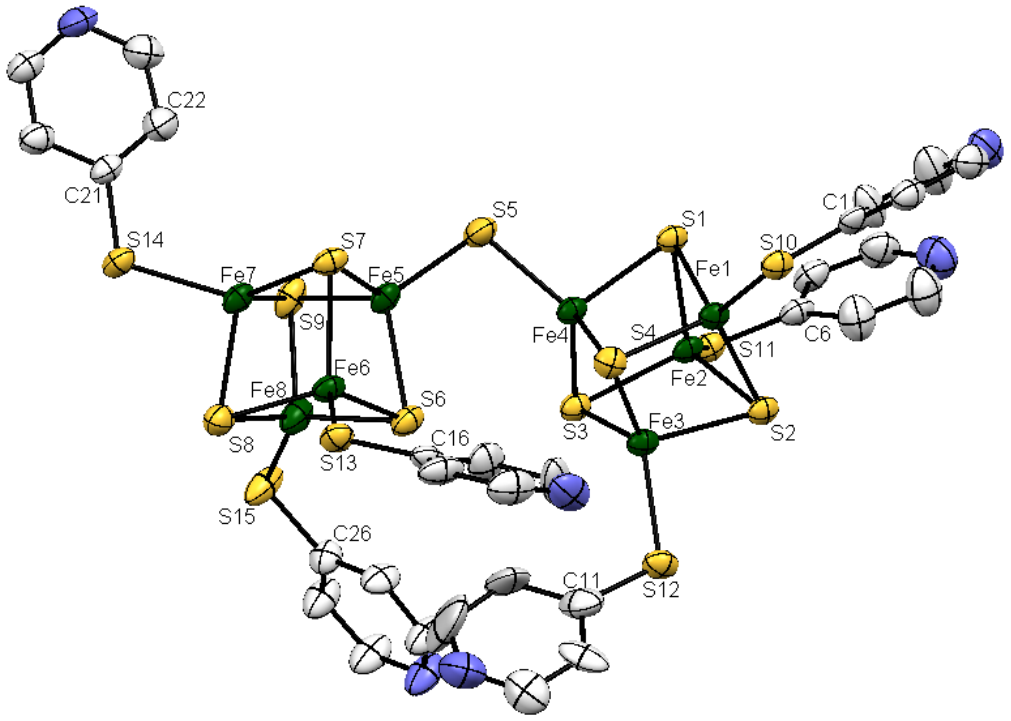

Figure 4.17. ORTEP diagram of $(Bu_4N)_4[(Fe_4S_4(SPy)_3)_2S]$ with disordered S15 and S12 pyridinethiolate ligands, hydrogen atoms and $(Bu_4N)^+$ counter ions omitted for clarity. Structural parameters are listed in Table 4.1.

Comparison of the bridging Fe-S and exogenous Fe-S/Cl bond lengths between $(Bu_4N)_4[(Fe_4S_4(SPy)_3)_2S]$ and the previously published sulfide-bridged double cubane clusters, described in the Introduction section 4.1, are highlighted in Table 4.1. These data indicate that a lengthening or shortening of typical Fe-S and Fe-Cl bonds is not observed for the exogenous ligands of the sulfide-bridged double cubane clusters. However, the bond angles show some differences between the four sulfide-bridged clusters. Whereas $(Ph_4P)_4[(Fe_4S_4(TefpS_3))_2S]$ has a nearly linear Fe-S-Fe bridge, $(Bu_4N)_4[(Fe_4S_4(SPy)_3)_2S]$, $(Bu_4N)_2(Ph_4P)_2[(Fe_4S_4Cl_3)_2S]$, and $(Ph_4P)_4[(Fe_4S_4$-$(TempS_3))_2S]$ display close to ideal tetrahedral bond angles for the bridging sulfide. Although Challen's complex, $(Bu_4N)_2(Ph_4P)_2[(Fe_4S_4Cl_3)_2S]$, has the smallest bond angle, which may be caused by the effect of the polar chloride exogenous ligands on the iron-

sulfur core, the steric bulk of this series of complexes is not equivalent nor is the crystal packing, so one has to be careful in interpreting small differences in Fe-S-Fe angles. In addition, the double cubane $(Ph_4P)_4[(Fe_4S_4(TefpS_3))_2S]$ with the linear bridge shows disorder in the bridging sulfide, which further complicates accurate interpretation of the Fe-S-Fe bridging angle in this compound.

Table 4.2. Selected structural parameters of sulfide-bridged double cubanes.

FeS cluster	Fe-S-Fe angle (bridge) [°]	Fe-S bond length (bridging) [Å]	Fe-S(Cl) bond length (exogenous) [Å][a]	ref.
$(Bu_4N)_4[(Fe_4S_4(SPy)_3)_2S]$	104.02	2.200	2.290	this work
$(Bu_4N)_2(Ph_4P)_2[(Fe_4S_4Cl_3)_2S]$	102.10	2.203	2.223	[6b]
$(Ph_4P)_4[(Fe_4S_4(TempS_3))_2S]$	109.66	2.213	2.267	[6d]
$(Ph_4P)_4[(Fe_4S_4(TefpS_3))_2S]$	161.72	2.143	2.267	[6d]

[a] average

A stereoview of the overlaid core structures of complexes $(Bu_4N)_4[(Fe_4S_4(SPy)_3)_2S]$, $(Bu_4N)_2(Ph_4P)_2[(Fe_4S_4Cl_3)_2S]$, and $(Ph_4P)_4[(Fe_4S_4(TempS_3))_2S]$ is shown in Figure 4.18, which illustrates the "rotation" of the second [4Fe-4S] core relative to the first which is held stationary.[6b, 6d] Figure 4.19 presents all of the sulfide-bridged double cubanes (see Table 4.2). Here, the atoms of the Fe-S-Fe bridge are located in the plane of the paper such that the symmetry of each one of the complexes is highlighted. $[(Fe_4S_4(SPy)_3)_2S]^{4-}$, shown in Figure 4.19, exhibits no rotational symmetry or mirror plane connecting the two iron-sulfur cores. However, a near perfect mirror plane defined by the atoms of the bridge exists for this double cubane. Both clusters $[(Fe_4S_4Cl_3)_2S]^{4-}$ and $[(Fe_4S_4(TempS_3))_2S]^{4-}$ contain a C_2 rotation axis

passing vertically through the bridging sulfide, which connects the iron-sulfur cores that are slightly twisted in opposite directions from the plane defined by the three bridging atoms. Lastly, the complex $[(Fe_4S_4(TefpS_3))_2S]^{4-}$ is the most symmetrical sulfide-bridged double cubane with an inversion center that includes the entire encapsulating ligand $TefpS_3$.

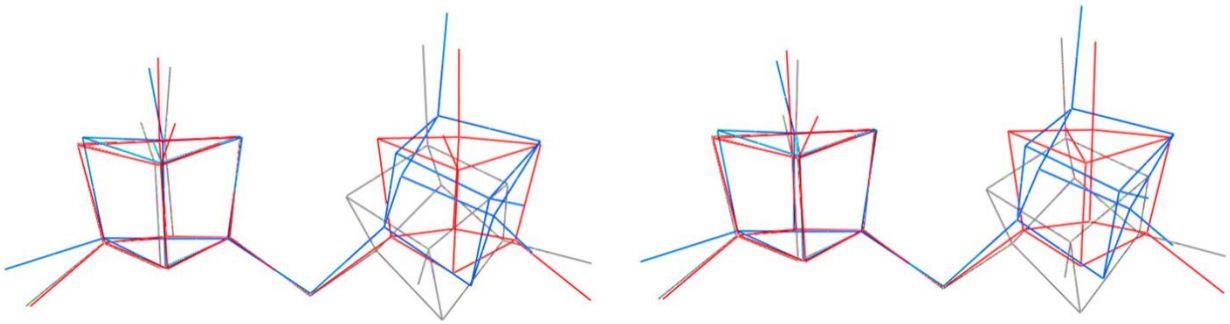

Figure 4.18. Stereo view of the wire frame overlay of $[(Fe_4S_4(SPy)_3)_2S]^{4-}$ (blue), $[(Fe_4S_4(Cl)_3)_2S]^{4-}$ (grey), and $[(Fe_4S_4(TempS_3)_2S]^{4-}$ (red) with counter ions, aromatic rings and solvent molecules omitted for clarity.

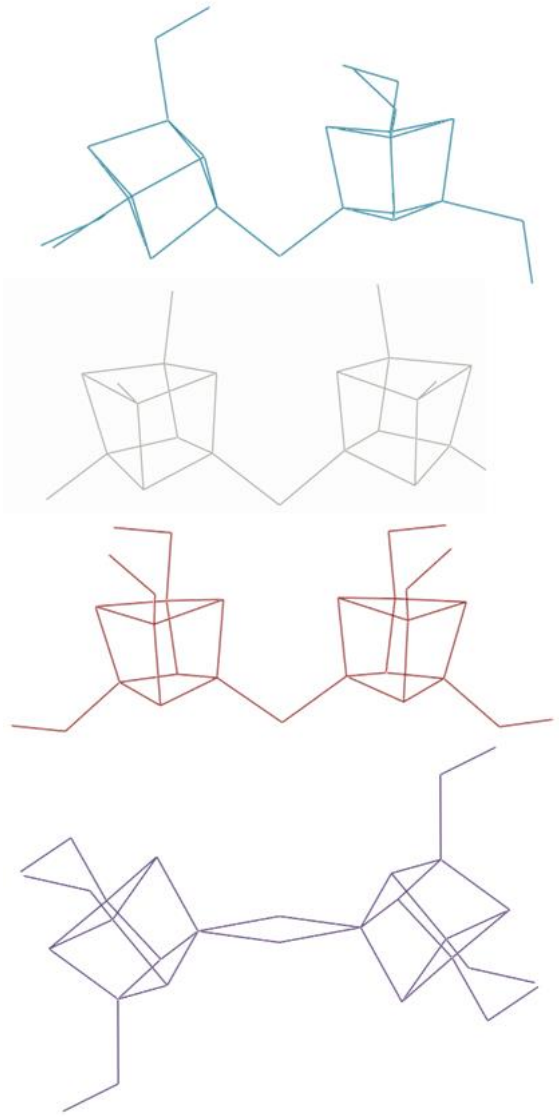

Figure 4.19. Wire frame side view highlighting the sulfide-bridge angles of $[(Fe_4S_4(SPy)_3)_2S]^{4-}$ (top, blue), $[(Fe_4S_4(Cl)_3)_2S]^{4-}$ (second, grey), $[(Fe_4S_4(TempS_3)_2S]^{4-}$ (third, red), and $[(Fe_4S_4(TefpS_3)_2S]^{4-}$ (last, purple) with disordered ligand atoms, counter ions, aromatic rings and solvent molecules omitted for clarity.

4.5 Electrochemistry of Pyridinethiolate Clusters

All of the unique pyridinethiolate ligated clusters synthesized here have irreversible oxidation events occurring at potentials of E_{pa} ~400 to 500 mV vs NHE. The single cubane cluster $(Bu_4N)_2[(Fe_4S_4(SPy)_4]$ has one observable reduction event at $E_{½}$

= -401 mV vs. NHE whereas the $(Bu_4N)_2[(Fe_4S_4(SMePy)_4]$ cluster has two observable reductions at $E_{½}$ = -742 and -1459 mV (Figures 4.21 and 4.20). All of these reduction events for the single cubane clusters are nearly reversible.

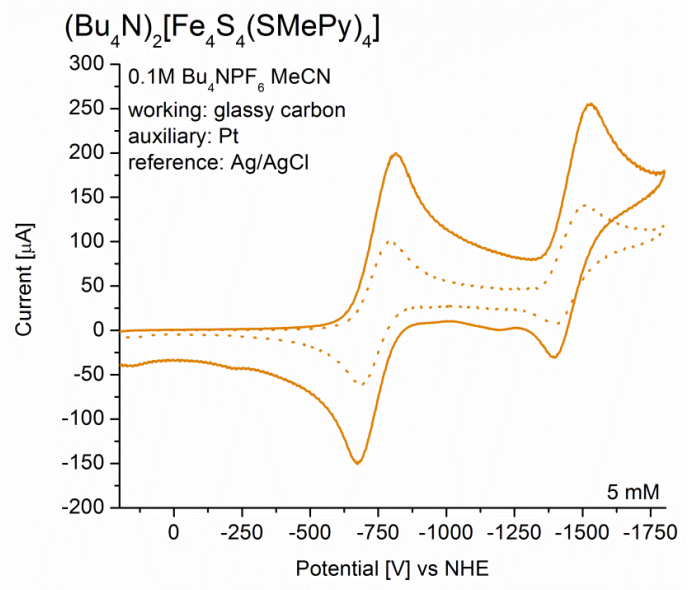

Figure 4.20. Cyclovoltammetry of $(Bu_4N)_2[Fe_4S_4(SMePy)_4]$ in MeCN at scan rates: 200 mV/s (solid) and 50 mV/s (dotted).

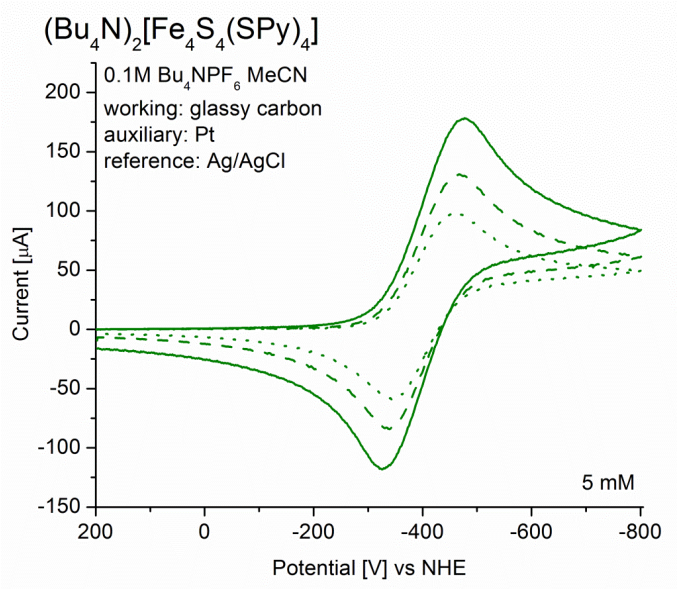

Figure 4.21. Cyclovoltammetry of $(Bu_4N)_2[Fe_4S_4(SPy)_4]$ in MeCN at scan rates: 200 mV/s (solid), 100 mV/s (dashed), and 50 mV/s (dotted).

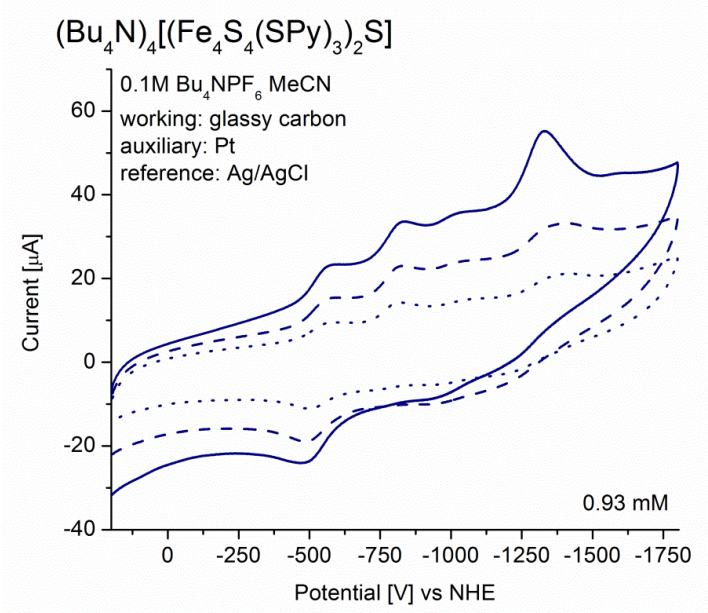

Figure 4.22. Cyclovoltammetry of $(Bu_4N)_4[(Fe_4S_4(SPy)_3)_2S]$ in MeCN at scan rates: 200 mV/s (solid), 100 mV/s (dashed), and 50 mV/s (dotted).

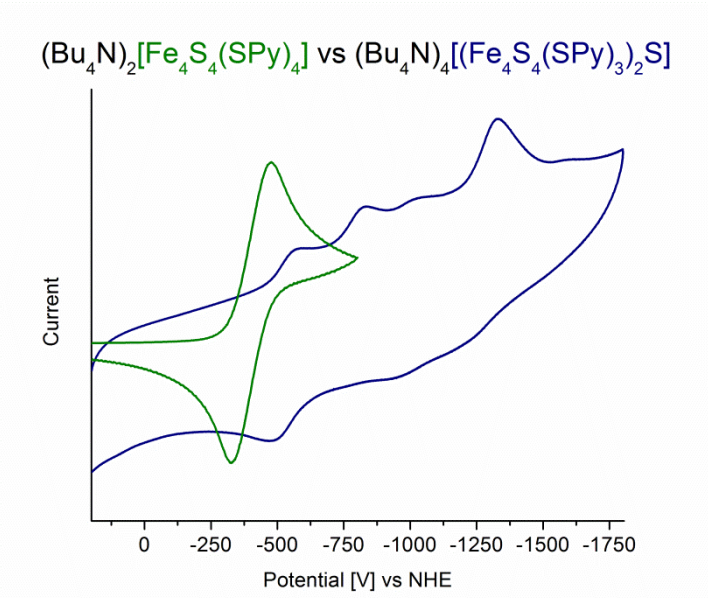

Figure 4.23. Cyclovoltammograms of $(Bu_4N)_2[Fe_4S_4(SPy)_4]$ (green) and $(Bu_4N)_4[(Fe_4S_4(SPy)_3)_2S]$ (blue) in MeCN.

In comparison to literature values for analogous single iron-sulfur clusters (see Table 4.3), the same trend is observed for clusters with other aromatic thiolate ligands. When converting from the short chain ethylthiolate ligand of $(Bu_4N)_2[Fe_4S_4(SEt)_4]$ to

aromatic thiolates, the reduction potentials generally shift distinctively more positive from -1076 mV vs. NHE for the ethylthiolate cluster. This is expected since phenylthiolates are weaker donors than alkylthiolates. This effect is less pronounced for benzylthiolates; for example, the benzyl clusters $(Bu_4N)_2[Fe_4S_4(SBz)_4]$ and $(Bu_4N)_2[Fe_4S_4(SMePy)_4]$ show reduction potentials of -946 mV and -742 mV, respectively, compared to the analogs $(Bu_4N)_2[Fe_4S_4(SPh)_4]$ and $(Bu_4N)_2[Fe_4S_4(SPy)_4]$ with reduction potentials of -756 mV and -401 mV, respectively. This illustrates that benzylthiolates have a somewhat intermediate donicity between alkyl- and phenylthiolates, the pyridine-based thiolates applied here follow this trend well.

The sulfide-bridged double cubane $(Bu_4N)_4[(Fe_4S_4(SPy)_3)_2S]$ has four observable reduction events with distinct E_{pc} signals and merged E_{pa} signals so that only the first reduction event can be quantified as $E_{½}$ = -528 mV (Figure 4.22 and 4.23). Due to the method of hand-collecting crystals of the sulfide-bridged cluster, the concentration of the cluster in the CV experiment was quite low. Nevertheless, the signals in the cyclovoltammogram are significant enough to discern them from the background charge of the electrodes, but are too weak to allow for the identification of the E_{pa} potentials.

Table 4.3. $E_{½}$ reduction potentials of relevant single iron-sulfur clusters vs. NHE [mV] in MeCN.

FeS single clusters	$[Fe_4S_4]^{2+/1+}$	$[Fe_4S_4]^{1+/0}$	ref.
$(Bu_4N)_2[Fe_4S_4(SEt)_4]$	-1076	--	[14]
$(Bu_4N)_2[Fe_4S_4Cl_4]$	-566	--	this work[a]
$(Bu_4N)_2[Fe_4S_4(SPy)_4]$	-401	--	this work
$(Bu_4N)_2[Fe_4S_4(SPh)_4]$	-756	-1486	[14]
$(Bu_4N)_2[Fe_4S_4(SMePy)_4]$	-742	-1459	this work
$(Bu_4N)_2[Fe_4S_4(SBz)_4]$	-946	--	[15]

[a] synthesized from $FeCl_2$, NaSPh, NaOMe, Bu_4NCl in MeCN[11]

Each [4Fe-4S] cluster can undergo two reductions to form the all ferrous cubane cluster; therefore, theoretically, each double cubane cluster should be able to be reduced by four electrons. All of the double cubane clusters compared here are electronically coupled through the sulfide-bridge. This is evident from the multiple one electron reductions observed in the cyclovoltammograms for each double cubane. Rather than each sub-cluster reducing by one electron at the same potential, giving rise to a two electron process, both clusters share the charge by delocalization across both iron-sulfur clusters, leading to a split in potential of the two coupled redox events. The second reduction event is thus at a more negative potential and observed as a distinct process. For both clusters $(Bu_4N)_4[(Fe_4S_4(SPy)_3)_2S]$ and $(Bu_4N)_2(Ph_4P)_2[(Fe_4S_4Cl_3)_2S]$ four one electron reduction processes are identified via their cathodic peaks, whereas the corresponding anodic peaks are ill-defined.[11] Tatsumi's sulfide-bridged clusters have three reduction events reported; unfortunately, a comparison of the reduction potentials to the other cluster is not possible as the potentials are referenced vs. $Ag/AgNO_3$ of unreported concentration.[6d]

The single cluster, $(Bu_4N)_2[Fe_4S_4(SPy)_4]$, is slightly easier to reduce than the sulfide-bridged double cubane $(Bu_4N)_4[(Fe_4S_4(SPy)_3)_2S]$ with reduction potentials of -401 mV and -528 mV, respectively. This order is reversed for the all chloro single and sulfide-bridged double cubane cluster, $(Bu_4N)_2[Fe_4S_4Cl_4]$ and $(Bu_4N)_2(Ph_4P)_2[(Fe_4S_4Cl_3)_2S]$, with reduction potentials of -566 mV and -456 mV, respectively. In the case of the pyrdinethiolate bound single and double cubane clusters the replacement of one thiolate ligand for a sulfide (bound to another [4Fe-4S] cluster) causes the double cluster to be harder to reduce with a more negative reduction potential

indicating that the $^{-}$S-[4Fe-4S] ligand is a stronger donor compared to the pyrdinethiolate. On the other hand, the chloride is the strongest donor in this series, and thus, replacement of one chloride shifts the potential more positive compared to the all-chloro single cubane.

Table 4.4. Reduction potentials of relevant sulfide-bridged iron-sulfur clusters vs. NHE [mV] in MeCN.

Sulfide-bridged FeS clusters	$[(Fe_4S_4)_2S]^n$				ref.
	n = 4+/3+	3+/2+	2+/1+	1+/0	
$(Bu_4N)_4[(Fe_4S_4(SPy)_3)_2S]$	-528	-828 [b]	~ -1050 [b]	~ -1370 [b]	this work
$(Bu_4N)_2(Ph_4P)_2[(Fe_4S_4Cl_3)_2S]$	-456	-776	~ -1156 [b]	--	[6b, 11]
$(Ph_4P)_4[(Fe_4S_4(TempS_3)_2S]$ [a]	(-1660)	(-1870)	(-2310) [b]	--	[6d]
$(Ph_4P)_4[(Fe_4S_4(TefpS_3)_2S]$ [a]	(-1550)	(-1740)	(-2240) [b]	--	[6d]

[a] referenced vs. $Ag/AgNO_3$ of unreported concentration; [b] E_{pc} value due to undefined E_{pa}

4.6 EPR of One Electron Reduced Clusters

Each cubane cluster in the $[Fe_4S_4]^{2+}$ state has two ferric and two ferrous irons; a face of the cubane thus contains a high-spin Fe^{3+} and a high-spin Fe^{2+}, ferromagnetically coupled, for a combined spin of S= $^9/_2$. The two opposite faces of the cubane are anti-ferromagnetically coupled, resulting in the total spin of S = 0.[1b] The pyridinethiolate ligated cubane clusters synthesized here gave no EPR signal in their isolated state in agreement with this. In order to prepare the one-electron reduced cubanes, solutions of the tetrabutylammonium salts of $[(Fe_4S_4(SPy)_4]^{2-}$ and $[(Fe_4S_4(SPy)_3)_2S]^{4-}$ were reduced with sodium acenaphthylene in the presence of Bu_4NBr and subsequently frozen. The resulting reduced clusters $[(Fe_4S_4(SPy)_4]^{3-}$ and $[(Fe_4S_4(SPy)_3)_2S]^{5-}$ each exhibit an EPR signal corresponding to an axial S = ½ ground state, for the unpaired electron spin simply added to the starting S = 0 states (Figure 4.24). The S = ½ EPR signal of the reduced

single cluster $(Bu_4N)_3[(Fe_4S_4(SPy)_4]$ decreases in intensity significantly when the sample is warmed above 8 K with axial g values of $g_x=g_y = 1.928$ and $g_z = 1.724$. It should be noted that $g < 2$ is not uncommon for ferredoxins due to antiferromagnetic coupling of Fe^{2+} and Fe^{3+} as described in the Heisenberg-Dirac-van Vleck Hamiltonian.[1b] In the case of the bridged double cubane the one-electron reduced state corresponds to a mixed-valent compound, but not of two bridged metal centers, which is the usual case, but of two linked clusters: $[Fe_4S_4]^+$–S–$[Fe_4S_4]^{2+}$. The extra electron could be localized on one cluster, oscillate between the clusters, or could be quantum-mechanically delocalized. However, at the same time the extra electron is also delocalized within one cluster. This creates an interesting electronic situation. When warming the sample of the double cubane cluster above 8 K the intensity of the S = ½ signal has an initial decrease then *increases* at ~45 K, and then decreases again as shown in Figure 4.25 and 4.26. The sharp axial EPR signal of $(Bu_4N)_5[(Fe_4S_4(SPy)_3)_2S]$ has g values of $g_x=g_y = 2.0328$ and $g_z = 1.995$ in contrast to the rhombic g values reported by Holm and coworkers for double cubanes bridged by small organic dithiolates.[6a] Over the whole temperature range (Figure 4.25), no broadening of the EPR signal of the sulfide-bridged double cubane is observed, indicating that the electron is likely in a trapped state in one of the clusters, and not fluctuating between the two (at least not at the temperatures used for the EPR measurements). The observed variation in EPR intensity could indicate a population of a low-lying excited state, potentially with the same S = ½ or a larger total spin of S = $^3/_2$ and a different relaxation behavior. In the latter case, large zero-field splitting, such that only the $|M_S> = \pm 1/2$ doublet is thermally populated, could then explain the experimental observations. In this respect, note that an S = $^3/_2$ ground state has been observed for a

number of one-electron reduced single-cubane clusters.[16] Further experiments are required to investigate the interesting properties of the one-electron reduced double cubane in detail.

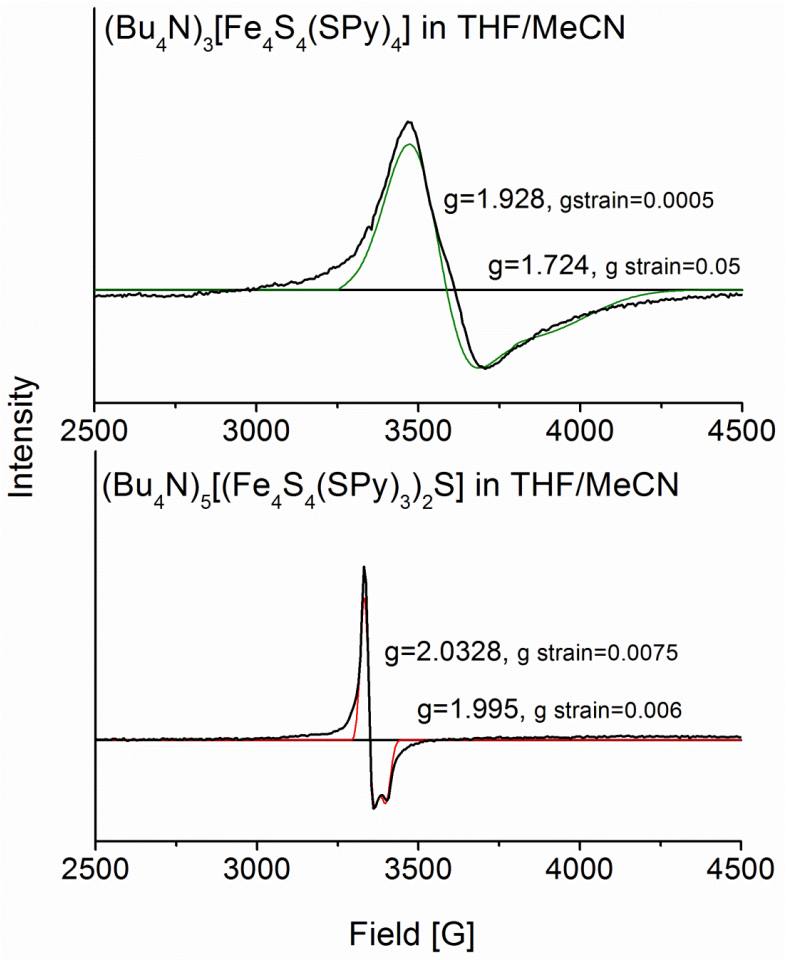

Figure 4.24. EPR spectra of the one-electron reduced clusters $(Bu_4N)_3[Fe_4S_4(SPy)_4]$ (top) and $(Bu_4N)_5[(Fe_4S_4(SPy)_3)_2S]$ (bottom) at 4.3 K. The colored lines are the simulated spectra using the program Spin Count (M. Hendrich, Carnegie Mellon University).

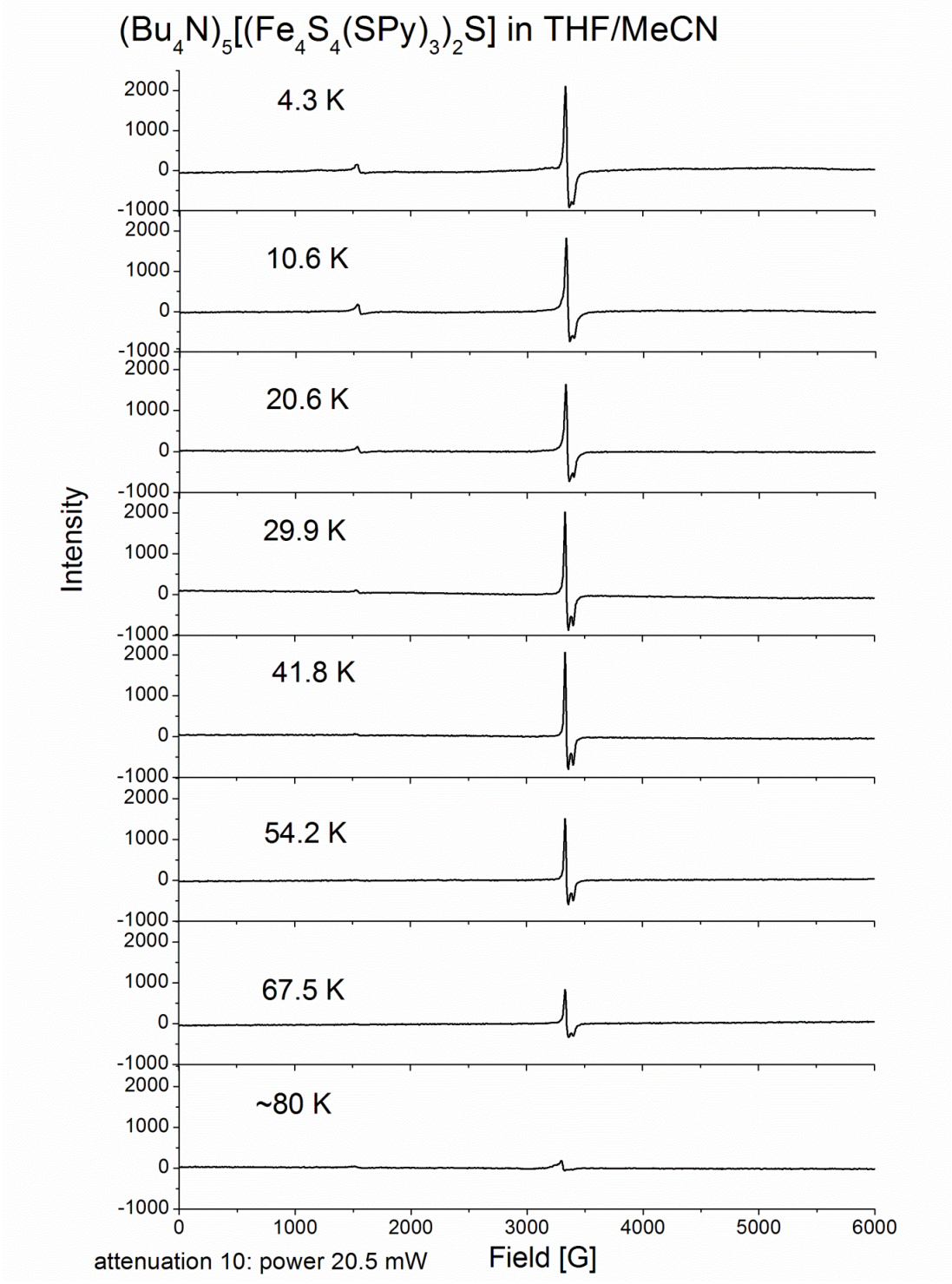

Figure 4.25. EPR spectra for the one electron reduced cluster $(Bu_4N)_5[(Fe_4S_4(SPy)_3)_2S]$ at varying temperatures (see also Figure 4.26).

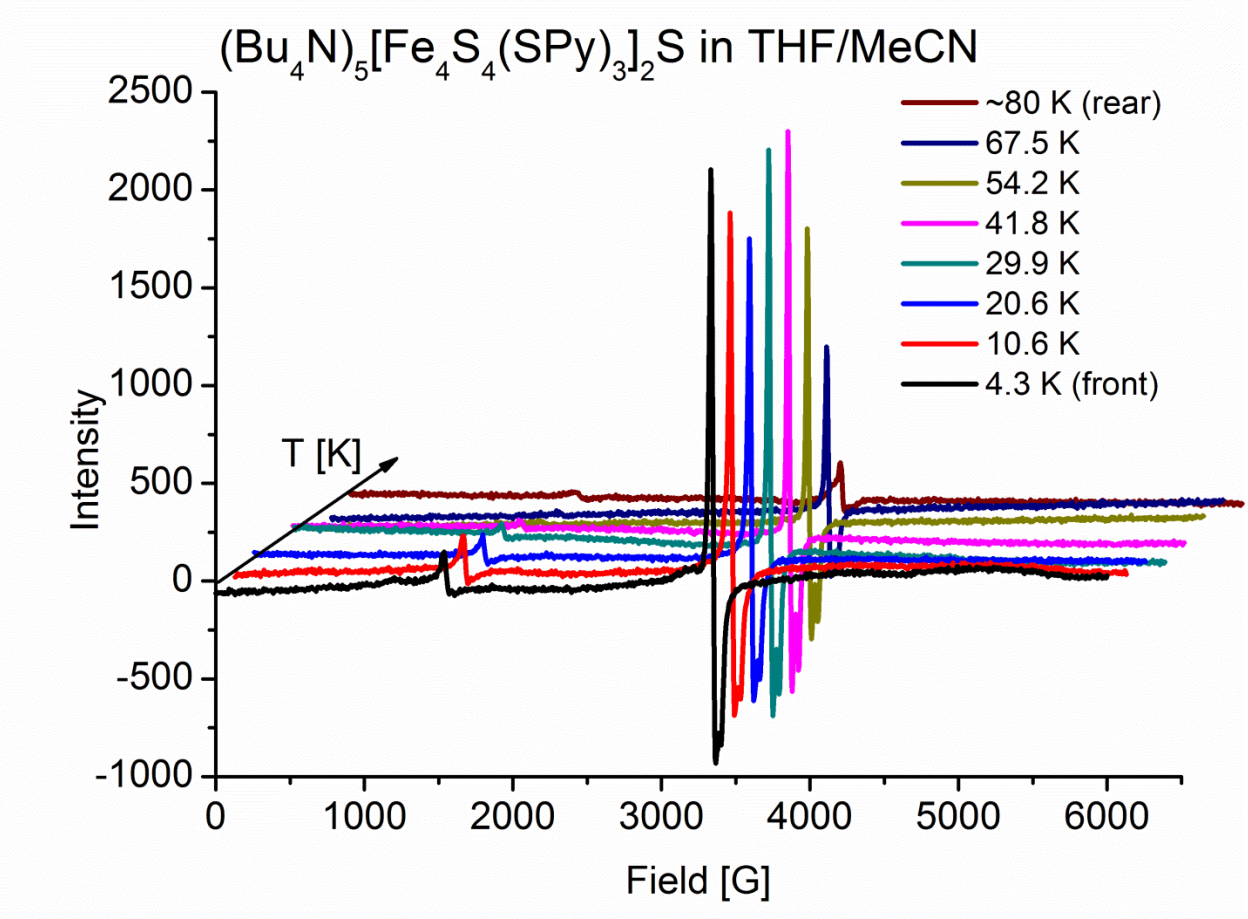

Figure 4.26. EPR spectra for the one electron reduced cluster $(Bu_4N)_5[(Fe_4S_4(SPy)_3)_2S]$ at varying temperatures.

4.7 Crystallization of $(Bu_4N)_3[Fe_4S_4(SPy)_4]$ with La^{3+}, Eu^{3+}, and Gd^{3+}

The tetraligated cluster $(Bu_4N)_3[Fe_4S_4(SPy)_4]$ has the capability of binding to four separate secondary metal centers. Due to the angle of attachment of the -SPy ligands to the cubane cluster it is not possible for multiple pyridinethiolate ligands from one [4Fe-4S] cluster to bind to the same secondary metal center. Thus, by adding a "ligand free" metal cation (a metal salt with anions that are weak bases) to a solution of this cubane, it should be possible to generate extended lattice networks (or metal organic frameworks, MOFs) of redox active [4Fe-4S] centers and cations with the unique

property of electron storage and transfer. The inclusion of lanthanide metals further provides fluorescence properties which could prove to be beneficial for the transfer of electrons through the resulting MOF material.

Stock solutions of a range of concentrations were prepared of $(Bu_4N)_3[Fe_4S_4(SPy)_4]$, $La(NO_3)_3$, $Eu(NO_3)_3$, and $Gd(NO_3)_3$ in DMF or MeCN and combined using various crystallization methods (Figure 4.27). Layering and slow diffusion at room temperature and at -10 °C were attempted repeatedly, utilizing a variety of glassware to increase or decrease the surface area of the stock solutions as they interact or to further distance the two solutions for slower diffusion. The mixtures were allowed to slowly diffuse, and after three months, thin plate crystals were observed in the diffusion reactions for each of the lanthanide ions reacted: La^{3+}, Eu^{3+}, and Gd^{3+}. Once the thin plates were mounted to collect the diffraction data, the crystallographer noted that the plates were so thin that they were bending due to their own weight. Figure 4.28 illustrates a sampling of the diffraction pattern collected for the crystals from the reaction of $(Bu_4N)_3[Fe_4S_4(SPy)_4]$ and $Eu(NO_3)_3$.

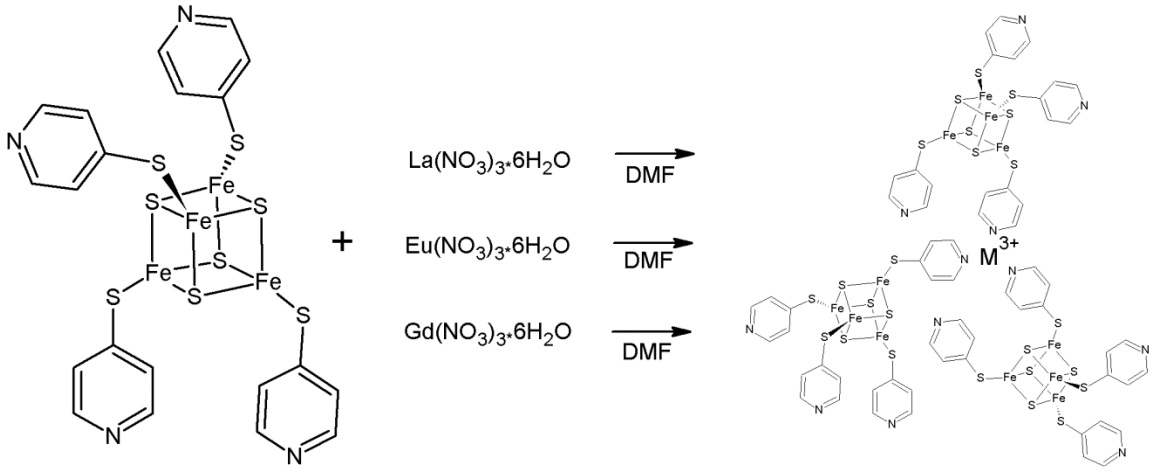

Figure 4.27. Synthetic scheme for the reaction of the single cubane cluster $(Bu_4N)_3[Fe_4S_4(SPy)_4]$ with lanthanide nitrate salts for the production of redox active MOFs.

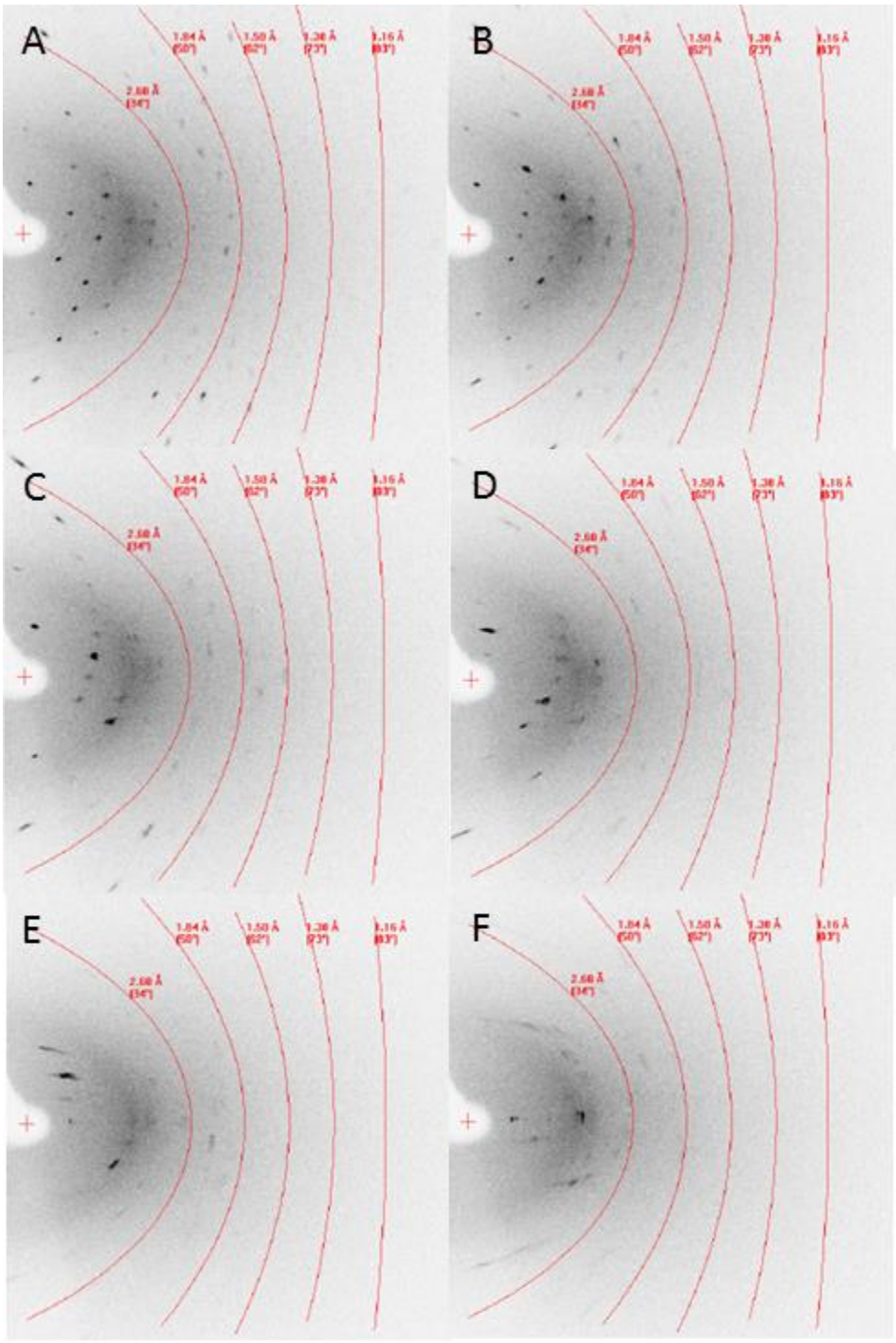

Figure 4.28. The diffraction pattern of a plate crystal taken from the reaction mixture of $Eu(NO_3)_3$ and $(Bu_4N)_2[Fe_4S_4(SPy)_4]$ in DMF representative of all of the screened crystals produced by the lanthanide reactions with $(Bu_4N)_2[Fe_4S_4(SPy)_4]$. Images A through F are the observed diffraction pattern where each image progresses by a 2° rotation of the source.

The extreme thinness of these crystals did not produce viable diffraction data sets as seen in Figure 4.28. A clear diffraction pattern was only observed for a very narrow range of degrees, <10°. As the source moved from that narrow window of diffraction, no diffraction pattern were discernible. Further crystallization attempts to grow larger crystals proved unsuccessful.

It is peculiar that the crystals grown from each of the lanthanide metals all exhibited the same narrow band of diffraction pattern. It is possible that the narrow gap of a clean diffraction pattern is coinciding with the source running through the plane of the thin crystal. The growth of the crystals appears to be primarily in two dimensions which is unexpected given that the single cluster has four flexible ligands capable of binding to the lanthanide metal centers in essentially any orientation, and that lanthanide cations can coordinate with up to eight pyridine ligands. Introduction of additional ligands, such as phenol, salen, or catechol, to satisfy the coordination number of the lanthanide but not exchange ligands of the [4Fe-4S] cluster may be the key to stabilizing lattice growth in three dimensions to produce a MOF that is amendable to structural characterization. Further experimentation is needed.

4.8 Conclusions

The preparation of three new *para*-pyridinethiolate ligated iron-sulfur cubane clusters has been reported here. The single clusters $(Bu_4N)_2[Fe_4S_4(SMePy)_4]$ and $(Bu_4N)_2[Fe_4S_4(SPy)_4]$ are notable additions to the archive of synthetic [4Fe-4S] cubane clusters with similar syntheses and geometric and electronic properties. Most interesting is the isolation of the sulfide-bridged double cubane $(Bu_4N)_4[(Fe_4S_4(SPy)_3)_2S]$ which is

intentionally formed with the addition of sulfide in the cluster synthesis and also through cluster decomposition and equilibrium in solution of the single cluster $(Bu_4N)_2[Fe_4S_4(SPy)_4]$. Because the single cluster $(Bu_4N)_2[Fe_4S_4(SMePy)_4]$ does not readily form sulfide-bridged double cubanes under the same conditions, it can be inferred that the tautomerization of the *para*-pyrdinethiolate ligand likely is the origin of the propensity of the single cluster to lose sulfide in a decomposition pathway, which is somehow stabilized or initiated by the pyridinethiolate ligand. Hence, $(Bu_4N)_4[(Fe_4S_4(SPy)_3)_2S]$ is the first example of a sulfide-bridged all-thiolate ligated cluster that has been structurally characterized in the absence of a large encapsulating ligand. Although the equilibrium of single and double clusters causes the crystallization and isolation of pure complex to be difficult, we succeeded in isolating both species in the form of single crystals, and we were able to determine their crystal structures. The structures of the *para*-pyrdinethiolate ligated single cluster and the sulfide-bridged double cluster show typical internal and external Fe-S bond lengths within 2.2-2.4 Å, and reduction potentials that are more positive than those of the analogous phenylthiolate clusters, yet more negative than the chloro-clusters. The unique spectroscopic features in the ^{1}H-NMR and Far-IR spectra of the single and sulfide-bridged double cubane clusters allow for a simple check for purity of the collected crystalline material. One-electron reduction of the single and double pyridinethiolate clusters $(Bu_4N)_2[Fe_4S_4(SPy)_4]$ and $(Bu_4N)_4[(Fe_4S_4(SPy)_3)_2S]$ both results in the appearance of $g \approx 2$ signals in EPR, indicative of $S = ½$ ground states of these species. Temperature-dependent EPR data of the reduced sulfide-bridged double cubane do not show any broadening of the signal at higher temperature, which suggests that the additional electron is trapped in one of the

clusters in the dimer, and not fluctuating at the experimental temperatures. The temperature dependence of the EPR intensity of this species is quite unusual, and suggests the presence of a low-lying excited state, but this point requires further study.

The added pyridyl groups of the iron sulfur clusters prepared here allow for a wide range of interesting applications for these clusters. In particular, the pyridines are open for coordinating to an external metal center forming an electron bridge.[17] The clusters have essentially reversible redox cycles in which an electron can be transferred through the aromatic pyridinethiolate ligand to or from the external metal center. With the abundance of bridging pyridinethiolate ligands for each cluster, materials with three-dimensional linked structures could possibly be obtained with interesting redox and optical properties, for example conducting solids or materials with non-linear optical properties. Work towards these goals will be pursued in the future.

4.8 References

[1] a) B. A. Averill, T. Herskovitz, R. H. Holm, J. A. Ibers, *J. Am. Chem. Soc.* **1973**, *95*, 3523-3534; b) H. Beinert, R. H. Holm, E. Münck, *Science* **1997**, *277*, 653659.

[2] P. V. Rao, R. H. Holm, *Chem. Rev.* **2004**, *104*, 527-559.

[3] a) W. E. Cleland, D. A. Holtman, M. Sabat, J. A. Ibers, G. C. DeFotis, B. A. Averill, *J. Am. Chem. Soc.* **1983**, *105*, 6021-6031; b) C. Zhou, R. H. Holm, *Inorg. Chem.* **1997**, *36*, 4066-4077.

[4] W. Lo, P. Zhang, C.-C. Ling, S. Huang, R. H. Holm, *Inorg. Chem.* **2012**, *51*, 9883-9892.

[5] a) T. Mochida, M. Ueda, H. Moriyama, *Mol. Cryst. Liq. Cryst.* **2000**, *342*, 91-06; b) M. Ueda, T. Mochida, *Inorg. Chim. Acta* **2003**, *353*, 306-309.

[6] a) T. D. P. Stack, M. J. Carney, R. H. Holm, *J. Am. Chem. Soc.* **1989**, *111*, 1670-1676; b) P. R. Challen, S.-M. Koo, W. R. Dunham, D. Coucouvanis, *J. Am. Chem. Soc.* **1990**, *112*, 2455-2456; c) J. A. Weigel, R. H. Holm, *J. Am. Chem. Soc.* **1991**, *113*, 4184-4191; d) T. Terada, T. Wakimoto, T. Nakamura, K. Hirabayashi, K. Tanaka, J. Li, T. Matsumoto, K. Tatsumi, *Chem. Asian J.* **2012**, *7*, 920-929; e) J. Huang, S. Mukerjee, B. M. Segal, H. Akashi, J. Zhou, R. H. Holm, *J. Am. Chem. Soc.* **1997**, *119*, 8662-8674; f) M. A. Whitener, G. Peng, R. H. Holm, *Inorg. Chem.* **1991**, *30*, 2411-2417.

[7] a) J. H. Barnes, M. Fatome, C. E. L. Jones, S. G. Murray, *Eur. J. Med. Chem.* **1988**, *23*, 211-216; b) D. Mascagna, M. d'Ischia, C. Costantini, G. Prota, *Synthetic Comm.* **1994**, *24*, 35-42.

[8] C. J. A. Daley, R. H. Holm, *J. Inorg. Biochem.* **2003**, *97*, 287-298.

[9] R. A. Jones, A. R. Katritzky, *J. Chem. Soc.* **1958**, 3610-3613.

[10] S. Stoyanov, I. Petkov, L. Antonov, T. Stoyanova, P. Karagiannidis, P. Aslanidis, *Can. J. Chem.* **1990**, *68*, 1482-1489.

[11] P. R. Challen, University of Michigan (Ann Arbor, Michigan), **1990**.

[12] Y. Kim, J. Han, *Bull. Korean Chem. Soc.* **2012**, *33*, 48-54.

[13] a) L. Guodong, Z. Hongtu, H. Sheng-Zhi, T. C. W. Mak, *Acta Cryst.* **1987**, *C43*, 352-353; b) J. Gloux, P. Gloux, H. Hendriks, G. Rius, *J. Am. Chem. Soc.* **1987**, *109*, 3220-3224.

[14] C. Zhou, J. W. Raebiger, B. M. Segal, R. H. Holm, *Inorg. Chim. Acta* **2000**, *300-302*, 892-902.

[15] T. Herskovitz, B. A. Averill, R. H. Holm, J. A. Ibers, W. D. Phillips, J. F. Weiher, *Proc. Natl. Acad. Sci. U. S. A.* **1972**, *69*, 2437-2441.

[16] a) R. Holm, P. Kennepohl, E. I. Solomon, *Chem. Rev.* **1996**, *96*, 2239-2314; b) P. A. Lindahl, E. P. Day, T. A. Kent, W. H. Orme-Johnson, E. Münck, *J. Biol. Chem.* **1985**, *260*, 11160-11173.

[17] D. L. Gerlach, D. Coucouvanis, N. Lehnert, *Eur. J. Inorg. Chem.* **2013**, *(accepted for publication)*.

CHAPTER 5

Conclusions

The primary scope of this thesis was to develop a robust biologically inspired catalyst for multi-electron reduction by utilizing the collective structural and mechanistic knowledge of assimilatory sulfite reductases. The three structural features identified as necessary for the first generation design are (i) a metalloporphyrin, for use as a catalytic site, (ii) a [4Fe-4S] cluster, for use as an electron reservoir, and (iii) a bridging ligand or atom to link the catalytic and electron storage components. Two designs were formulated using different forms of connectivity for the bridging component resulting in a) a more biomimetic axial coordination of an iron-sulfur cluster via a bridging ligand to a heme complex (Chapter 2), and b) a covalent ligation of the iron-sulfur cluster directly to the functionalized porphyrin ligand (Chapter 3). For both designs, a stable link between the catalytic site and the electron reservoir was a key necessity. Insight into the use of various small organic bridging ligands bound first to the [4Fe-4S] cluster led to investigations into the properties of iron-sulfur clusters with functionalized ligands (Chapter 4).

The primary focus of the research presented in Chapter 2, the Axially Bound Model, was to optimize the axial binding of the iron-sulfur cluster to the heme iron via the use of a small organic ligand to achieve strong binding in solution, and in this way, to obtain a single heme-[4Fe4S] complex which could later be tested for the catalytic

reduction of biologically relevant substrates. Preferential binding of the bridging ligand was achieved byincorporating a thiolate anionic site for ligation to the iron-sulfur cluster and a neutral σ-donor N-heterocycle, in particular imidazole and pyridine, for coordination to the heme iron at the axial coordination site. To aid in the binding of only one cluster per heme macrocycle, the use of a site-differentiating ligand ($TriS^{3-}$) was employed for the [4Fe-4S] cluster. This ligand was first reported by Pohl and coworkers.[1] The site-differentiating ligand not only limits the number of bridging ligands to one at the iron-sulfur cluster but also helps to protect the iron-sulfur cluster from decomposition by ligand loss, using the chelating effect. The addition of electron withdrawing fluorine substituents to the peripheral groups of the porphyrin was utilized to reduce the electron density at the heme iron and in turn increased the binding affinity for an axial ligand. In contrast to previous reports by Holm and coworkers, who aimed to model the active site of aSIR by using a sulfide bridge to link an isobacteriochlorin to a site-differentiated iron-sulfur cubane cluster, our model design is highly flexible as each component can be adjusted as desired. This also bypasses the instability of an anionic ligand as a bridge to the heme iron, especially in the ferrous state of the heme.[2] The enzyme aSIR can readily use a sulfide bridge due to the ensured structural immobility and stability provided by the protein matrix. Our model design is meant to operate in solution for the purpose of reducing a variety of substrates, thus the primary achievement of my work is the determination of the synthetic and structural strengths and weaknesses of the model design and the chosen components, and their optimization to achieve optimal binding in solution, which would yield a viable catalytic array. The significant findings include the following: 1) the [4Fe-4S] cluster must be protected by an

encapsulating ligand to minimize exogenous ligand exchange or extended lattice growth, 2) the use of a bridging ligand which entails a thiolate and an N-heterocycle allows for the preferential binding of the [4Fe-4S] cluster component to the thiolate and the metalloporphyrin to the N-heterocycle, 3) inclusion of a flexible chain between the thiolate and the N-heterocycle of the bridging ligand may allow for increased binding to the metalloporphyrin, 4) additional electron withdrawing substituents in the periphery of the porphyrin ligand both increase the binding affinity of the N-heterocycle to the metalloporphyrin and aid in the fine tuning of the reduction potential of the ferric/ferrous couple of the heme.

It should be noted that even with my best system that optimizes the binding of the components to obtain a robust single molecule complex for catalytic testing, the equilibrium for the binding and dissociation of the N-heterocycle to the heme will always result in a fraction of free heme and free [4Fe-4S] cluster in solution. To further stabilize a model complex within this design, additional synthetic modifications need to be made to the porphyrin ligand to include at least one tether to the N-heterocycle. Thus the axial ligand would be anchored in the binding pocket of the heme. Addition of an appropriate thiolate group would allow for the covalent bond to the [4Fe-4S] cluster. Further modification could be devised that would tether the porphyrin directly to the encapsulating ligand of the [4Fe-4S] cluster. These modifications are not trivial and will require the establishment of the corresponding synthetic methods, and this would certainly constitute a significant challenge to the synthetic chemist.

As a synthetically less challenging alternative to the axial bound design, Chapter 3 reports the advancement of the Covalently Bound Model where the attachment of the

catalytic site and electron reservoir diverges from the biologically relevant axial coordination by instead covalently linking the heme and the iron-sulfur cluster. To achieve this goal the porphyrin macrocycle was modified to include a functional group so that the porphyrin itself is the ligand for the iron-sulfur cluster. The basic components of the aSIR active site are retained with the potential for electron transfer to proceed from the iron-sulfur cluster to the heme iron where substrate binding is to occur during catalytic turn over. It was shown that the functionalized porphyrin ligand does ligate to the [4Fe-4S] cluster. Our covalently bound model is at its early stage of development and will therefore require more efforts to minimize solvent and oxygen interference. The key benefit of the covalent model is the versatility of the heme porphyrin ligand which allows easy modification for later improvement as needed once the system is tested for substrate reduction. The only feature of the porphyrin ligand that must remain unchanged is the availability of a functional group, such as an alcohol or thiol group, for the binding of the [4Fe-4S] cluster.

Further efforts to obtain a robustly linked complex for multi-electron reduction of substrates would best be investigated into modifying the current synthesized complex of the covalently bound model presented here. As in the case of the axially bound model design, the heme porphyrin and the iron-sulfur cluster are modifiable to tune the electron density of the catalytic site by introducing peripheral substituents to adjust the redox potential. For the covalently bound model, an additional ligand for the heme can be introduced as desired to add additional stability or fine tune the electronic state of the heme iron for optimal reduction of substrate. The important difference for the covalently bound model vs. the axially bound model is that the axial ligand can be labile and bind as

needed throughout the catalytic cycle of the complex. This model can also be expanded to incorporate multiple electron reservoir sites per each catalytic site by binding multiple iron-sulfur clusters to a multi-functionalized heme porphyrin.

The early stages of development of the axially bound model lead to the investigation of the properties of iron-sulfur clusters with multi-functionalized ligands and the unexpected structural determination of a singly sulfide-bridged double cubane as reported in Chapter 4, Bridging [4Fe-4S] Pyridinethiolato Ligated Clusters. Prior to utilization of the encapsulating $TriS^{3-}$ ligand, tetra ligated iron-sulfur clusters were tested for binding, and not surprisingly, found to bind to multiple metalloporphyrins thus forming larger complexes and oligomers. Although the potential of the multi-functionalized iron-sulfur clusters were not optimal for isolation of a single molecule catalytic complex, the redox properties and the ability for coordination to secondary metal sites are a potential use for these clusters. Intentional growth of extended lattice systems with lanthanide and transition metals were attempted with evidence for the potential crystallization of such extended lattices. Interestingly, the propensity of the 4-pyridylthiolate ligand for tautomerization induces a lability of sulfide in a solution of the iron-sulfur clusters and generates the singly sulfide-bridged double cubane with pyridylthiolate ligands. Only three other crystal structures have been reported for singly sulfide-bridged clusters by Challen and Matsumoto and coworkers, but this is the first all-thiolate bound cluster that was structurally characterized in the absence of an encapsulating ligand.[3] Investigations into the ability of the one-electron reduced bridged clusters to electronically couple aid in the understanding of the capability of the iron-

sulfur cluster to readily share electrons to a secondary redox site as is seen in three enzymes: sulfite reductase, [Fe-Fe] hydrogenase, and acetyl CoA synthase.[4]

Hemes and iron-sulfur clusters have successfully been exploited and are widely used for enzymatic activity in biology and our understanding of their function and properties expands every day. With the advancement of bioinorganic and bioorganometallic research, enzyme cofactors such as the robust heme have gained more and more popularity for use as industrial catalysts and drugs and further research is expanding this area continuously. Alternatively, although robust *in vivo*, iron-sulfur clusters are sensitive to oxidation, strong acids, and strong Lewis acids. Knowing this limitation, our catalyst designs, which use iron-sulfur clusters as an electron source, can likely not be used for industrial applications. However, understanding how two very different, linked redox active sites transfer electrons from one (a [4Fe-4S] cluster) to the other (a heme iron) is valuable for understanding electron transfer and mechanism of aSIR.

In conclusion of and thesis work, two viable biologically inspired catalyst designs have been presented with their applicability to model aSIR has been tested. This work provides the proof of concept that both the axially and covalently coordinated models can be obtained, and the properties of the individual components of these designs have been optimized for electron transfer from the [4Fe-4S] electron reservoir to the heme catalytic site. The axially bound complex design is the more biomimetic system, and it has the advantage of increased stability due to the N-heterocycle used as an axial bridging ligand compared to the sulfide bridged system prepared by Holm and coworkers.[2] In addition, my work has shown that the hemes with more electron withdrawing substituents have the

highest binding constants with the imidazylthiolate bound [4Fe-4S] cluster. Using this system in connection with a ferrous heme, it can be expected that substrate binding and activation can be studied with this model, which is a distinct step forward compared to Holm's model. However, a disadvantage of this design is that only two electrons can be stored, and hence, a complete reduction of sulfite to sulfide is not possible. An appropriate test substrate will be hydrazine. The $[Fe4S4]^{3+/2+}$ redox couple is not reversible but the $[Fe4S4]^{2+/+}$ redox couple is reversible; therefore, the heme-bound-cluster complex should be reduced to the $[Fe^{2+}P]$–bridge–$[Fe_4S_4]^{+}$ state prior to substrate addition and reduction. The robust axial linkage should result in the bridge remaining intact.

The presence of Lewis bases such as solvent, substrate at high concentrations or the product of the reduction all have the potential of displacing the bridge in the axially coordinated model. These anticipated reaction conditions limit the versatility of the catalytic complex. Thus, the covalently bound complex design is preferred due to the robustness of the covalent linkage. Addition of substrate or coordinating solvents should not interfere with the connectivity of the heme and iron-sulfur cluster. As the model is presented thus far the transfer of an electron to the heme is occurs via the phenyl substituent. Because the phenyl rings are orthogonal to the conjugated π system of the porphyrin, the electronic coupling of the iron-sulfur cluster to the heme iron is weak. For more efficient electron transfer the porphyrin needs to be functionalized at the core of the porphyrin ring. With direct binding of the iron-sulfur cluster via a single hetero-atom to the conjugated π system of the porphyrin, strong electronic coupling of the two metal centers would be accomplished, ideal for fast electron transfer. An additional advantage

of the covalently bound model is the potential for the binding of multi-electron reduction (>2 electrons) with a single complex. A simple modification of the functionalized porphyrin can allow for multiple electron reservoirs by incorporating additional functional groups for the ligation of iron-sulfur clusters. Therefore, for the complex where one ferrous heme is covalently bound to four clusters reduced to the $[Fe_4S_4]^+$ state, five electrons would be available for reduction of substrate. As stated above, the axial coordinated model is limited to two electron transfers unless modification of the iron-sulfur cluster ligand allows for direct reduction of the cluster at an electrode surface rather than a sacrificial reductant that could also interact with substrate directly. The largest difficulty in testing for a catalytic turnover will be screening for a sacrificial reductant that will not reduce the substrate directly but will reduce the [4Fe-4S] cluster in either the axial or covalent bound model. Hence, it is suggested that a modification of the iron-sulfur cluster ligand should be considered for surface attachment to an electrode for electrochemical reduction of the iron-sulfur cluster for future catalytic investigations.

References

[1] C. Walsdorff, W. Saak, S. Pohl, *J. Chem. Soc., Dalton Trans.* **1997**, 1857-1861.

[2] a) L. Cai, R. H. Holm, *J. Am. Chem. Soc.* **1994**, *116*, 7177-7188; b) C. Zhou, L. Cai, R. H. Holm, *Inorg. Chem.* **1996**, *35*, 2767-2772.

[3] a) P. R. Challen, S.-M. Koo, W. R. Dunham, D. Coucouvanis, *J. Am. Chem. Soc.* **1990**, *112*, 2455-2456; b) T. Terada, T. Wakimoto, T. Nakamura, K. Hirabayashi, K. Tanaka, J. Li, T. Matsumoto, K. Tatsumi, *Chem. Asian J.* **2012**, *7*, 920-929.

[4] R. Holm, P. Kennepohl, E. I. Solomon, *Chem. Rev.* **1996**, *96*, 2239-2314.